Measurement of CP violation in $\mathrm{B}^0 \to \mathrm{J}/\psi + \mathrm{K_L}$ decay at KEK B-factory

Dissertation

Graduate school of Tohoku University

Mitsuhiro Yamaga

February 2001

Acknowledgment

I would like to thank everyone who helped me.

First, I would like to thank my advisor, Prof. Yamaguchi, for his gentle support and supervising my education of high energy physics.

Since I have worked mainly at KEK, I have been under the care of the KEK staffs. Especially, Prof. Kazuo Abe took great care of me over three years. I could not finish my work without his advice. I have no words to express my thanks to him.

I also thank all the Belle collaborators for many suggestions.

Finally I thank my wife, Atsuko Yamaga, for her support of my study as well as my life .

Abstract

We have measured the CP asymmetry parameter $\sin 2\phi_1$ in the $B^0 \to J/\psi + K_L$ decay at KEK B-factory.

For the detection of K_L and muons, the KLM detector subsystem was constructed which was based on glass-electrode resistive plate chambers (RPC). Although this was the first time that the glass plates were used as the RPC electrode, performance of the system under the high luminosity runs was proved to be excellent.

Only the direction of hadron shower, which was created by K_L, was measured by a combination of the KLM detector and the electromagnetic calorimeter. The $B^0 \to J/\psi + K_L$ signal was extracted from the center-of-mass momentum spectrum of the parent B^0, which was determined by the measured J/ψ momentum and K_L angle and assuming the two body decay. This is the first direct measurement of $B^0 \to J/\psi + K_L$ decay.

We observed 102 candidate events with an estimated background of 48 in the data sample of $6.2 fb^{-1}$. Although statistics is still limited, we could successfully identified the flavor of B meson, and measured the difference of decay vertices of two B mesons. From the proper-time difference analysis, we obtained $\sin 2\phi_1 = -1.00 \,^{+0.89}_{-0.73}$.

Contents

List of Figures

List of Tables

Chapter 1

Introduction

It is well known that the parity transformation P is violated in the weak interaction. This can be observed in the charged weak interaction where P is maximally parity-violating, that the charged vector boson $W^{\pm}$ couples only to left-handed fermions and right-handed antifermion. However, the Lagrangian for the weak interaction is invariant under the combined operations of P and charge conjugation C if the couplings have no physically significant phases.

The first observation of CP violation in the neutral kaon system in 1964 [1] suggested the existence of non-trivial phases in some cases of the weak couplings, and an enormous amount of theoretical work has been made to understand such mechanism. In a remarkable paper published in 1973, Kobayashi and Maskawa noted that CP violation could be accommodated in the Standard Model only if there were at least six quark flavors, twice the number of quark flavors known at that time [2]. The subsequent discovery of the c quark at SLAC [3] and BNL [4], and the b quark at Fermilab [5], and the t quark at CDF , has substantiated the six-quark Kobayashi-Maskawa (KM) hypothesis, and the KM model for CP violation is now considered to be an essential part of the Standard Model.

In 1980, Sanda and Carter pointed out that the KM model contained the possibility of large CP violating asymmetries in certain decay modes of the B mesons [6]. The subsequent observation of a long b quark lifetime [7] and a large amount of mixing in the neutral B meson system indicated that it would be feasible to carry out decisive tests of the KM model by studying B meson decays.

The observation of a CP violating asymmetry in B meson decays would be an important milestone; the first successful demonstration of a CP violating effect outside of the K^0 meson system; and would be a dramatic confirmation of the KM model. The importance of the research of CP violation in B decays is reflected in the number of laboratories. The BaBar [8] experiment at SLAC and CDF [9] are the competitive experiment with Belle. Other projects addressing this physics is also planned for LHC [10]. The goal of the Belle experiment at the first stage is to establish the CP violation in B decays.

In this thesis, we present a measurement of the CP asymmetry angle $\sin 2\phi_1$ in the $B^0 \to J/\psi + K_L$ decay using data collected by the Belle detector at KEK B-factory.

The outline of this thesis is as follows.

- First, physics formalism for CP violation is given in Chapter 2.

- An overview of experimental apparatus, KEK B-factory system which consists of KEKB accelerator and Belle detector is described in Chapter 3.

- Detailed description of the KLM detector system is given in Chapter 4.

- Software tools for data analysis and Monte Carlo simulation are described in Chapter 5.

- K_L reconstruction method and performance are described in Chapter 6.

- Reconstruction procedure of $B^0 \to J/\psi + K_L$ decay is described in Chapter 7.

- Extraction of CP asymmetry parameter $\sin 2\phi_1$ is described in Chapter 8.

- Finally, conclusion is given in Chapter 9.

Chapter 2

CP violation in B decays

In this chapter we describe the basic theory of CP violation in B decays and the measurement of the angles of unitarity triangle.

2.1 Description with the Standard Model

The hadronic sector of the standard model of weak and electromagnetic interactions is described by a Lagrangian which is constructed to be locally gauge invariant under the weak-isospin group $SU(2)_L$ and the weak hypercharge group $U(1)_Y$ with Weinberg-Salam Model [11]. In order to account for CP violation, the Lagrangian needs to have a non-trivial complex phase. The complex phase only appears in the Yukawa couplings for the interaction between quarks and Higgs bosons,

$$-\mathcal{L}_{\text{Yukawa}} = f_{ij}\overline{q}_{iL}\Phi n_{jR} + g_{ij}\overline{q}_{iL}\tilde{\Phi}p_{jR} + \text{hermitian conjugate}, \tag{2.1}$$

where

$$\Phi = \begin{pmatrix} \phi^+ \\ \phi^0 \end{pmatrix}, \tag{2.2}$$

$$\tilde{\Phi} = i\sigma^2\Phi^* = \begin{pmatrix} \phi^{0*} \\ -\phi^- \end{pmatrix}, \tag{2.3}$$

$$q_{iL} = \begin{pmatrix} p_i \\ n_i \end{pmatrix}, \tag{2.4}$$

$$p_{iL(R)} = \frac{1}{2}(1 \mp \gamma_5)p_i, \quad p_i = (u, c, t), \tag{2.5}$$

$$n_{iL(R)} = \frac{1}{2}(1 \mp \gamma_5)n_i, \quad n_i = (d, s, b), \tag{2.6}$$

$$f_{ij}, \ g_{ij} \ ; \ \text{arbitrary complex number.}$$

Under the spontaneous symmetry breaking, $SU(2)_L \times U(1)_Y \rightarrow U(1)_{EM}$, the complex field ϕ^0 is shifted and becomes real and the field ϕ^+ vanishes, then the Higgs

has a vacuum expectation value, $\langle\phi\rangle_0$,

$$\langle\phi\rangle_0 = \frac{1}{\sqrt{2}}\begin{pmatrix} 0 \\ v \end{pmatrix}. \tag{2.7}$$

After spontaneous symmetry breaking, we obtain the mass term in $\mathcal{L}_{\text{Yukawa}}$,

$$-\mathcal{L}_{\text{mass}} = \frac{v}{\sqrt{2}}(f_{ij}\overline{p}_{iL}p_{jR} + g_{ij}\overline{n}_{iL}n_{jR}) + \text{h.c.} \tag{2.8}$$

$$\equiv M^p_{ij}\overline{p}_{iL}p_{jR} + M^n_{ij}\overline{n}_{iL}n_{jR} + \text{h.c.}, \tag{2.9}$$

$$M^p_{ij} = \frac{v}{\sqrt{2}}f_{ij}, \quad M^n_{ij} = \frac{v}{\sqrt{2}}g_{ij}. \tag{2.10}$$

Since M^p_{ij} and M^n_{ij} are in general not diagonal, we must diagonalize these mass matrices in order to reveal the mass eigenstates. An arbitrary complex matrix can be diagonalized by means of appropriate two unitary matrices;

$$U^\dagger_L M^p U_R = M^u_{diag}, \quad D^\dagger_L M^n D_R = M^d_{diag}, \tag{2.11}$$

$$p_{L(R)} = U_{L(R)}u_{L(R)}, \quad n_{L(R)} = D_{L(R)}d_{L(R)}. \tag{2.12}$$

$u_{L(R)}$ and $n_{L(R)}$ are the mass eigenstates. With the mass eigenstates, the interactions of quarks with W bosons are given by

$$-\mathcal{L}_W = \frac{g}{\sqrt{2}}\overline{p}_{iL}\gamma_\mu n_{iL}W_{+\mu} + \text{h.c.} \tag{2.13}$$

$$= \frac{g}{\sqrt{2}}\overline{u}_{iL}V_{ij}\gamma_\mu d_{iL}W_{+\mu} + \text{h.c.}, \tag{2.14}$$

$$V = U^\dagger_L D_L. \tag{2.15}$$

There are three quark $SU(2)$ doublets, which written in the mass eigenstate basis are

$$q_{iL}: \quad \begin{pmatrix} u \\ d \end{pmatrix}_L \quad \begin{pmatrix} c \\ s \end{pmatrix}_L \quad \begin{pmatrix} t \\ b \end{pmatrix}_L. \tag{2.16}$$

The charged current leads to a term in the Lagrangian of the form

$$(\bar{u},\bar{c},\bar{t})_L\gamma^\mu(1-\gamma^5)V\begin{pmatrix} d \\ s \\ b \end{pmatrix}_L = (\bar{u},\bar{c},\bar{t})_L\gamma^\mu(1-\gamma^5)\begin{pmatrix} d' \\ s' \\ b' \end{pmatrix}_L, \tag{2.17}$$

where

$$\begin{pmatrix} d' \\ s' \\ b' \end{pmatrix} \equiv V\begin{pmatrix} d \\ s \\ b \end{pmatrix}. \tag{2.18}$$

Hence, it is not the mass eigenstates of the quark but the mixing among the different generations of them that interact with W bosons. The mixing matrix V for three

4

generations, which is referred to as Kobayashi-Maskawa (KM) matrix [2], can be written as

$$V = \begin{pmatrix} V_{ud} & V_{us} & V_{ub} \\ V_{cd} & V_{cs} & V_{cb} \\ V_{td} & V_{ts} & V_{tb} \end{pmatrix} \qquad (2.19)$$

CP violation arises from the complex term of KM matrix. The non-trivial complex phases are typically assigned to the furthest off-diagonal elements V_{ub} and V_{td}.

Wolfenstein described the KM matrix with a rather convenient approximate parameterization [12];

$$V = \begin{pmatrix} 1 - \frac{\lambda^2}{2} & \lambda & \lambda^3 A(\rho - i\eta) \\ -\lambda & 1 - \frac{\lambda^2}{2} & \lambda^2 A \\ \lambda^3 A(1 - \rho - i\eta) & -\lambda^2 A & 1 \end{pmatrix} + \mathcal{O}(\lambda^4) \qquad (2.20)$$

where there are four parameters, λ, A, ρ and η. These parameters has to be determined by experiments.

The best known element of V_{KM} is $V_{us} = \lambda$, which is the sine of the Cabibbo angle θ_c. From the measured rate for $K^- \to \pi^0 e^- \bar{\nu}_e$, one finds [13]

$$\lambda = \sin \theta_c = 0.2196 \pm 0.0023, \qquad (2.21)$$

an accuracy of about 1%.

The second best known element of V_{KM} is $V_{cb} = A\lambda^2$ which can be measured with semileptonic B meson decays. Both the exclusive decay $\bar{B} \to D^* \ell \bar{\nu}$ and the inclusive decay $\bar{B} \to X_c \ell \bar{\nu}$ have been used to extract V_{cb}, yielding consistent results. Combining the various experimental determination, one finds [13]

$$A = 0.819 \pm 0.035. \qquad (2.22)$$

With λ and A reasonably well determined, ρ and η remain the most important unknowns in V_{KM}. The relative strength of $b \to u$ and $b \to c$ transition in semileptonic B decay determines the ratio [13]

$$|V_{ub}/V_{cb}| = 0.08 \pm 0.02 \quad or \quad \sqrt{\rho^2 + \eta^2} = 0.364 \pm 0.091. \qquad (2.23)$$

2.2 The unitarity triangle

Unitarity of the KM matrix implies the unitarity equation

$$\sum_i V_{ij} V_{ik}^* = \delta_{jk} \qquad (2.24)$$

which can be represented as the equation of a closed triangle in the complex plane. The above equation involving V_{ub} and V_{td} gives the following triangular relation

$$V_{td} V_{tb}^* + V_{cd} V_{cb}^* + V_{ud} V_{ub}^* = 0 \qquad (2.25)$$
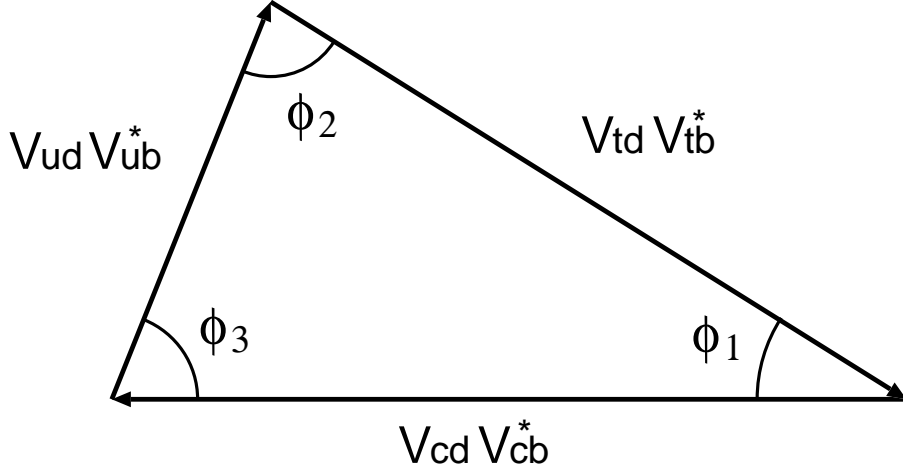
Figure 2.1: Unitarity triangle of KM matrix.

which is the most useful one from the phenomenological point of view since it contains the most poorly-known elements in the KM matrix. This triangle has the shape shown in Figure 2.1. CP is violated when the area of the triangle does not vanish, i.e. when all the angles are different from zero. The three internal angles are defined as

$$\phi_1 \equiv \arg\left(\frac{V_{cd}V_{cb}^*}{V_{td}V_{tb}^*}\right), \phi_2 \equiv \arg\left(\frac{V_{ud}V_{ub}^*}{V_{td}V_{tb}^*}\right), \phi_3 \equiv \arg\left(\frac{V_{cd}V_{cb}^*}{V_{ud}V_{ub}^*}\right) \qquad (2.26)$$

2.3 CP violation in B^0 meson system

2.3.1 $B^0 - \bar{B}^0$ mixing

The flavor state B^0 and $\bar{B}^0$ mix through the weak interaction. Figure 2.2 shows the box diagram for $B^0 - \bar{B}^0$ mixing in the standard model.
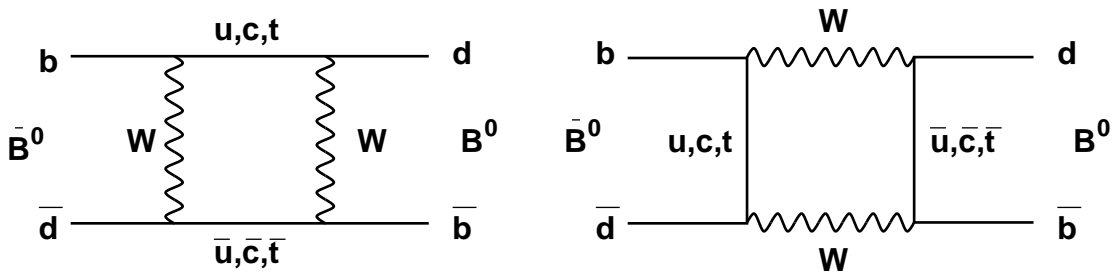
Figure 2.2: Box diagram for $B^0 - \bar{B}^0$ mixing.

The B meson state can be expressed as

$$|\Psi_B(t)\rangle = a(t)|B^0\rangle + b(t)|\overline{B}^0\rangle, \qquad (2.27)$$

6

or

$$\Psi_B(t) = \begin{pmatrix} a(t) \\ b(t) \end{pmatrix}, \tag{2.28}$$

which obeys the time-dependent Schrödinger equation

$$i\frac{\partial}{\partial t}|\Psi_B(t)\rangle = \mathbf{H}|\Psi_B(t)\rangle = E|\Psi_B(t)\rangle. \tag{2.29}$$

a and b are normalized as $|a(t)|^2 + |b(t)|^2 = 1$. The Hamiltonian $\mathbf{H}$ is a 2×2 matrix which is expressed as

$$\mathbf{H} = \begin{pmatrix} H_{11} & H_{12} \\ H_{21} & H_{22} \end{pmatrix} = \begin{pmatrix} \langle B^0|\mathbf{H}|B^0\rangle & \langle B^0|\mathbf{H}|\overline{B}^0\rangle \\ \langle \overline{B}^0|\mathbf{H}|B^0\rangle & \langle \overline{B}^0|\mathbf{H}|\overline{B}^0\rangle \end{pmatrix} \tag{2.30}$$

Considering that the wave function of decay particle is generally written as $\Psi(t) = \Psi(0)e^{-i(m-\frac{i}{2}\Gamma)t}$, $\mathbf{H}$ is written as

$$\mathbf{H} = \mathbf{M} - \frac{i}{2}\mathbf{\Gamma} \tag{2.31}$$

where $\mathbf{M}$ (mass matrix) and $\mathbf{\Gamma}$ (decay matrix) are Hermitian 2×2 matrices,

$$\mathbf{M} = \begin{pmatrix} M_{11} & M_{12} \\ M_{21} & M_{22} \end{pmatrix}, \quad \mathbf{\Gamma} = \begin{pmatrix} \Gamma_{11} & \Gamma_{12} \\ \Gamma_{21} & \Gamma_{22} \end{pmatrix}, \tag{2.32}$$

Since $\mathbf{M}$ and $\mathbf{\Gamma}$ are Hermitian,

$$M_{21} = M_{12}^*, \quad \Gamma_{21} = \Gamma_{12}^*. \tag{2.33}$$

According to the CPT invariance, we obtain the relation

$$M_{11} = M_{22}, \quad \Gamma_{11} = \Gamma_{22}. \tag{2.34}$$

Here we obtain the expression

$$\mathbf{H} = \begin{pmatrix} \langle B^0|\mathbf{H}|B^0\rangle & \langle B^0|\mathbf{H}|\overline{B}^0\rangle \\ \langle \overline{B}^0|\mathbf{H}|B^0\rangle & \langle \overline{B}^0|\mathbf{H}|\overline{B}^0\rangle \end{pmatrix} = \begin{pmatrix} M_0 - \frac{i}{2}\Gamma_0 & M_{12} - \frac{i}{2}\Gamma_{12} \\ M_{12}^* - \frac{i}{2}\Gamma_{12}^* & M_0 - \frac{i}{2}\Gamma_0 \end{pmatrix} \tag{2.35}$$

where $M_{11} = M_{22} = M_0$、$\Gamma_{11} = \Gamma_{22} = \Gamma_0$. The eigenstate of this Hamiltonian is the mass-eigenstate of real particle. Let us call the two state as "heavy" ($= B_H$) and "light" ($= B_L$). We obtain the eigenstate ($|B_H\rangle$、$|B_L\rangle$) and eigenvalue (λ_H、λ_L) for each state as follows :

$$\begin{aligned}
|B_H\rangle &= \frac{1}{\sqrt{|p|^2 + |q|^2}}\{p|B^0\rangle - q|\overline{B}^0\rangle\}, \\
|B_L\rangle &= \frac{1}{\sqrt{|p|^2 + |q|^2}}\{p|B^0\rangle + q|\overline{B}^0\rangle\}, \\
\lambda_H &= M_{11} - \frac{i}{2}\Gamma_{11} - pq \equiv m_H - \frac{i}{2}\Gamma_H, \\
\lambda_L &= M_{11} - \frac{i}{2}\Gamma_{11} + pq \equiv m_L - \frac{i}{2}\Gamma_L,
\end{aligned} \tag{2.36}$$

where

$$p = (M_{12} - \frac{i}{2}\Gamma_{12})^{1/2},$$

$$q = (M_{12}^* - \frac{i}{2}\Gamma_{12}^*)^{1/2}. \tag{2.37}$$

Define the mass difference $\Delta m_B \equiv m_H - m_L$ and the width difference $\Delta\Gamma_B \equiv \Gamma_H - \Gamma_L$. The solution for mixing parameter is

$$\frac{q}{p} = \sqrt{\frac{M_{12}^* - \frac{i}{2}\Gamma_{12}^*}{M_{12} - \frac{i}{2}\Gamma_{12}}} = -\frac{2\left(M_{12}^* - \frac{i}{2}\Gamma_{12}^*\right)}{\Delta m_B - \frac{i}{2}\Delta\Gamma_B} \tag{2.38}$$

An alternative common notation is to define $\bar{\epsilon}$ such that

$$p = \frac{1 + \bar{\epsilon}}{\sqrt{2\left(1 + |\bar{\epsilon}|^2\right)}}, \quad q = \frac{1 - \bar{\epsilon}}{\sqrt{2\left(1 + |\bar{\epsilon}|^2\right)}}, \quad \frac{q}{p} = \frac{1 - \bar{\epsilon}}{1 + \bar{\epsilon}}. \tag{2.39}$$

The condition

$$\left|\frac{q}{p}\right| \neq 1 \tag{2.40}$$

implies indirect CP violation, which results from the fact that the mass eigenstates are different from the CP eigenstates.

Although the $\Delta\Gamma_B$ has not been measured directly, since the decay channels common to B^0 and $\bar{B}^0$, which are responsible for the difference of $\Delta\Gamma_B$, are known to have the branching fractions of order 10^{-3} or less, it should follow that $\Delta\Gamma_B/\Gamma_B < 10^{-2}$. On the other hand, the observed $B^0 - \bar{B}^0$ mixing rate implies $x_d \equiv \Delta m_B/\Gamma_B = 0.74 \pm 0.04$ [14], i.e.

$$|\Delta\Gamma_B| \ll \Delta m_B. \tag{2.41}$$

Thus there is a negligible lifetime difference between the mass eigenstates. It follows that $|\Gamma_{12}| \ll |M_{12}|$, and to first order in Γ_{12}/M_{12} we obtain from (2.38)

$$\frac{q}{p} \simeq -\frac{M_{12}^*}{|M_{12}|}\left(1 - \frac{1}{2}\mathrm{Im}\frac{\Gamma_{12}}{M_{12}}\right). \tag{2.42}$$

Hence

$$1 - \left|\frac{q}{p}\right| \simeq 2\mathrm{Re}\,\bar{\epsilon} \sim \mathcal{O}(10^{-2}). \tag{2.43}$$

CP violation in $B^0 - \bar{B}^0$ mixing is a small effect as that in the kaon system.

2.3.2 Interference between decay and mixing

With $m_{H,L} = m_B \pm \frac{1}{2}\Delta m_B$ and $\Gamma_{H,L} \simeq \Gamma_B$, we obtain the time evolution of the state as

$$|B_H(t)\rangle = |B_H\rangle e^{-i(m_H - \frac{i}{2}\Gamma_B)t},$$

$$|B_L(t)\rangle = |B_L\rangle e^{-i(m_L - \frac{i}{2}\Gamma_B)t}. \tag{2.44}$$

From this equation we obtain the time evolution of $|B^0\rangle$ and $|\bar{B}^0\rangle$.

$$
\begin{aligned}
|B^0(t)\rangle &= g_+(t)|B^0\rangle + \frac{q}{p}g_-(t)|\overline{B}^0\rangle, \\
|\overline{B}^0(t)\rangle &= \frac{p}{q}g_-(t)|B^0\rangle + g_+(t)|\overline{B}^0\rangle,
\end{aligned}
\tag{2.45}
$$

where

$$
\begin{aligned}
g_+(t) &= e^{-i(m_B - \frac{i}{2}\Gamma_B)t}\cos(\tfrac{1}{2}\Delta m_B t), \\
g_-(t) &= ie^{-i(m_B - \frac{i}{2}\Gamma_B)t}\sin(\tfrac{1}{2}\Delta m_B t).
\end{aligned}
\tag{2.46}
$$

Consider that initially pure B^0 or $\bar{B}^0$ decays into the CP eigenstate f_{CP}. Due to $B^0 - \bar{B}^0$ mixing, there exist two decay channels,

$$
B^0 \to f_{CP}, \quad B^0 \to \bar{B}^0 \to f_{CP}
\tag{2.47}
$$

Define the decay amplitudes as

$$
\mathcal{A} \equiv \langle f_{CP}|B^0\rangle, \quad \overline{\mathcal{A}} \equiv \langle f_{CP}|\overline{B}^0\rangle.
\tag{2.48}
$$

For convenience we use

$$
\lambda \equiv \frac{q}{p}\frac{\overline{\mathcal{A}}}{\mathcal{A}}.
\tag{2.49}
$$

It can be shown that λ is independent of phase conventions and thus physically meaningful. In other words, the convention dependence of q/p cancels against that of $\overline{\mathcal{A}}/\mathcal{A}$.

The time-dependent decay amplitude from Equation (2.45) is expressed as

$$
\begin{aligned}
\langle f_{CP}|B^0(t)\rangle &= \mathcal{A}[g_+(t) + \lambda g_-(t)], \tag{2.50} \\
\langle f_{CP}|\overline{B}^0(t)\rangle &= \mathcal{A}\left(\frac{p}{q}\right)[g_-(t) + \lambda g_+(t)]. \tag{2.51}
\end{aligned}
$$

Thus we obtain the time-dependent decay width as

$$
\begin{aligned}
\Gamma(B^0(t) \to f_{CP}) &= |\mathcal{A}|^2 e^{-\Gamma_B t}\Big[\frac{1+|\lambda|^2}{2} + \frac{1-|\lambda|^2}{2}\cos(\Delta m_B t) - \mathrm{Im}\lambda\sin(\Delta m_B t)\Big], \\
\Gamma(\overline{B}^0(t) \to f_{CP}) &= |\mathcal{A}|^2 e^{-\Gamma_B t}\Big[\frac{1+|\lambda|^2}{2} - \frac{1-|\lambda|^2}{2}\cos(\Delta m_B t) + \mathrm{Im}\lambda\sin(\Delta m_B t)\Big].
\end{aligned}
\tag{2.52}
$$

Now we define the time-dependent CP asymmetry,

$$
A_{f_{CP}}(t) \equiv \frac{\Gamma(B^0(t) \to f_{CP}) - \Gamma(\bar{B}^0(t) \to f_{CP})}{\Gamma(B^0(t) \to f_{CP}) + \Gamma(\bar{B}^0(t) \to f_{CP})}.
\tag{2.53}
$$

Using Equation (2.52) it is expressed as

$$
A_{f_{CP}}(t) = \frac{(1-|\lambda|^2)\cos(\Delta m_B t) - 2\mathrm{Im}\lambda\sin(\Delta m_B t)}{1+|\lambda|^2},
\tag{2.54}
$$

9

In case of neutral B meson, $|\Gamma_{12}| \ll \|M_{12}|$, so q/p is approximately

$$\frac{q}{p} = \sqrt{\frac{M_{12}^* - \frac{i}{2}\Gamma_{12}^*}{M_{12} - \frac{i}{2}\Gamma_{12}}} \approx \sqrt{\frac{M_{12}^*}{M_{12}}}, \tag{2.55}$$

and hence $|q/p| = 1$. Also note that if a single combination of quark-mixing-matrix elements contributes to $B^0 \to f_{CP}$ and $\bar{B}^0 \to f_{CP}$, $|\bar{\mathcal{A}}/\mathcal{A}| = 1$. Therefore

$$|\lambda| = \left|\frac{q}{p}\right| \left|\frac{\bar{\mathcal{A}}}{\mathcal{A}}\right| = 1. \tag{2.56}$$

Thus Equation (2.54) becomes

$$A_{f_{CP}}(t) \simeq -\text{Im}\lambda \sin(\Delta m_B t) \tag{2.57}$$

This method using such decays is very useful and shows large CP violation in the Standard Model prediction. The quantity $\text{Im}\lambda$ which can be extracted from $A_{f_{CP}}$ is theoretically very interesting since it can be directly related to KM matrix elements in the Standard Model.

2.4 ϕ_1 measurement

- $B^0 \to J/\psi K_S$

One of the cleanest example that we can measure the unitarity angle is the $B^0 \to J/\psi K_S$ via $b \to c\bar{c}s$ quark transition. $B^0 \to J/\psi K_S \to \ell^+\ell^-\pi^+\pi^-$ is the most promising mode since the branching ratio for this mode has been measured and the signals are very clean with no appreciable background. Figure 2.3 shows the Feynman diagram for this decay.

In the B meson system, up to corrections of order 10^{-2}, we have

$$\left(\frac{q}{p}\right) \simeq \sqrt{\frac{M_{12}^*}{M_{12}}} = \frac{V_{tb}^* V_{td}}{V_{tb} V_{td}^*} = e^{-2i\phi_1}. \tag{2.58}$$

This combination of KM parameters can be read off directly from the vertices of the box diagram in Figure 2.2, which in the Standard Model are responsible for the non-diagonal element M_{12}^* of the mass matrix. As shown in Figure 2.3, the weak phase in the tree diagram is represented by $V_{cb}^* V_{cs}$. With $CP(J/\psi K_S) = -1$, one finds

$$\lambda_{J/\psi K_S} = -\left(\frac{q}{p}\right)_B \cdot \left(\frac{q}{p}\right)_K \cdot \frac{\bar{\mathcal{A}}}{\mathcal{A}} = \frac{V_{tb}^* V_{td}}{V_{tb} V_{td}^*} \cdot \frac{V_{cs} V_{cd}}{V_{cs}^* V_{cd}} \cdot \frac{V_{cb} V_{cs}^*}{V_{cb}^* V_{cs}} = -e^{-2i\phi_1}, \tag{2.59}$$

where the first term comes from $B^0 - \bar{B}^0$ mixing, the second from the ratio $\bar{\mathcal{A}}_f/\mathcal{A}_f$ and the third from $K^0 - \bar{K}^0$ mixing. Therefore we obtain

$$\text{Im}\lambda_{J/\psi K_S} \simeq \sin 2\phi_1. \tag{2.60}$$

There are additional contributions from the penguin diagram represented by $V_{ib}^* V_{is}$ ($i = u, c, t$). While the t quark and c quark contribution have the same magnitude of that as the tree diagram, they do not have the relative phase with respect to the tree diagram. The u quark contribution, on the other hand, has a different phase ($V_{ub}^* V_{us}$). However its magnitude is at the order of λ^4 as compared to λ^2 for the others, and it can be negligible. Thus the measurement of ϕ_1 via $B^0 \to J/\psi K_S$ is straightforward.
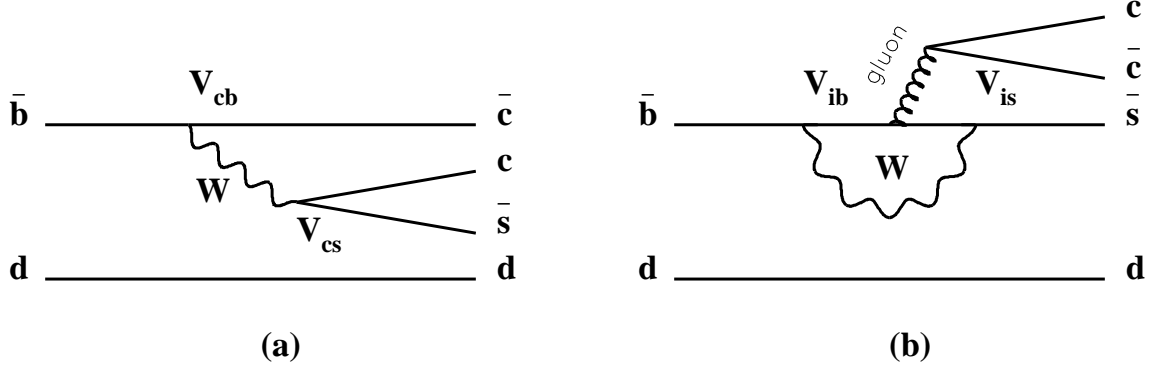
Figure 2.3: Diagram for $B^0 \to J/\psi K_S$, (a) Tree diagram, and (b) Penguin diagram.

- $B^0 \to J/\psi K_L$

The $B^0 \to J/\psi + K_L$ decay mode provides another measurement of the ϕ_1 angle that complements the measurement of $J/\psi K_S$. This channel has the same branching ratio as that for $J/\psi K_S$, and a large fraction of the K_Ls can be detected by the ECL and the KLM. However, we cannot measure the energy of K_L by either the ECL or the KLM. Thus $J/\psi K_L$ decay is not fully reconstructed, which will result in suffering from large backgrounds.

Since, approximately, K_L has an opposite CP from K_S, CP of $J/\psi K_L$ final state is $+1$, which is opposite from the $J/\psi K_S$ final state.

Experimentally we measure $\Delta t = t_{CP} - t_{tag}$ instead of t, where t_{CP} is the decay time of B decaying to a CP eigenstate and t_{tag} is the decay time of the other B. To extract $\sin 2\phi_1$, we measure the proper time difference distribution instead of $A_{f_{CP}}$,

$$\frac{dN}{d\Delta t} = \frac{1}{\tau_B} e^{-|\Delta t|/\tau_B} \left[1 - \eta_{CP} \sin 2\phi_1 \sin(\Delta m_B \Delta t) \right]. \tag{2.61}$$

Figure 2.4 illustrates an example of the time-dependent CP asymmetry measurement with $B^0 \to J/\psi + K_L$ decay.
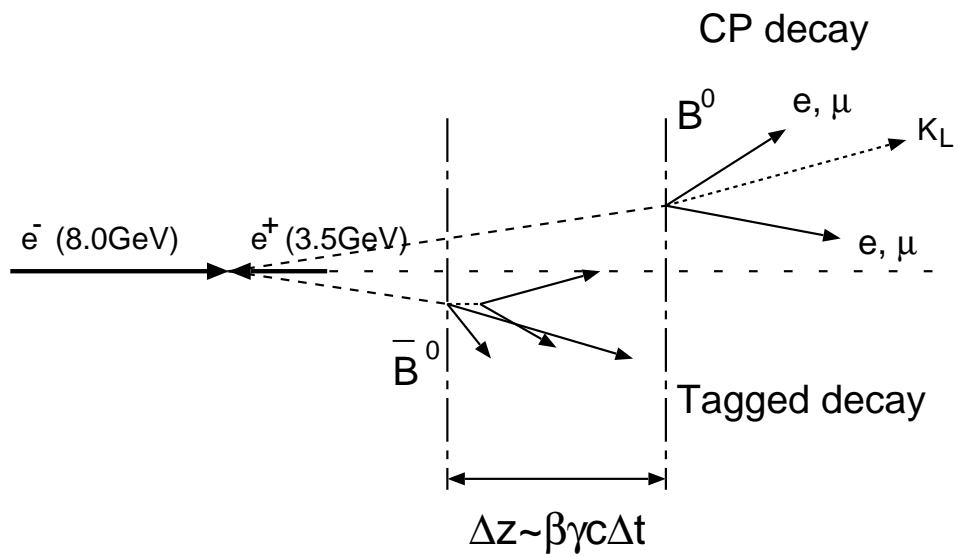
Figure 2.4: Time dependent CP asymmetry measurement with $B^0 \to J/\psi K_L$.

Chapter 3

KEK B-factory

KEK B-factory consists of an asymmetric high luminosity e^+e^- collider and detector system built at KEK (High Energy Accelerator and Research Organization, Japan). KEKB accelerator is designed to produce a large number of B mesons. The Belle detector is optimized to measure the particles from B meson decays effectively.

In this chapter we describe the experimental apparatus of KEK B-factory. KEKB accelerator specification, Belle detector system with sub detector components and data acquisition system are described.

3.1 KEKB accelerator

KEKB accelerator is an e^+e^- collider with asymmetric beam energies. The center of mass energy is set to 10.58 GeV which is on the $\Upsilon(4S)$ resonance state. Since $\Upsilon(4S)$ decays only into B meson pairs, we can generate B meson pairs efficiently. In the $\Upsilon(4S)$ rest frame, the average momentum of B meson in the $\Upsilon(4S)$ decay is about 340 MeV/c, so the average decay length is approximately 30 μm. This length is too short to measure the difference of the vertex of two B mesons by present vertex detector. So $\Upsilon(4S)$ is Lorentz boosted so that the flight length of B mesons are long enough to be measured by the vertex detector. The asymmetry of beam energy is expressed as

$$\beta\gamma = \frac{E_- - E_+}{\sqrt{s}}$$

where $\beta\gamma$ is the Lorentz boost parameter, $\sqrt{s}$ is the center of mass energy, and E_- and E_+ are the energy of electron and positron, respectively. There are two factors to optimize this asymmetry. One is the flight length of the B mesons, and the other is the detector acceptance. Figure 3.1 shows the required integrated luminosity as a function of $\beta\gamma$ to measure the CP asymmetry parameter, $\sin 2\phi_1$, with 3σ. It does not change so significantly within the range of 0.4 to 0.8. Thus the asymmetry was determined to be $\beta\gamma = 0.425$, and the energy of electron and positron is set to $E_- = 8.0$ GeV and $E_+ = 3.5$ GeV. The average decay length is approximately 200 μm in this case.

Figure 3.2 shows the overview of KEKB [15]. The electron ring (HER:High
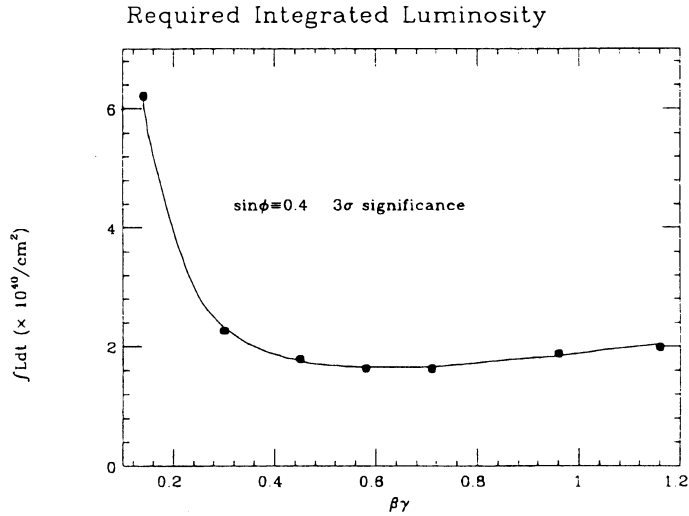
Figure 3.1: Required integrated luminosity to measure the CP asymmetry.

energy ring) and the positron ring (LER:Low energy ring) are built side by side in the tunnel which has a circumference of about 3km. There is only one interaction point at Tsukuba area, where the Belle detector is located. 8 GeV electrons and 3.5 GeV positrons are directly injected from the Linear Accelerator. The RF cavities of HER (LER) are installed at the straight section of Nikko and Oho area (Fuji area). Two wigglers for LER are also located at Nikko and Oho area, so that they reduce the longitudinal damping time of the LER from 43 ms to 23 ms, i.e. the same damping time as the HER. The design luminosity of KEKB is 10^{34} cm^{-2}s^{-1}. This is 50 times higher than the world record which was achieved by CESR of Cornell university. To achieve this luminosity, 5000 bunches are need to be accumulated in each ring at maximum capacity. For now this is not achieved yet, and we are operating it with about 1000 bunches . At KEKB, electron and positron beams collide at a finite angle of ±11 mrad in order to reduce parasitic collisions, so it is not necessary to bend the beam with bending magnets near the interaction point, which can become a source of synchrotron X-ray background in the detector. The main parameters are summarized in Table 3.1 [15].

3.2 Belle detector

Figure 3.3 and 3.4 shows the configuration of Belle detector. Due to the asymmetry of beam energy, the detector also has the asymmetric structure along the beam direction. For the precise and effective measurement of CP asymmetry with B mesons, the following are required.

- Precise measurement of the decay vertex of the B mesons for the proper time determination.

- Efficient track finding capability of charged particles.

14
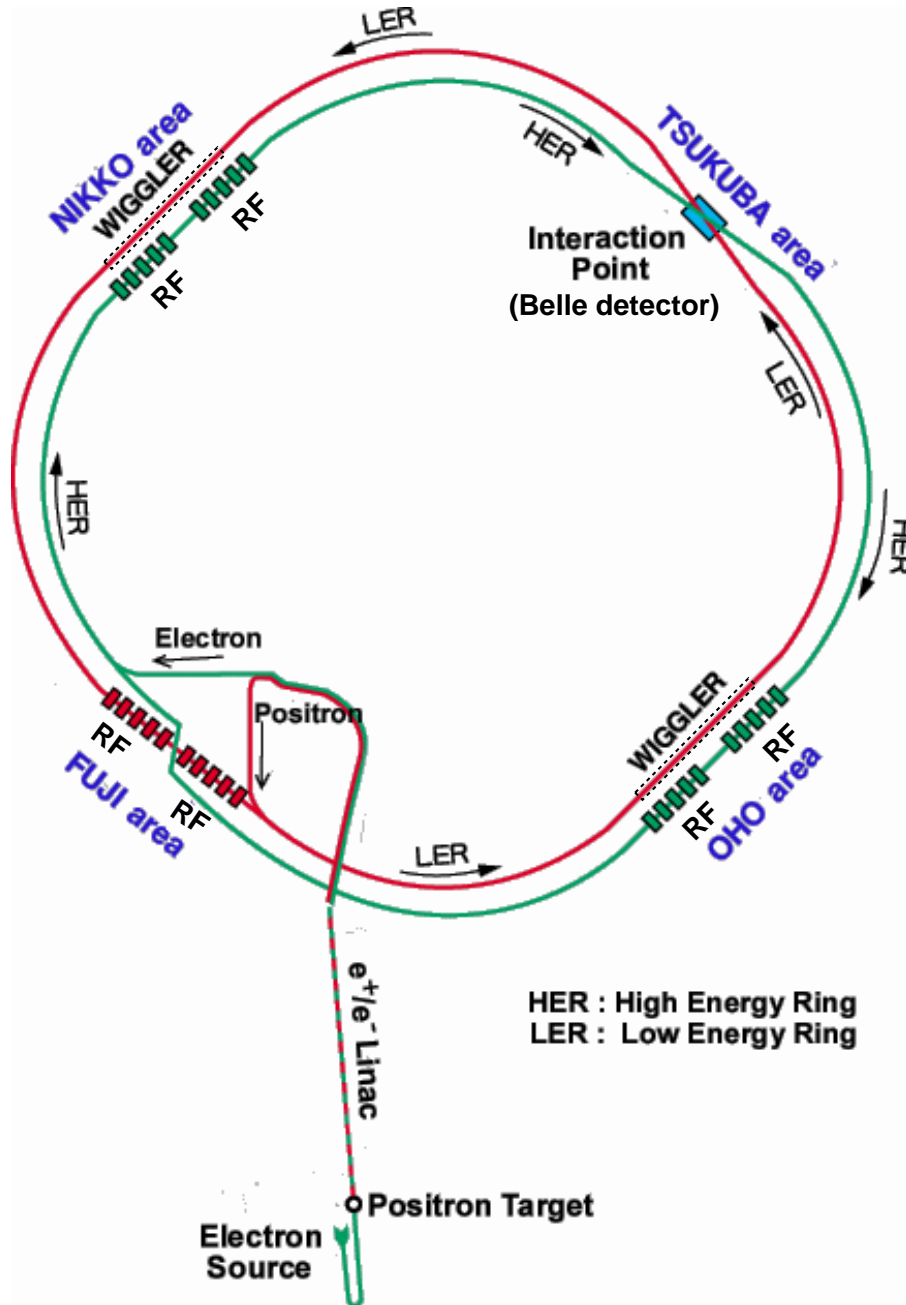
Figure 3.2: Configuration of KEKB accelerator.

- Good particle identification for the reconstruction of exclusive B meson final state and flavor tagging.

- High resolution photon detection capability.

- Efficient trigger and data acquisition system.

The vertex measurement is done by the silicon vertex detector (SVD) just outside the beam pipe. The charged particle tracking is done by the central drift chamber (CDC). K/π separation is made by a combination of dE/dx measurement with the CDC and the aerogel Čerenkov counter (ACC) and the time of flight counter (TOF). Electromagnetic showers are detected by the CsI(Tl) electromagnetic calorimeter (ECL). All the detectors mentioned above are located inside the superconducting solenoidal magnet which provides a uniform magnetic field of 1.5 Tesla along the direction of the detector z-axis. The outermost detector is the K_L and muon detector (KLM) which is instrumented in the iron return yoke. The coordinate system of Belle is defined as shown in Figure 3.5.

A brief description of each components are described in the following sections.
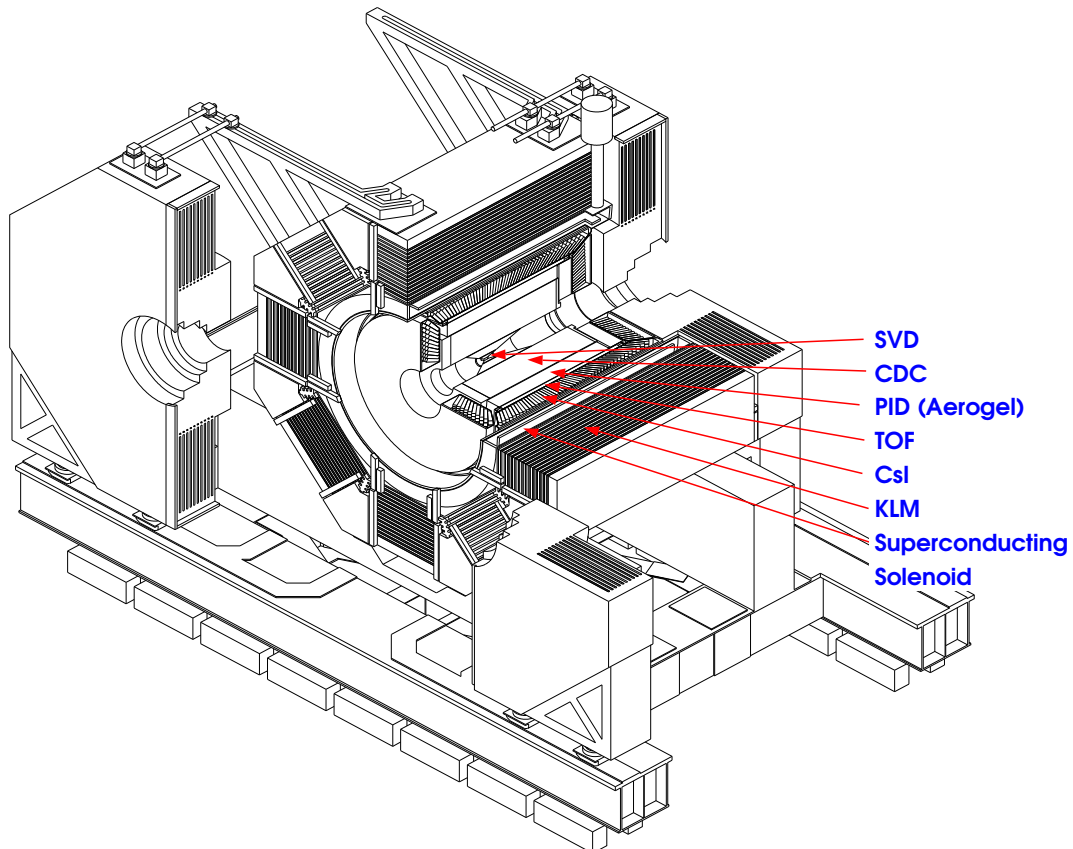
Figure 3.3: Belle detector.

16
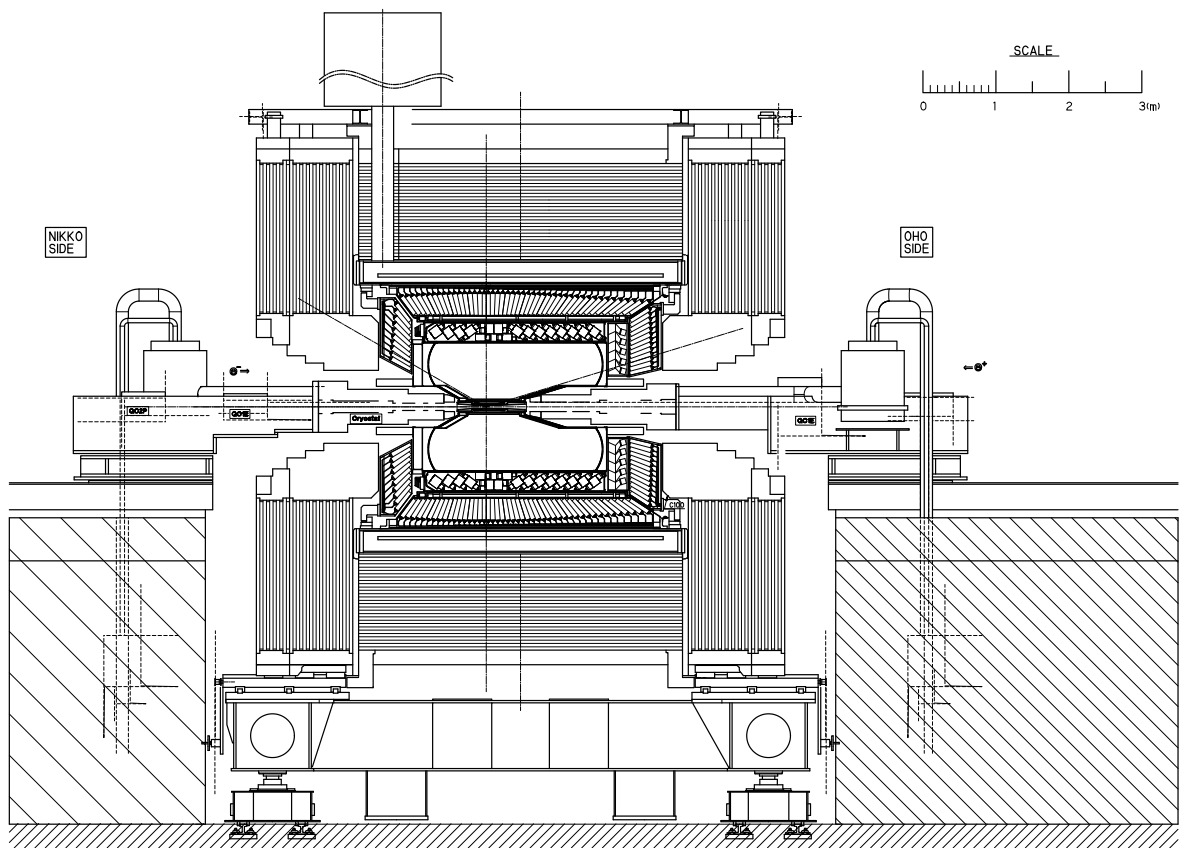
Figure 3.4: Side view of Belle detector.
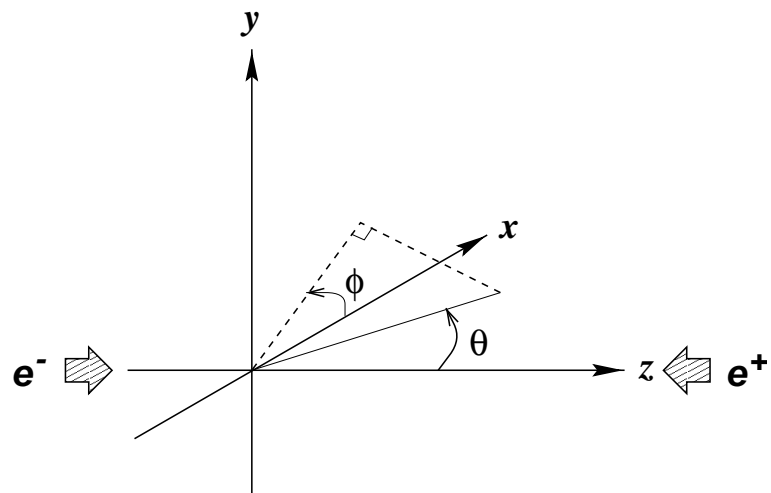
Figure 3.5: Definition of Belle coordinate system.

3.2.1 Silicon Vertex Detector(SVD)

Figure 3.6 shows the configuration of SVD. The SVD has three detection layers consisting of 8, 10 and 14 units of the double sided silicon detectors (DSSD), respectively. The thickness of a DSSD is 300 μm. The 2 dimensional position can be measured by each layer. The z-vertex resolution is estimated to be 113 μm including the effect of the beam background, which is sufficient to allow study of CP violation. The SVD occupies the region from 20.5 mm to 75 mm in radius, and from -150 mm to 220 mm in z. The acceptance in polar angle is $20° < \theta < 150°$. The total number of readout channels is about 82,000. The details of SVD is described in [16].
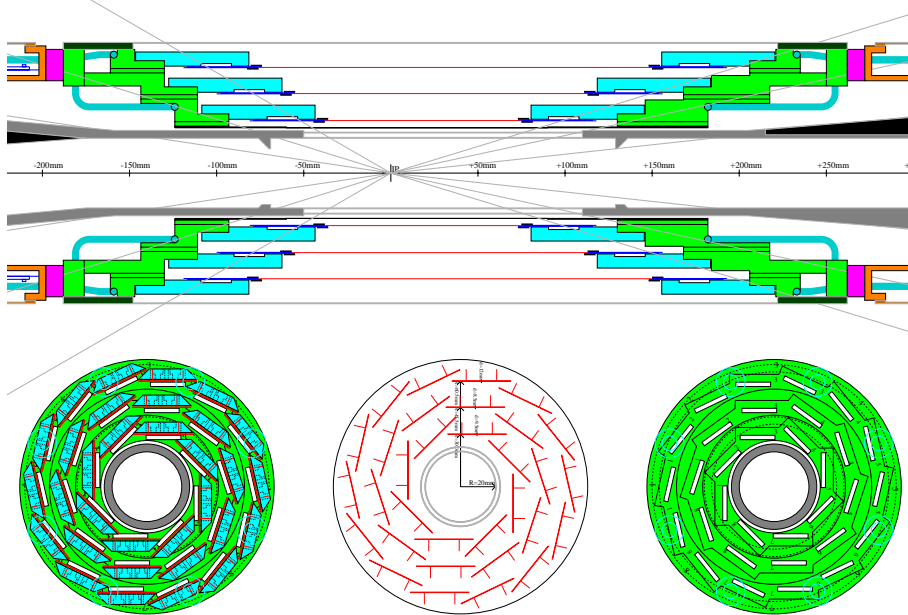
Figure 3.6: Silicon Vertex Detector(SVD).

3.2.2 Central Drift Chamber (CDC)

The CDC is a small-cell drift chamber which contains 50 anode sense-wire layers and 3 cathode-strip layers. The anode layer consists of 32 axial-wire layers and 18 stereo-wire layers, and provide 3 dimensional tracks with combining the hit information of axial and stereo wires. Stereo angles range from 42.5 to 72.1 mrad. The cathode strip layers are located at innermost of the CDC, and reconstruct z-position precisely. The CDC occupies a region from 77 mm to 880 mm in radius. The acceptance is $17° < \theta < 150°$ in polar angle. A low Z gas mixture (50% helium - 50% ethane) is used to minimize the multiple coulomb scattering contribution to the momentum resolution. The total number of readout channels is 8,400 for the anode and 1,792 for the cathode. Using muon tracks from cosmic rays a resolution of $\delta p_t/p_t = (0.20 \oplus 0.29 p_t)\%$ is obtained [1]. The dE/dx resolution for hadron tracks is 6.9%. Figure 3.7 shows the geometrical configuration of the CDC.

---

[1] $a \oplus b \equiv \sqrt{a^2 + b^2}$

CDC structure
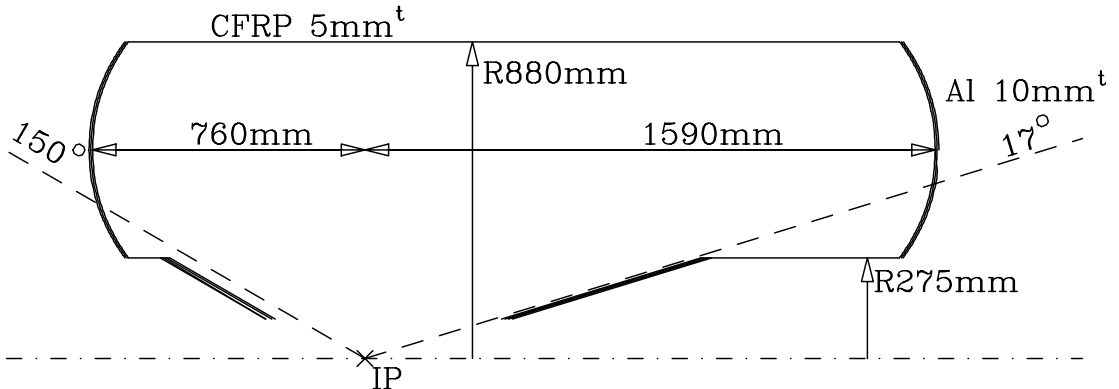
Figure 3.7: Central drift chamber (CDC).

3.2.3 Aerogel Čerenkov Counter (ACC)

The ACC is a silica aerogel threshold counter. It is designed to separate kaons and pions in high momentum range of $0.8 \sim 3.5$ GeV/c. Counters in the barrel region have different refraction indices $n = 1.01, 1.013, 1.015, 1.020$ and 1.028, depending on the polar angle, which are optimized to match the kinematics of two body decays from B mesons. The refraction index of the endcap counters, on the other hand, is 1.030, which are optimized for the kaon identification for flavor tagging. The Čerenkov light is collected and amplified by fine-mesh photomultipliers(FMPMTs) which can operate in the 1.5T magnetic field. The barrel part consists of 960 aerogel counters segmented into 16 divisions in z and 60 in ϕ. The number of readout channels is 1,560 in the barrel and 228 in the endcap. The acceptance is $17° < \theta < 127°$. Figure 3.8 and 3.9 shows the configuration of barrel and endcap aerogel Čerenkov counter, respectively.

3.2.4 Time of Flight counter (TOF/TSC)

The Time of Flight counter (TOF) is used to separate kaons and pions in the momentum range up to 1.2 GeV/c. The Trigger Scintillation Counter (TSC) provides timing signals for the trigger. One 5 mm-thick TSC layer and one 4 cm-thick TOF counter layer are placed at the position of 120 cm in radius from IP with a 2 cm gap between them. The TOF is segmented into 128 in ϕ and each counter is read out by one FMPMT at each end. The TSC has a 64 segmentation and are read out only from the backward end by a single FMPMT. The total number of readout channels is 256 for TOF and 64 for TSC. The time resolution is $\sigma_t \simeq 100$ ps. Figure 3.10 shows the configuration of TOF/TSC.
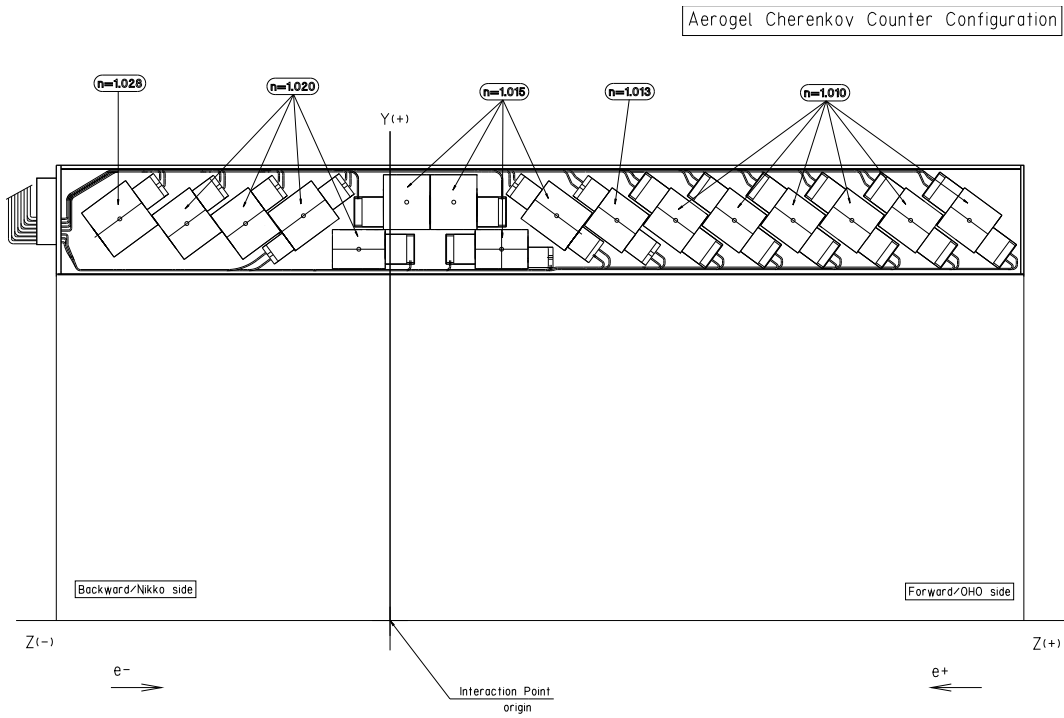
Figure 3.8: Configuration of barrel ACC.
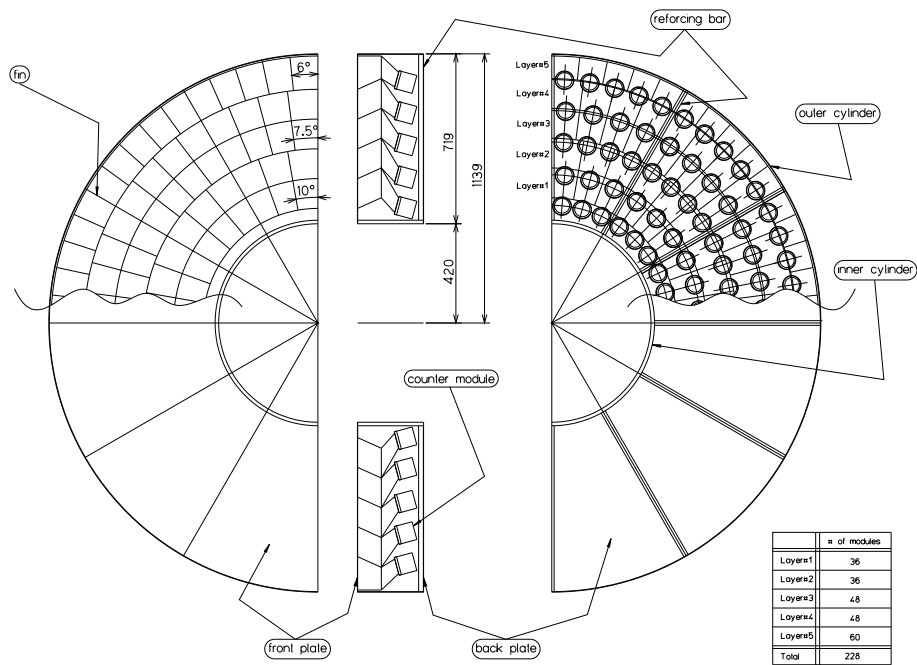
Figure 3.9: Configuration of endcap ACC.

20
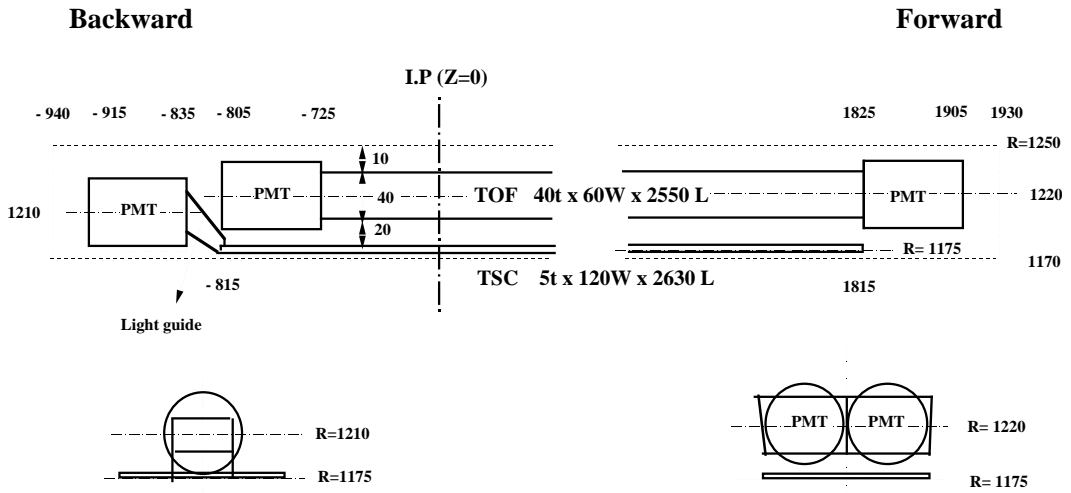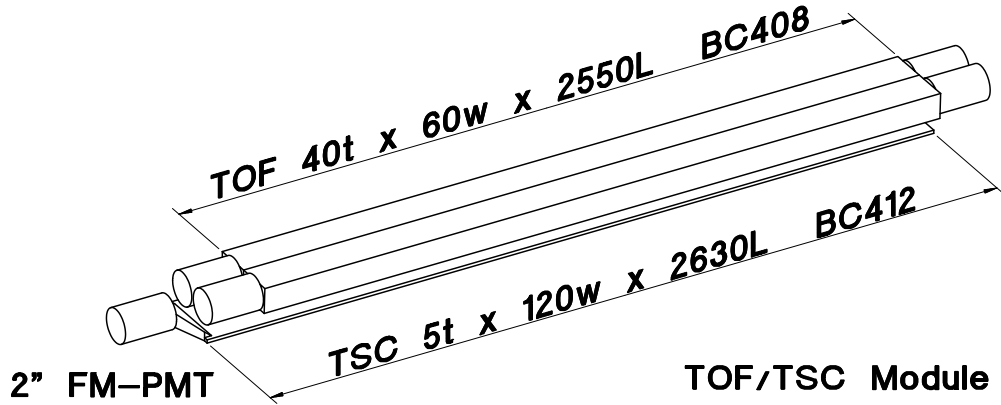
Figure 3.10: Configuration of TOF/TSC.

3.2.5   Electromagnetic Calorimeter(ECL)

The ECL is used to measure energy deposit by electromagnetic showers. Photons and electrons deposit most of their energies in the ECL, but the other kind of particles deposit a part of their energies. The matching of the energy measured by the ECL and the momentum of a charged particle measured by the CDC is used for the electron identification.

The ECL consists of 8,736 blocks of 30 cm×5.5 cm×5.5 cm CsI(Tl) crystals. They are assembled into a tower structure pointing near the interaction point. Figure 3.11 shows the overall configuration of the ECL. The barrel part has 46 segments in θ and 144 segments in ϕ. The forward (backward) endcap has 13 (10) segments in θ and the ϕ segments vary from 48 to 144 (from 64 to 144). The barrel part has 6,624 crystals and the forward (backward) endcap has 1,152 (960) crystals. Each crystal is read out by two 2 cm×1 cm photodiodes. Barrel crystals are placed at $r = 125$ cm. Forward (backward) endcap crystals are at $z = +196$ cm (-102 cm).

The energy resolution is $\sigma_E/E = 0.066\%/E \oplus 0.81\%/E^{1/4} \oplus 1.34\%$ and the

position resolution is $\sigma_{pos} = 0.5$ cm/$\sqrt{E}$, where the unit of E is GeV. Total amount of material in front of the CsI is $0.387X_0$ at $\theta = 90°$, where X_0 is the unit radiation length.

3.2.6 K_L/μ detector (KLM)

The KLM is the only sub-detector that is placed outside the solenoid coil. It was designed to detect K_L and muon. It consists of octagonal barrel region and two endcap regions that are divided into quadrants. Both parts have a structure of alternating layers of 47mm thick iron plates and 44mm thick slots where RPCs (Resistive plate chamber) are mounted. There are 15 slots in the barrel and 14 in the endcap. The iron also serves as a flux return for the magnetic field of solenoid coil.

The details of KLM is explained in chapter 4.

3.2.7 Extreme Forward Calorimeter (EFC)

The EFC is the additional electromagnetic calorimeter that is used to measure the energy of photons and electrons in the extreme forward direction.

Since the EFC is exposed in the high irradiation (about 5 MRad per year) of photons and electrons by the synchrotron radiation and the spent electrons, BGO ($Bi_4Ge_3O_{12}$) crystals are used. Both forward and backward EFC consists of BGO crystals divided into 5 segments in θ and 32 in ϕ. Typical crystal size is about 2 cm$\times$2 cm, with a length of 13.4 cm($12X_0$) for forward and 11.8 cm ($10.5X_0$) for backward. The EFC covers $6.2° < \theta < 11.6°$ and $163.1 < \theta < 171.5°$. The details of EFC is described in [17].

3.2.8 Trigger and data acquisition

The Belle data acquisition system consists of four major parts as shown in Figure 3.13 : the event readout part, the event builder part, the timing control part and the slow control part. The readout part can run in parallel for each detector subsystem at 500 Hz in maximum. All the subsystem, except for SVD, use a system consisting of FASTBUS TDC and VME for digitizing the data. The charge and/or timing information of each channel of detectors are converted into a multi-edge timing signal with Charge-to-Time conversion frontend electronics, except for KLM which provides the time-multiplexed information on a single line. The SVD information is processed on the data scanner and is directly sent to the VME memory.

The trigger information is provided by CDC, TOF, ECL, KLM, EFC and processed by global decision logic circuit (GDL) for the trigger decision. Figure 3.14 shows the overview of the Belle trigger system. The decision is distributed by the sequence control system via Timing Distributor Module in each subsystem VME.

The data is transfered to the Event Builder switch network, where the detector-wide parallel data is recorded into event-wide parallel data and shipped to each node of the Online Farm. The Online Farm consists of 120 processors for the fast
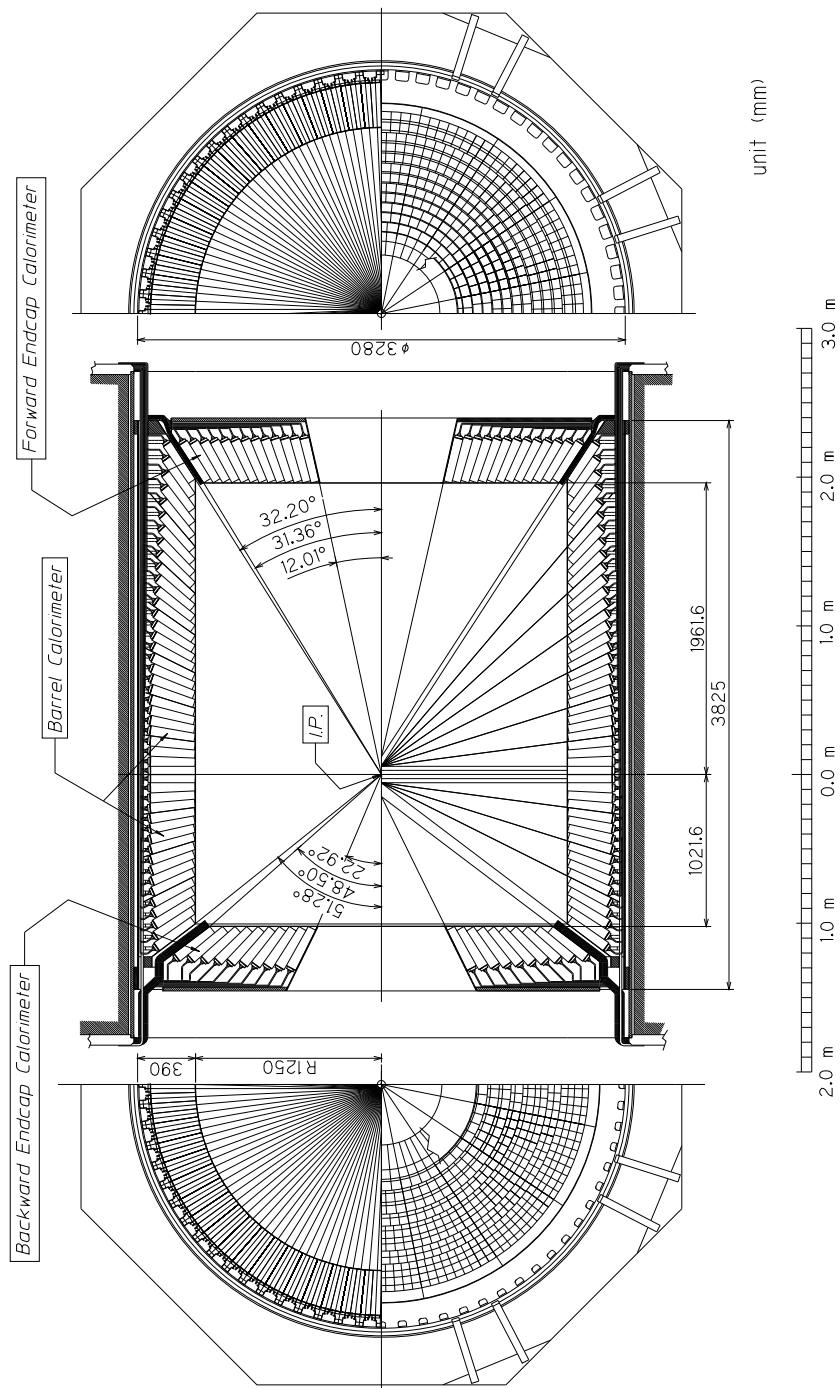
Figure 3.11: CsI calorimeter.
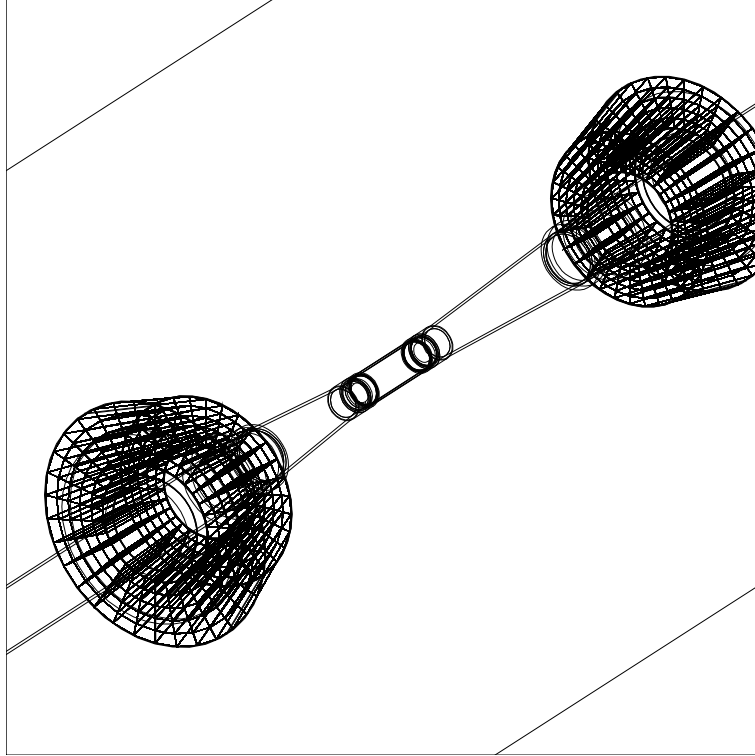
Figure 3.12: Extreme Forward Calorimeter.

reconstruction of up to 15 MBytes/sec event data stream. The events which passed the Farm is stored into the Mass Storage System and eventually stored into the tape system.

All the subsystem are controlled centrally by the Master Control. The message passing is done through a conventional TCP/IP network. The network also provides an experiment-wide shared memory (NSM) in order to store the useful run-related and environmental-related information for control and monitoring purpose.

3.3   KEKB and Belle commissioning

The detector construction was completed in Dec.1998. The detector has been calibrated with cosmic rays. The first cosmic ray event was observed on Jan.18, 1999 with all the subsystems operating with and without 1.5 Tesla magnetic field. The detector was rolled into the interaction point on May 1, 1999.

The first commissioning of the KEKB accelerator was from May 24 to Aug.4, 1999. The first B meson was observed on Jun.1, 1999. During first beam run period, the peak luminosity reached 3×10^{32}cm^{-2}s^{-1}, and 26 pb^{-1} data were recorded in total. During the running from Oct., 1999 to July, 2000, the peak luminosity has reached 2.2×10^{33}cm^{-2}s^{-1}, and the integrated luminosity of 6.8 fb^{-1} was accumulated. The present peak luminosity is still 20% of the designed value. Efforts for further machine tuning and improvement of some of the machine components continue. Figure 3.15
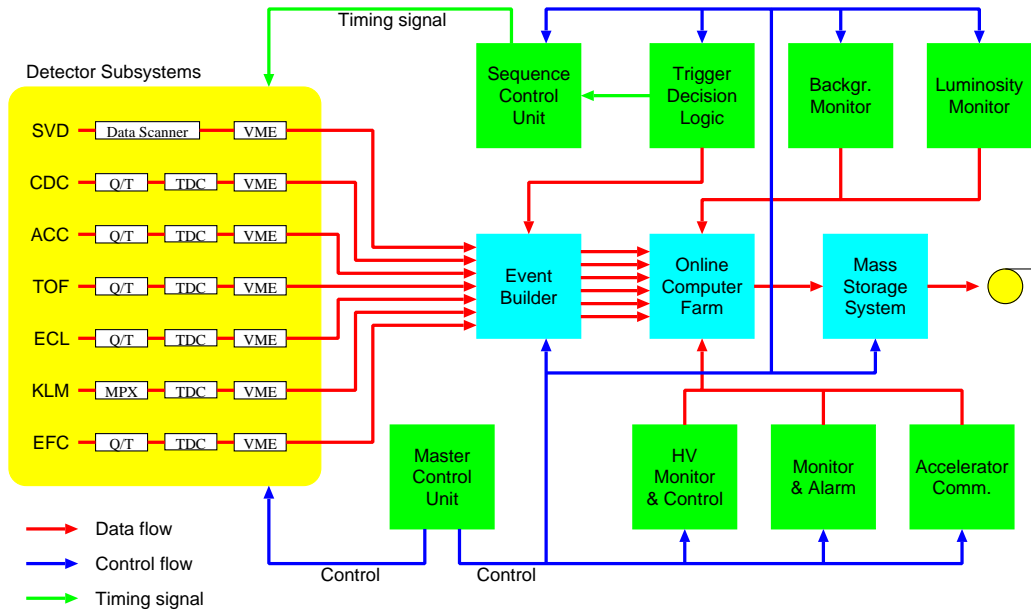
Figure 3.13: Data acquisition system.
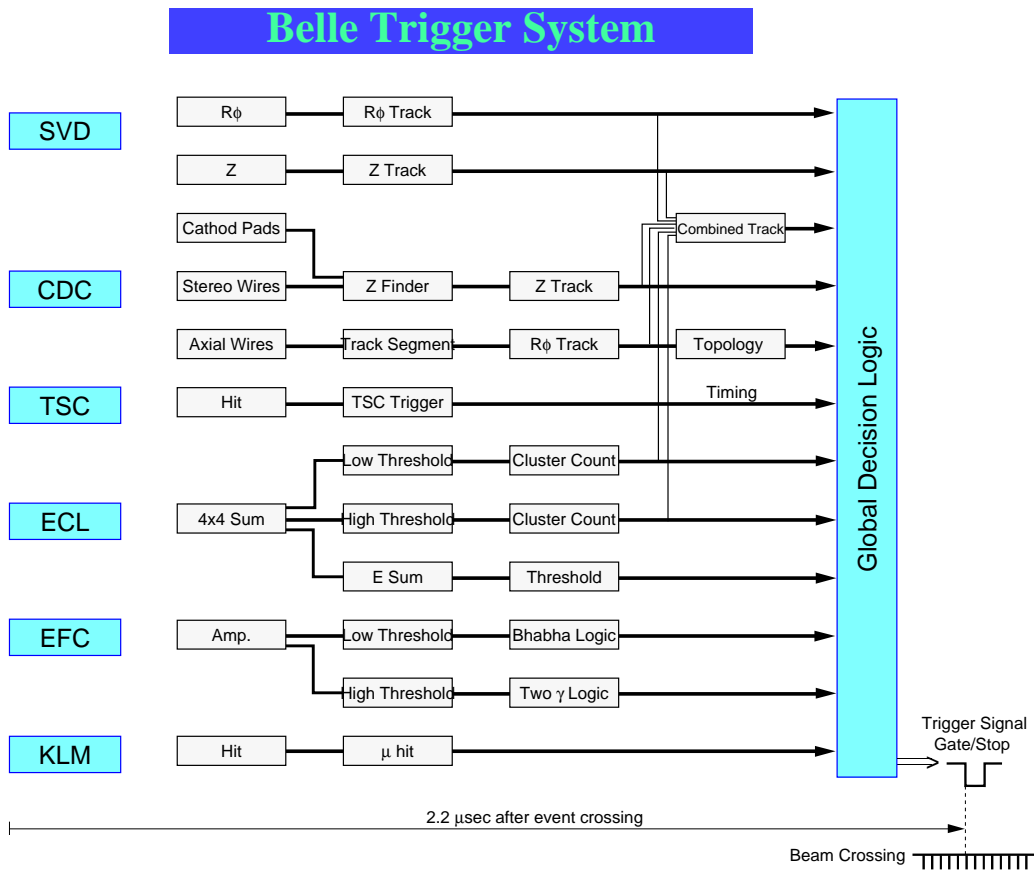
Figure 3.14: Trigger scheme.

shows the history of the luminosity of the KEKB until July 2000.
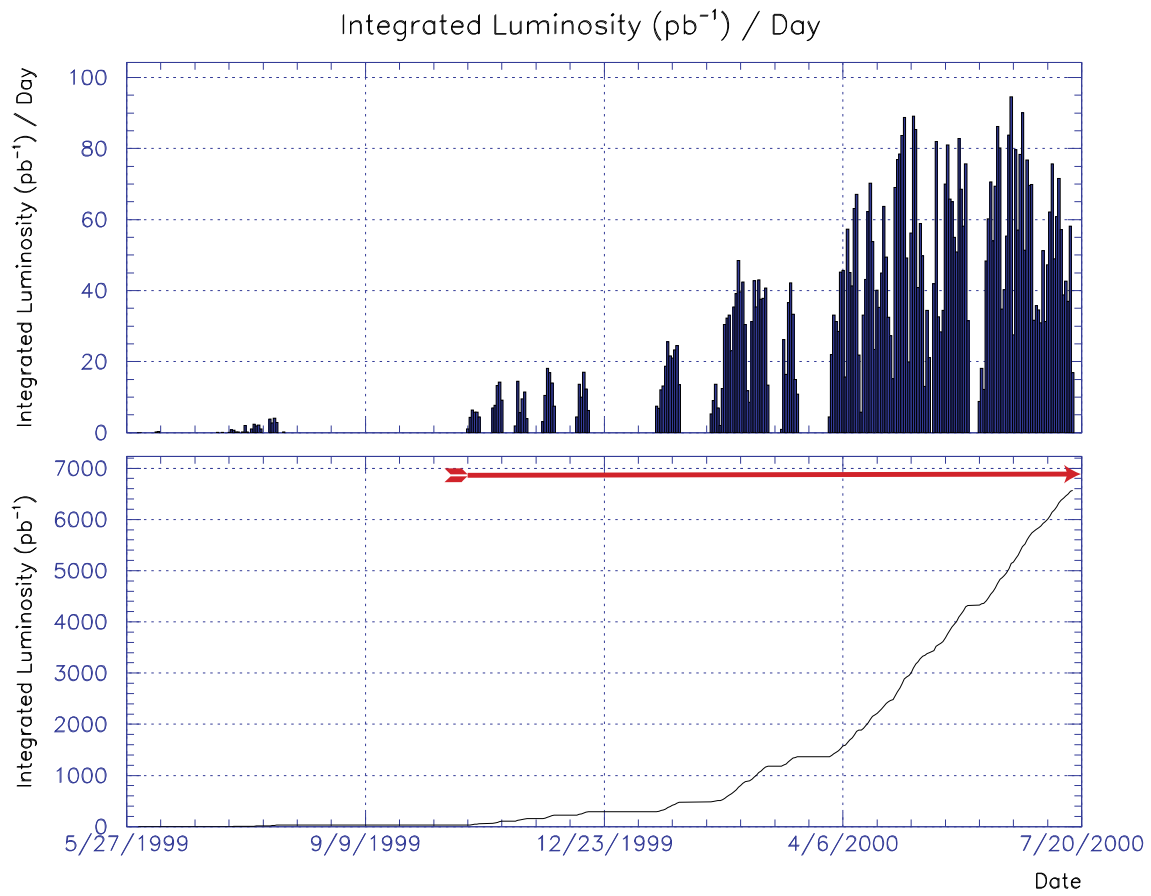
Figure 3.15: History of integrated luminosity of KEKB.

Parameter	LER	HER	Units
Particles	e^+	e^-	
Energy (E)	3.5	8.0	GeV
Circumference (C)	3016.26		m
Luminosity (L)	2×10^{33} (1×10^{34})		cm^{-2}s^{-1}
Crossing angle (θ_x)	± 11		mrad
Tune shifts (ξ_x/ξ_y)	0.039/0.052		
Beta function at IP (β_x^*/β_y^*)	0.33/0.01		m
Beam current (I)	0.7 (2.6)	0.5 (1.1)	A
Natural bunch length (σ_z)	0.4		cm
Energy spread (σ_E/E)	7.1×10^{-4}	6.7×10^{-4}	
Bunch spacing (s_B)	0.59		m
Particles/bunch	3.3×10^{10}	1.4×10^{10}	
Emittance $(\varepsilon_x/\varepsilon_y)$	$1.8 \times 10^{-8}/3.6 \times 10^{-10}$		m

Table 3.1: Present parameters of KEKB. () are the design value.

Chapter 4

KLM detector

In this chapter we describe the KLM system. Glass-electrode RPC module, High Voltage system, gas supply and exhaust system, and signal readout system are described.

4.1 Introduction

KLM is the subdetector system that is designed to identify K_L and muon with the momentum above ~ 600 MeV/c with high efficiency [18].

Since muons are produced in many of B decay modes, its identification is quite important for the measurements such as B flavor from semileptonic decay, $J/\psi \to \mu^+\mu^-$ and rare B decays.

Since K_L is a neutral hadron, it rarely interacts with the inner detectors. So K_L detection is performed by finding the hadron shower in the electromagnetic calorimeter and the KLM.

Figure 4.1 shows a schematic view of the KLM. It consists of an octagonal barrel detector and two endcap detector that are divided into quadrants. Both part have a structure of alternating layer of 47 mm thick iron plates and 44 mm thick slots where RPCs (resistive plate chamber) are mounted. The detail of RPC is described in the next section. The iron plate is an absorber material in KLM and also serves as a return path of the magnetic flux provided by superconducting solenoid. There are 15 slots in the barrel and 14 in the endcap. The overall detector coverage area is about 2000 m^2.

The detector component of KLM consists of a unit of RPCs and readout strips which is called "module". The barrel modules are rectangular in shape and vary in size from 220×151 to 220×267 cm^2. The endcap modules are in fan shape, and the inner radius is 130.5 cm, outer radius is 331 cm. The thickness of both module is 3.9 cm.

The KLM covers the polar angle range of $25° < \theta < 145°$. The number of readout channel is 21,856 in barrel and 16,128 in endcap.
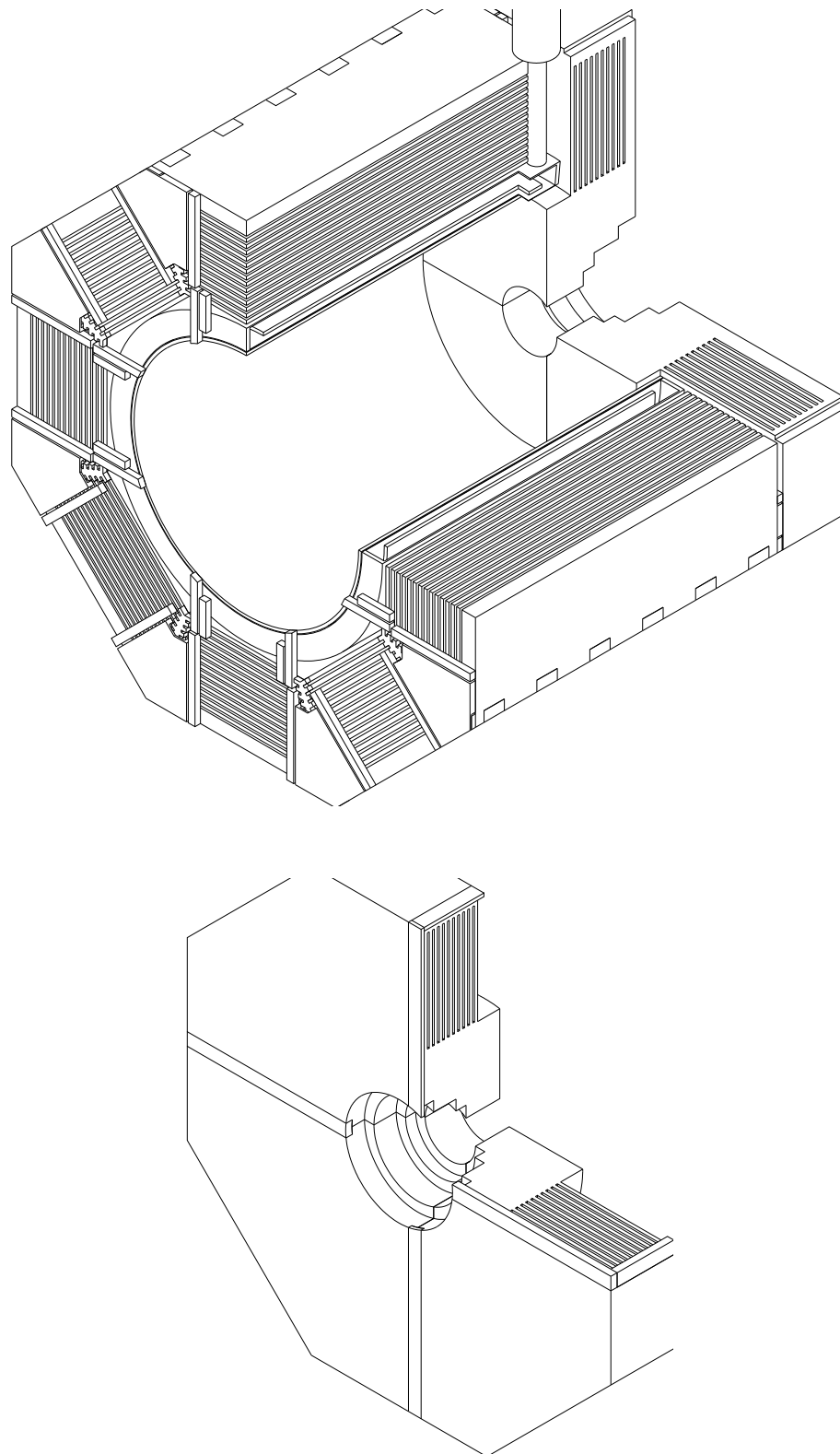
Figure 4.1: Schematic view of barrel and endcap KLM.

4.2 Glass-electrode RPC

The RPC is essentially like a planer spark counter wherein the avalanche induced by an incident charged particle is quenched when the limited amount of charge on the inner surface of high resistive electrodes is exhausted.

The RPC has features as follows.

- Signal pulse height is high ($\sim$ several 100 mV) enough to operate without amplifier.

- Good time resolution ($\sim$ several nsec).

- Easy to build. Have freedom in size and shape.

- Not so expensive.

We have chosen the float glass plate as the electrodes of RPC after various resistive plates were tested. It has a volume resistivity of $\sim 10^{12}$ Ω·cm. The electrode is covered with carbon coating with a surface resistivity of $\sim 10^7$ $\Omega/\square$ to distribute the high voltage. There are spacers between two glass electrode to hold the 2 mm gap, which also makes the path of the gas flow. Figure 4.2 shows the typical signal shape of our glass-electrode RPC. The signal typically has a few 100 mV peak into a 50 Ω termination, and have a full width at half maximum of less than 50 nsec. The rise-time of the signal is of the order of 1 nsec.
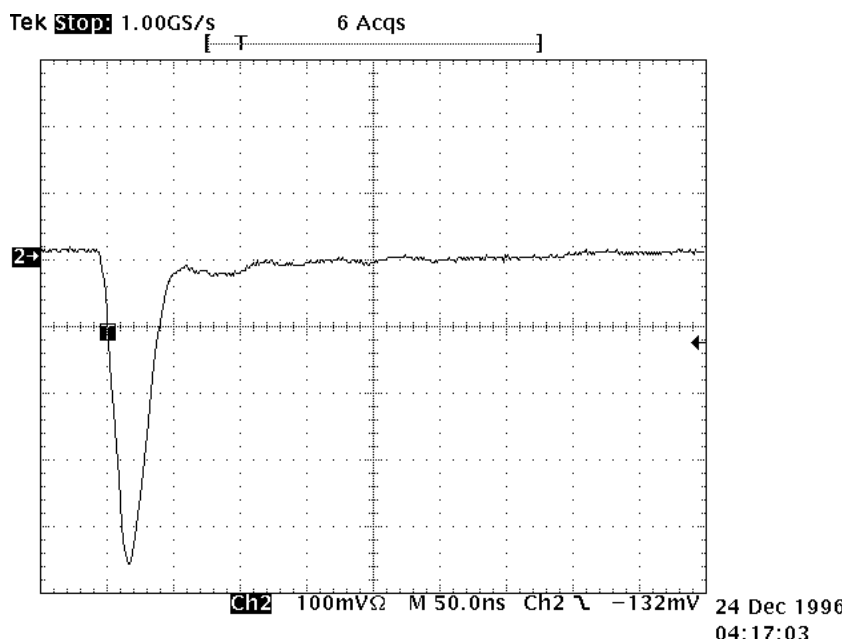
Figure 4.2: Typical signal of Glass-electrode RPC.

A schematic view of the barrel RPC is shown in Figure 4.3. The endcap module contains 10 pie-shaped RPCs as shown in Figure 4.4.

Figure 4.5 shows the cut-away view of an endcap RPC superlayer module with 96 ϕ and 48 θ pickup strips. The superlayer structure is described in next section.
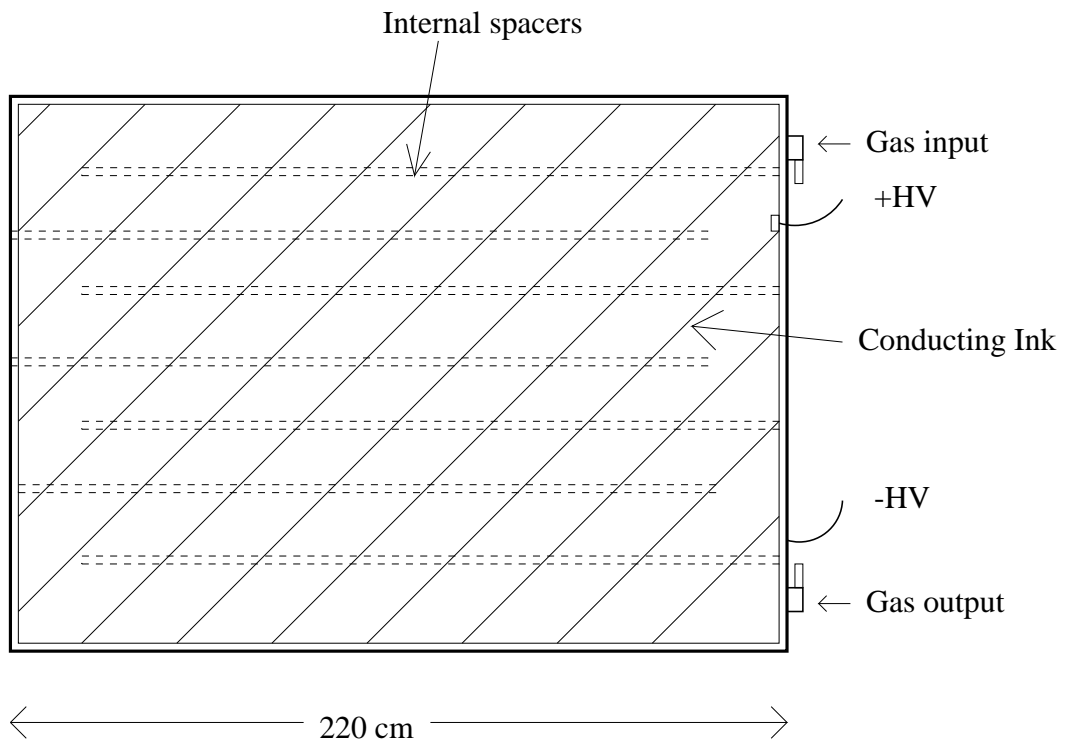
Internal spacers

Figure 4.3: Barrel RPC showing internal spacers.
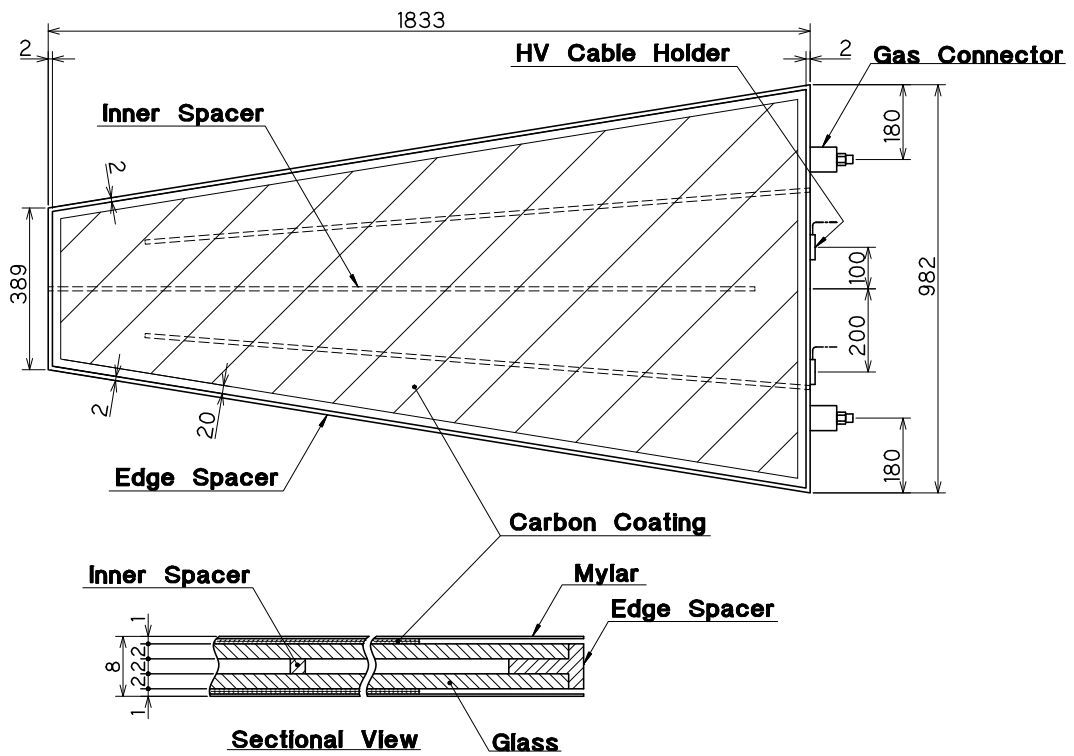
Figure 4.4: Endcap RPC showing internal spacers.
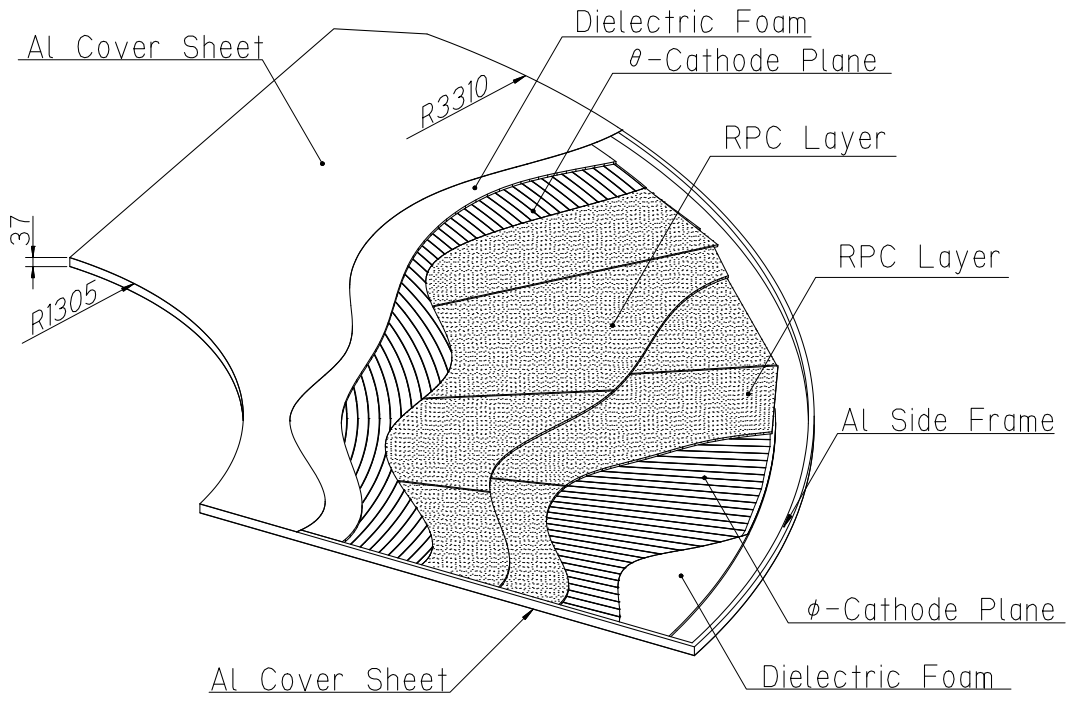
Figure 4.5: Cut-away view of an endcap RPC module.
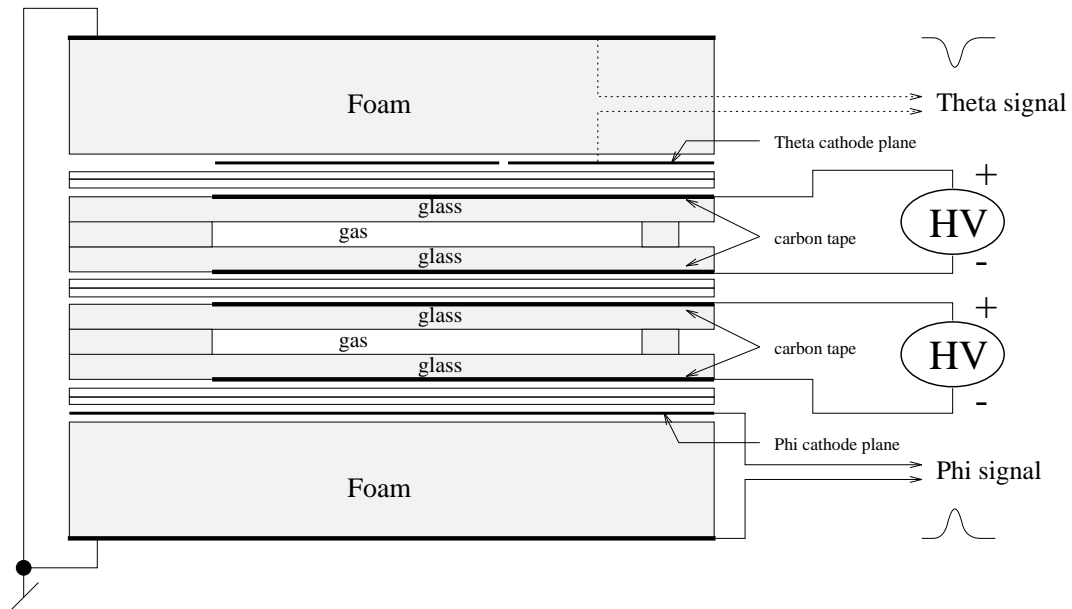
Figure 4.6: Superlayer structure.

4.3   Superlayer structure

The superlayer structure consist of two RPCs sandwiched between orthogonal pickup strip planes as shown in Figure 4.6. The HV is supplied to the same direction for two RPC layers so that both readout planes could produce signals when either RPC fires. This design minimizes the effect of dead regions between gaps in adjacent RPCs and near the internal spacers by offsetting their locations for two RPCs that comprise a superlayer, which result in a high efficiency.

4.4   Gas system

We have chosen the gas mixture of 30% argon, 62% HFC134a, and 8% butane-silver(iso-/n-$\sim$25/75), which is environmentally friendly and non-flammable and provides high detection efficiency and stable RPC operation[19].

Figure 4.7 shows the block diagram of the KLM gas distribution. Mixed gas is supplied to each RPC in a superlayer so that if one supply line fails the other will still be operational. To insure the uniform gas distribution for 704 channel, "Flow Registers" which is a 10 cm long stainless steel tube of 254 μm diameter are inserted upstream of the RPC. Since mixed gas is heavier than air, the gas, that fills the 20 m vertical exhaust line to the ground level, exerts about 40 mmAq pressure to the RPCs, which might damage them. We use Venturi pump to control the exhaust pressure differential to be nearly zero. The exhaust system is shown in Figure 4.8.

During initial operation, we experienced a damage of the electrode surface which is caused by water vapor. We found it from the increase of dark current and corresponding decrease of efficiency. The water vapor was migrating through the polyolefin tubings, and the concentration of H_2O was measured to be about 2000 ppm in some exhaust lines. By replacing the polyolefin tubing with copper tubing, the contaminated RPCs eventually dried out and have recovered the efficiency. Now careful control and monitor of water vapor in the gas are made by the water filters and dew point meters. Interlock system turns off the HV to protect the glass surface if abnormal gas mixture is detected.

4.5   HV system

RPCs are operated in a limited streamer mode. Applied high voltage is fixed to +4.7 (+4.5) kV for anode plane of barrel (endcap) RPCs and −3.5 kV for cathode plane for barrel and endcap RPCs. Dark current of individual layer is carefully monitored since efficiency becomes lower when the current exceeds the nominal value of $\sim$ 7 μA per one RPC layer.
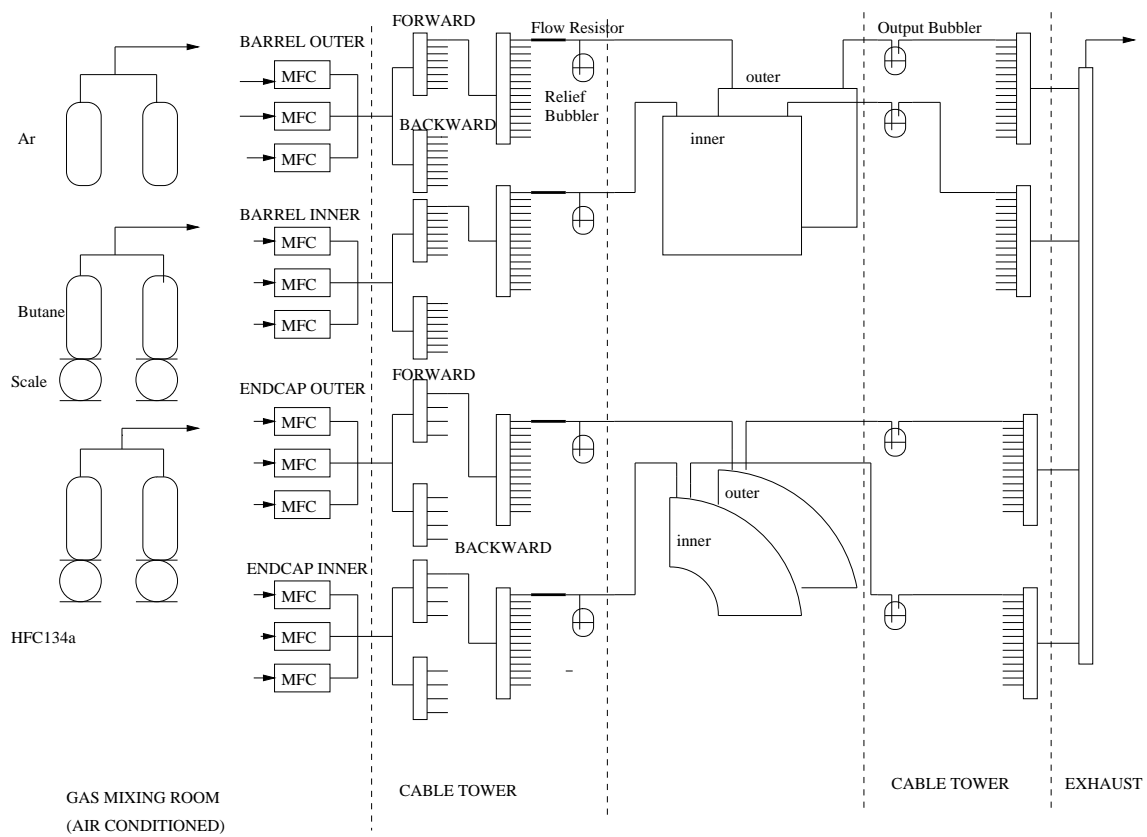
Figure 4.7: KLM gas distribution system.
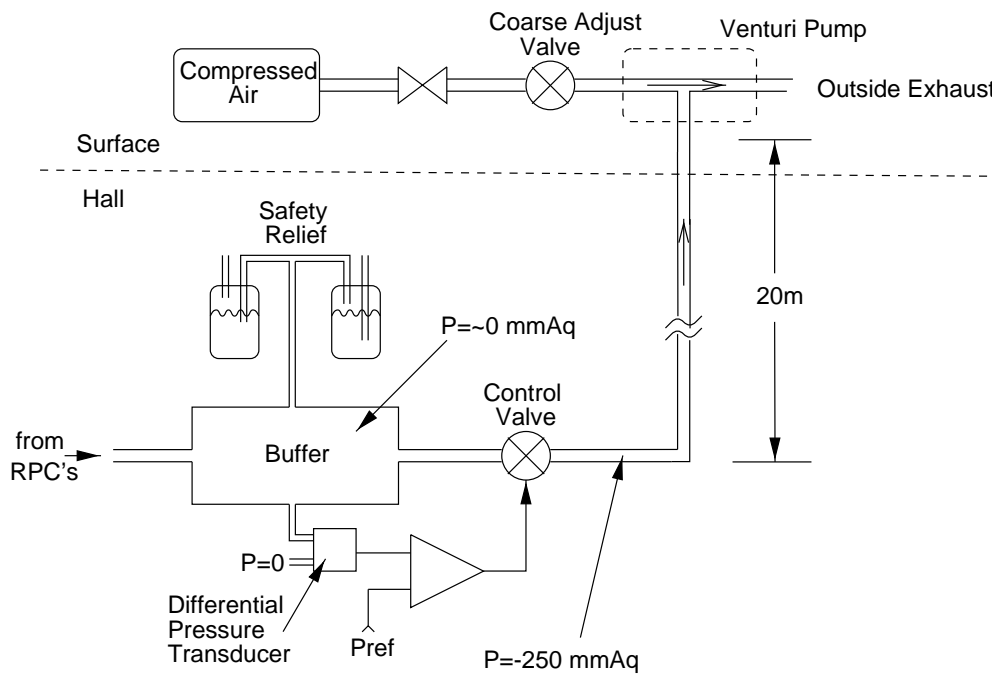
Figure 4.8: KLM gas exhaust system.

4.6 Readout system

The readout system consists of custom-made VME discriminator and FASTBUS pipeline TDC which is the standard BELLE digitizer. We have total 38 K channel of signal readouts of RPC. Time multiplex scheme, a kind of parallel-to-serial conversion, is used to reduce the number of TDC by factor of 1/12. This scheme is shown in Figure 4.9. The fraction of dead channels in whole system is about 0.3%. Most of them are due to the defect of connection of the strip and signal lines in the RPC module.
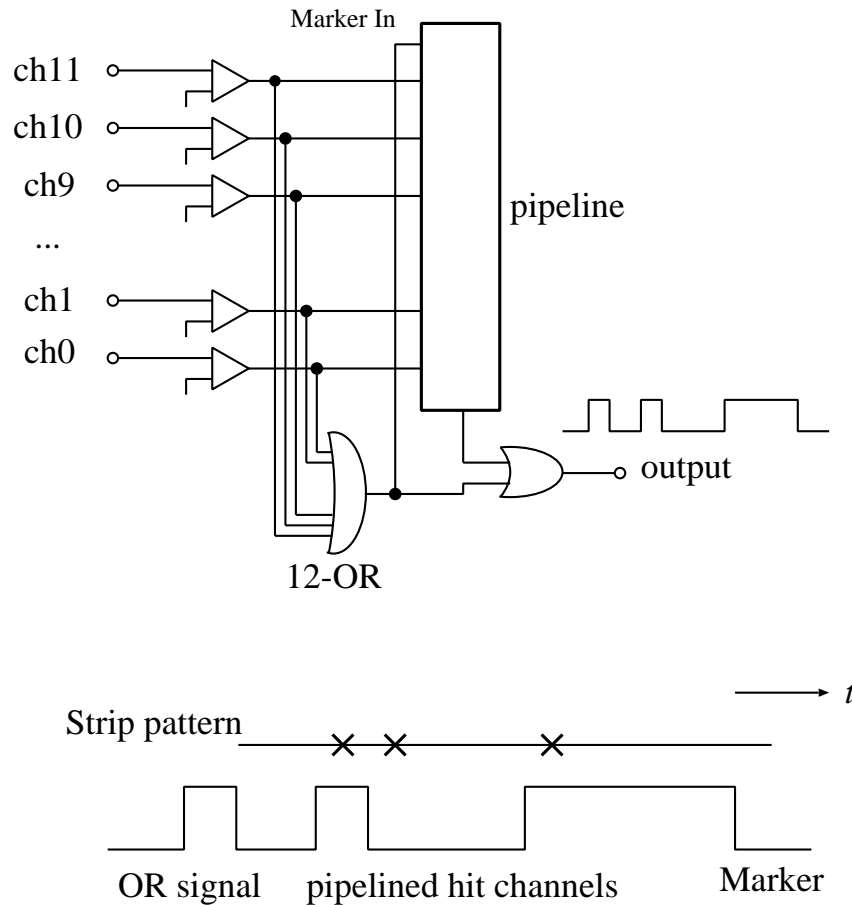
Figure 4.9: Time multiplex scheme.

4.7 Efficiency and resolution

Figure 4.10 shows the efficiency of endcap RPC module as a function of HV in cosmic ray measurement. The lower 2 lines are for the case when only one RPC layer of the superlayer is active, and the upper line is for the case when both RPC layers of the superlayer are active. The efficiency was obtained by triggering on and tracking a particle using the other layers, calculating the expected location of the

track as it passed through this layer, and looking to see if a hit was recorded at that location (± 1 strip). The efficiency is the ratio of the number of hits found to the number expected. Figure 4.11 shows the efficiency map with a grid determined by the readout strip. The size of the box indicates the efficiency of the grid. When only one RPC layer of the superlayer is active, the edges of each RPC and the region near the internal spacers are clearly seen as inefficient regions. When both RPC layer are active, the superlayer acts as a logical "OR" for hits of either RPC layer. Since care was taken to insure that the edges of RPCs in the two RPC layers do not overlap, we obtain the uniform efficiency that is typically over 98%.

Figure 4.12 shows the spatial resolution of the modules. This residual distribution shows the difference between the measured and predicted hit location using the track that has been fitted using hits in the adjacent layers. The multiplicity referred to is the number of adjacent strips that produces signal. When this strip multiplicity is more than one, the hit location is determined as the center of the strips. With one or two strips hit the standard deviation is 1.1cm. With three hit strips it is 1.7cm, and with four hit strips it is 2.9cm. The multiplicity-weighted standard-deviation is 1.2cm, which gives the angular resolution from the interaction point better than 10 mrad. The resolution is almost the same as that expected from strip size and assumption of uniform distribution of particles.

Figure 4.13 shows the Δt distribution of 2 KLM layers using cosmic lays. The time resolution of the KLM system is $\sim$ several nsec.
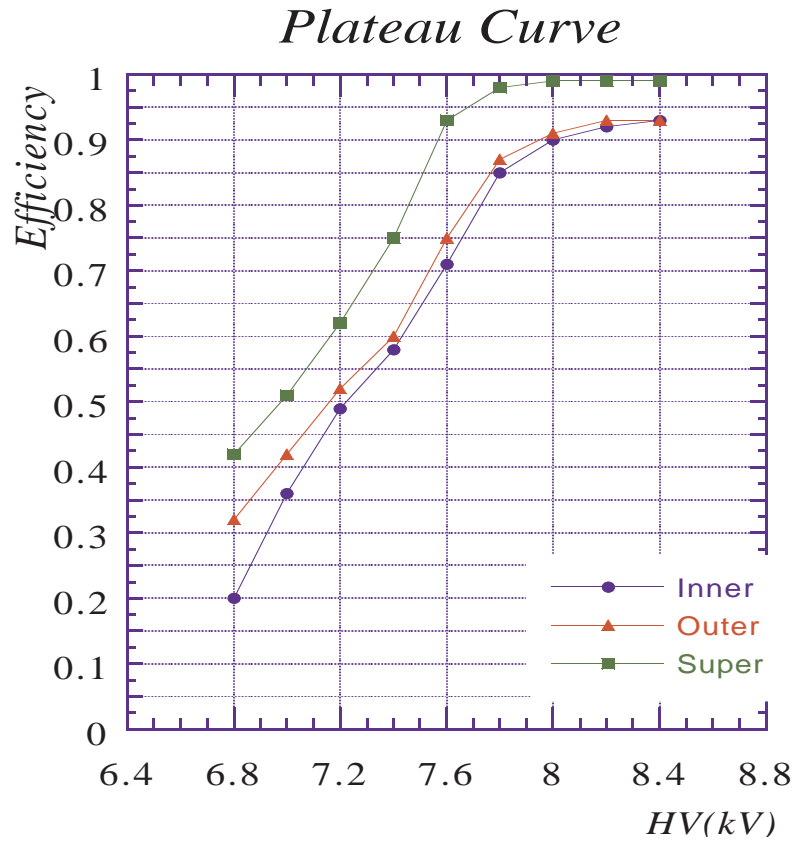
Figure 4.10: Efficiency of endcap RPC module as a function of HV. Lower 2 lines are for the case when only one RPC layer of the superlayer is active. Upper line is for the case when both RPC layers of the superlayer are active.
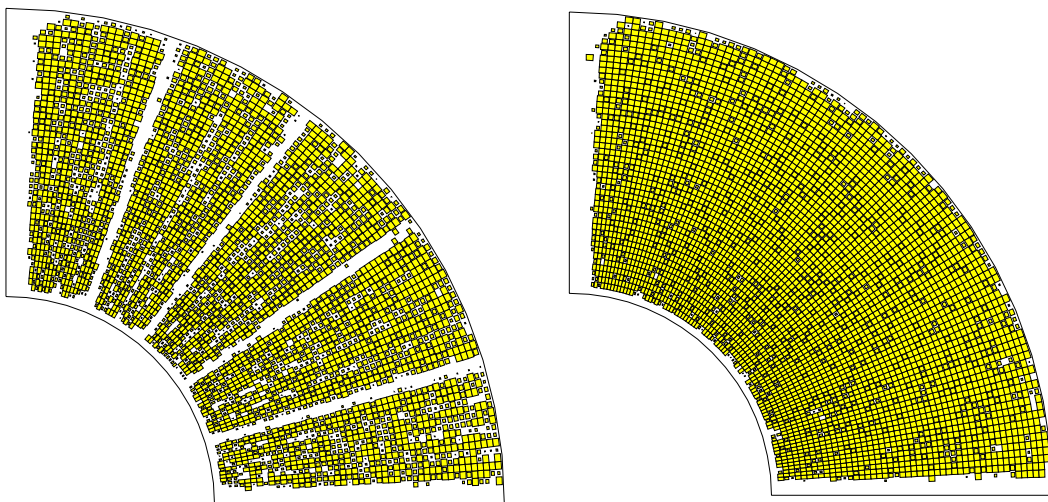
Figure 4.11: Efficiency map of RPCs in endcap module when only one RPC layer of the superlayer is active (left), and when both RPC layers of superlayer are active (right).
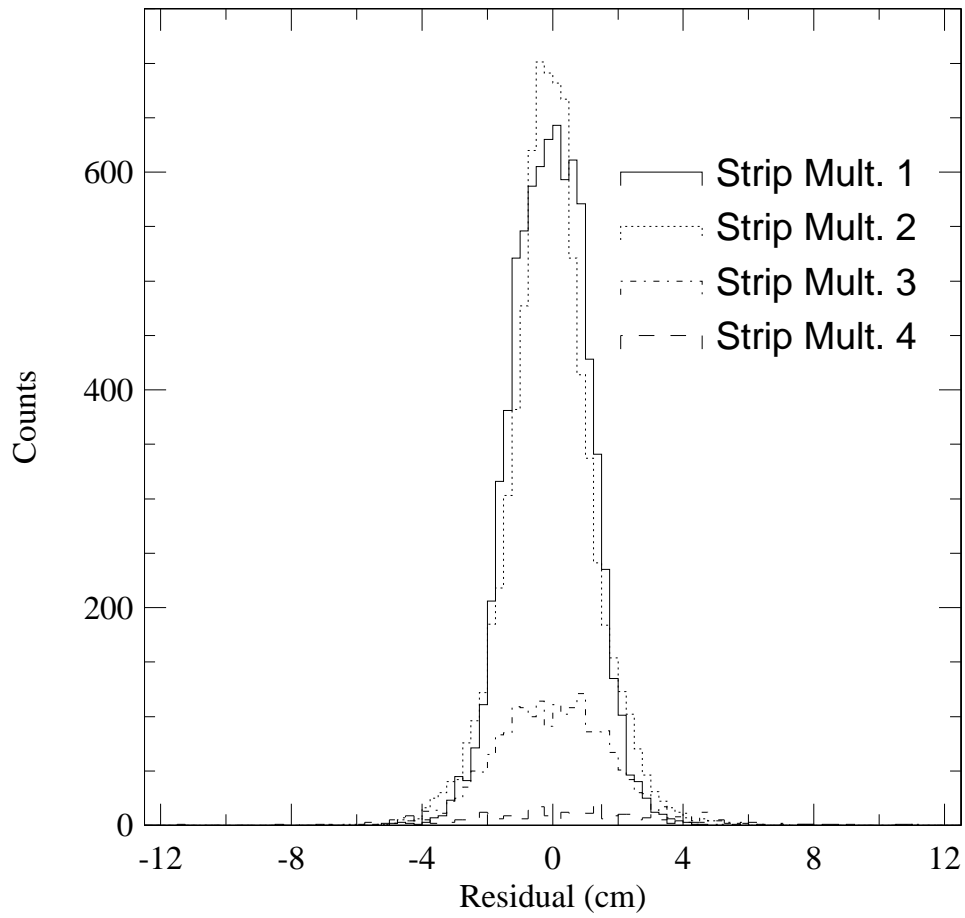
Figure 4.12: Spatial resolution of a superlayer.

ID	100
Entries	3605
χ^2/ndf	212.7 / 72
Constant	239.1
Mean	2.243
Sigma	5.274

Time Resolution (nsec)
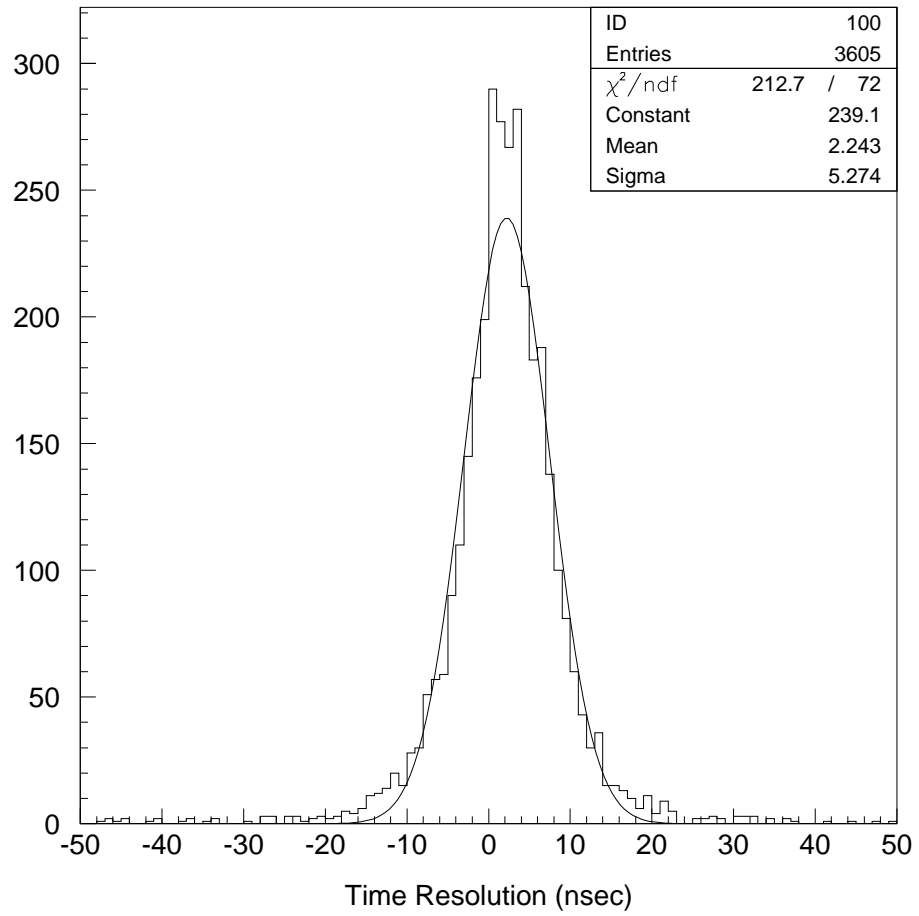
Figure 4.13: Time resolution of KLM system.

Chapter 5

Software Tools

In this chapter we describe the software tools for data analysis and for Monte Carlo simulation of the Belle detector.

5.1   Overview

Figure 5.1 shows the general framework of data analysis and Monte Carlo simulation in the Belle experiment. The raw data taken by the Belle DAQ are processed by reconstruction tools, such as charged particle tracker, energy measurement and particle identifications. Output of reconstruction tools are stored into Data Summary Tape (DST). For physics analysis, DSTs are converted to the more convenient and compact subset of data, so-called Mini-DST (MDST).

For Monte Carlo simulation, we have two detector simulator : full detector simulator and fast detector simulator. The full detector simulator generates detector response in the same way as the real detector generates it. Data generated by full detector simulator is processed by the reconstruction tools, and subsequent process is the same as in the real data. The fast detector simulator uses the parameterized detector performances, and generate Mini-DST data directly.

Analysis and simulation tools consist of many program modules which are executed on a common framework, BASF/FPDA [20]. Data are managed by the bank system, PANTHER [21], which is based on entity relationship model [22]. PANTHER can be used from either FORTRAN, C or C++ languages.

5.2   Reconstruction tools

For the event reconstruction for physics analysis, it is necessary to perform charged particle tracking, energy measurement and particle identification.

5.2.1   Charged particle tracking

The charged particle tracking tries to find all tracks in the event and reconstruct them, and provide the coordinate, momentum, energy deposit (dE/dx), for each
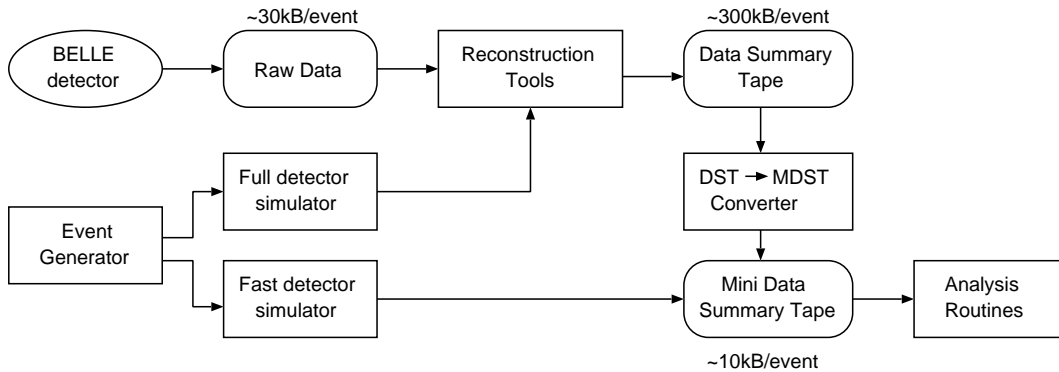
Figure 5.1: Flow of data analysis and Monte Carlo simulation.

track.

First, the CDC hit points that are associated to the track are selected. Axial-wire hits of the CDC are used to project the track into the r-ϕ plane, and stereo-wire hits are used to calculate the z-position. Then, the fitting to the helix is done with those hits. After that, matching between hit points of SVD and the tracks is performed, then the refit is done by the Kalman filtering method.

The tracks are extrapolated to the outer detector positions by considering the change of magnetic field and energy loss in the material of detector components.

5.2.2   Energy reconstruction

Since photons and electrons which pass through ECL deposit most of their energy in crystals, it is necessary to reconstruct the energy of crystals to measure the total energy deposit of them.

First, a seed crystal which has the highest energy deposit among the neighboring crystals is searched for. Total energy in 3×3 crystals (E_9) and 5×5 crystals (E_{25}) around the seed crystal is calculated.

5.2.3   Particle Identification

Particle identification is necessary to distinguish the species of each particle. We made tools to identify $e^\pm$, $\mu^\pm$, $K^\pm$ and $\pi^\pm$ with excellent performance. We also designed a tool to detect K_L, which is necessary in particular for $B^0 \to J/\psi + K_L$ analysis.

- **Electron identification**

Electron identification is performed by measuring the ratio of energy deposit in the ECL and momentum (E/p). It is around 1.0 for electron. The transverse distribution of electromagnetic shower with respect to the direction of incident electron is also narrower than that of hadrons.

For electron identification, E/p is the main method. In addition to it, we use matching information of track and ECL cluster, shower shape, dE/dx in the CDC, light yield in the ACC, and time of flight measured by the TOF.

Figure 5.2 shows the efficiency and fake rate of electrons as a function of momentum, which are determined from the data. We used single electron Monte Carlo events embedded into the real hadronic events as electron samples, and $K_S \to \pi^+\pi^-$ events as pion samples. The upper limit of electron contamination in $K_S \to \pi^+\pi^-$ sample, which is relevant for the fake rate, is estimated to be less than 0.08% with the Monte Carlo study.

The details of electron identification is described in [23].
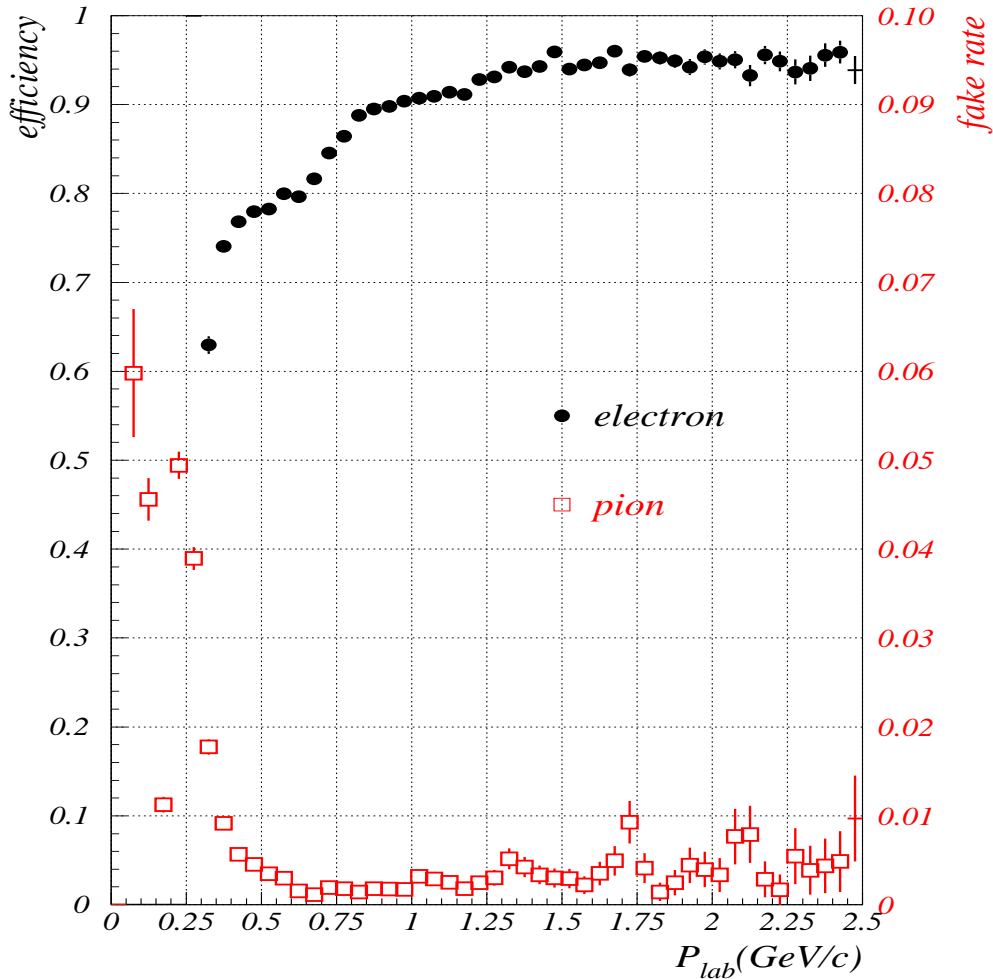
Figure 5.2: Efficiency (filled circle) and fake rate (open box) of electron identification.

• Muon identification

Muon is more penetrative than any other charged particle since muon is massive and does not produce electromagnetic shower. Charged tracks are extrapolated to KLM region, then KLM hits nearby the track are collected. The track extrapolation is performed by Kalman filtering method inside the KLM region.

Use of hit information of the KLM is the main method for muon identification. The depth of KLM hits shows ΔR which is the difference between the measured and expected range of track. The spread of KLM hits shows χ_r^2 which is the normalized transverse deviations of all hits associated with the track. Probability density distributions of ΔR and χ_r^2, obtained from Monte Carlo single track of muons, pions and kaons, are used to calculate the likelihood.

Figure 5.3 shows the efficiency and fake rate of muons as a function of momentum, which are determined from data. We used $e^+e^- \to (e^+e^-)\mu^+\mu^-$ events as muon samples, and $K_S \to \pi^+\pi^-$ events as pion samples. The purity of muon samples in $e^+e^- \to (e^+e^-)\mu^+\mu^-$ and $K_S \to \pi^+\pi^-$ is estimated to be 97% and 99.8% with Monte Carlo study, respectively.

The details of muon identification is described in [24].

• K/π separation

The separation of kaons and pions is basically performed by using the mass difference of them. We have the TOF and the ACC that are mainly aimed for this separation. dE/dx information of the CDC is also used.

Time of flight information from the TOF is used to measure the velocity ($\beta = v/c$) of the particle. From β measured by the TOF and momentum p measured by the CDC, mass m can be calculated as

$$p = \frac{mc\beta}{\sqrt{1-\beta^2}} \equiv mc\beta\gamma. \tag{5.1}$$

This method is applicable for the particle of momentum below 1.2 GeV/c.

The ACC is a threshold type detector which makes use of Čerenkov light. When a charged particle pass through a material with refractive index n, the Čerenkov light is emitted in the condition of

$$\beta > \frac{1}{n} \tag{5.2}$$

From Equation (5.1) and (5.2), the threshold momentum is expressed as

$$p > \frac{mc}{\sqrt{n^2-1}} \tag{5.3}$$

Refractive index is selected so that the Čerenkov light is emitted for pion and not for kaon in higher momentum range ($1.2 < p < 3.5$ GeV/c). If an extrapolated track has associated hits in ACC, it is identified as pion.
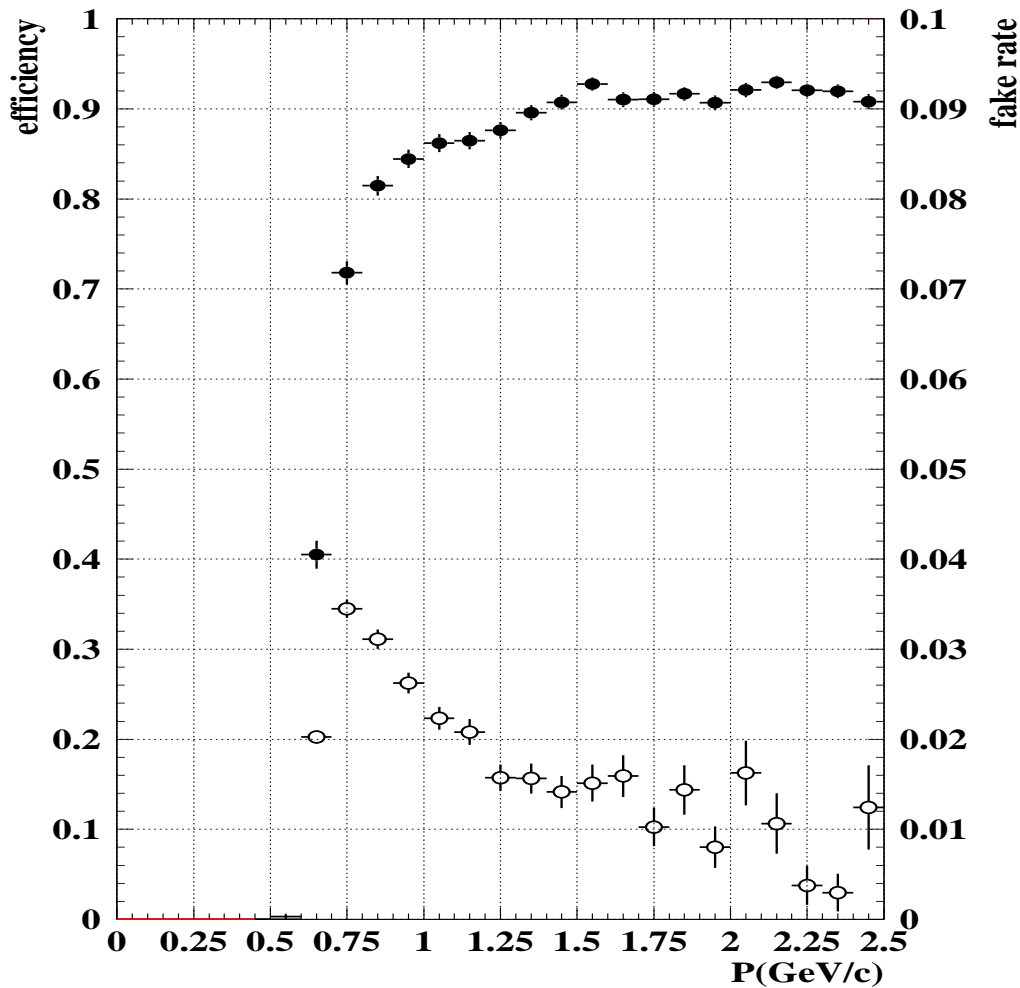
Figure 5.3: Efficiency (filled circle) and fake rate (open circle) of muon identification.

The likelihood is calculated from the combination of information from the CDC, ACC and TOF. Figure 5.4 shows the momentum coverage of each detector component. Figure 5.5 shows the efficiency and fake rate of kaons as a function of momentum, measured with $D^{*+} \to D^0(K\pi) + \pi^+$ decay sample. The contamination of the sample by the combinatorial background is estimated to be 2.3% from the fit to the mass difference distribution between reconstructed D^{*+} and D^0 mesons.

The details of K/π separation is described in [25].

- K_L **detection**

The K_L candidates are identified by the combination of the hit information of the ECL and the KLM.

Since the K_L detection is crucially important for $J/\psi K_L$ analysis, we describe
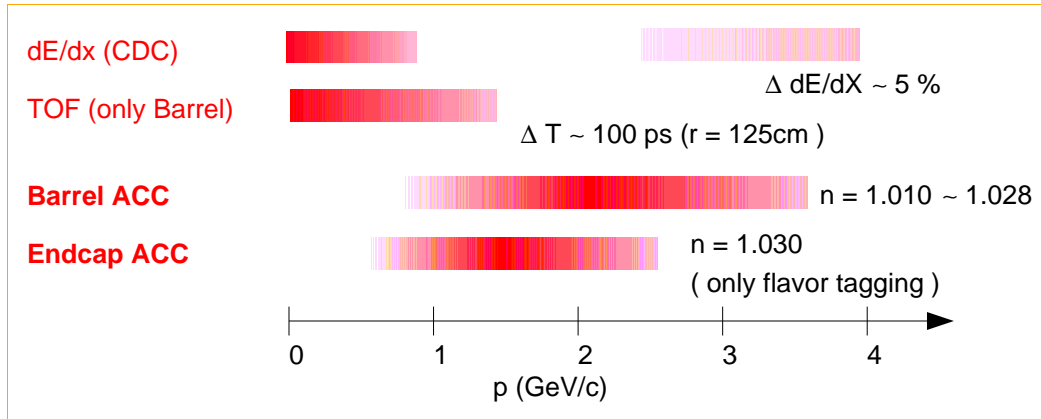
Figure 5.4: Momentum coverage of each component for K/π separation.
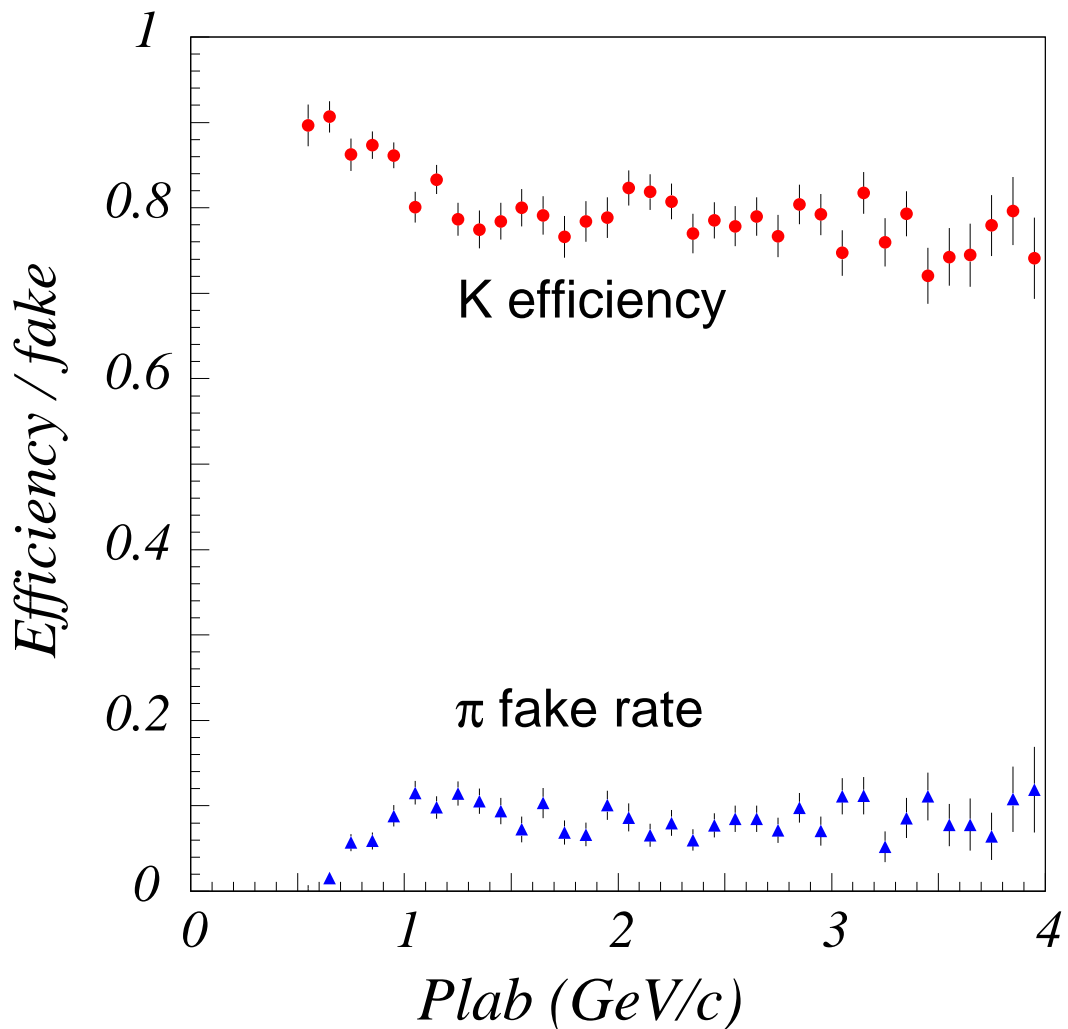
Figure 5.5: Efficiency (circle) and fake rate (triangle) of K by K/π separation routine, measured with $D^{*+} \to D^0(K\pi) + \pi^+$ decay.

the details in the next chapter.

5.3 Monte Carlo simulation

Monte Carlo simulation is necessary to know the reconstruction efficiency and the background contamination.

5.3.1 Event generator

The event generator simulates the physical process of particle decay chain. The initial state is $\Upsilon(4S)$ or $q\bar{q}$ (for continuum) and the final states consist of stable particles. We use QQ [26] event generator originally developed by CLEO group and modified to match the Belle experiment [27]. QQ can handle either $\Upsilon(4S)$ decays or continuum process. The decay of particle is performed according to the decay table which contains the decay modes and branching ratios measured by CLEO. User can control decay mode of any particle by changing the decay table. The output of QQ is stored into HEPEVT table [28] which includes production time, vertex position, 4-momentum, decay subproducts, etc.

5.3.2 Full detector simulation

The full detector simulator is based on GEANT3 [29], which is a library developed at CERN to simulate the passage of particles through the materials. GEANT system allows us to describe an experimental setup by a structure of geometrical volumes, and transport particles which are generated by an event generator through the various ranges of the setup, taking into account geometrical volume boundaries and physical effects according to the nature of particles themselves, their interactions with matter and the magnetic field.

The full detector simulation takes long time to process ($\sim$30 sec/event) since it traces all particle step by step computing reactions with materials.

5.3.3 Fast detector simulation

The fast detector simulator was developed [30] to save processing time when we simulate a large number of background events.

The fast detector simulation takes the particles from the event generator as an input, and calculate the detector responses with smearing functions based on simple parameterization. Some of the smearing functions are determined from full detector simulation, some are based on the results of the beam tests, and others are from real data if it is possible to use. The fast detector simulator produces the Mini-DST format output data directly. The fast detector simulator could not take into account the effect of secondary particles generated by the reaction of particles and detector materials.

Chapter 6

K_L detection

In this chapter we describe the K_L identification method and its performance with the Belle detector.

6.1 K_L selection criteria

The K_L candidates are identified using the combination of the hit information of the ECL and the KLM. Following algorithm is used to select the K_L candidates.

1. Hit clusters are made by combining nearby KLM hits which are within 5° opening angles each other. This process is repeated until no more hit is found within 5° opening angle from each other. We call this hit cluster "KLM cluster".

2. KLM clusters are classified as charged or neutral. Each charged track found by inner tracker is extrapolated to the first layer of KLM, and the meeting point is joined to interaction point by a straight line. If this line is within the 15° cone around the KLM cluster direction, the KLM cluster is defined as being associated with the charged track, and is classified as charged cluster. Otherwise the cluster is classified as neutral cluster.

3. Calculate the direction of neutral KLM cluster for two different cases separately.

   - If the neutral ECL shower with energy(E_{ECL}) greater than 0.16 GeV is found within the 15° opening angle of the KLM cluster direction, the KLM cluster is said to be associated with the ECL shower, and we use the direction of ECL shower as the direction of KLM cluster.

   - If no ECL shower is found to associate to KLM cluster, we use the direction of the center of KLM cluster as the direction of the KLM cluster.

4. K_L candidates are required to satisfy following conditions.

   - The KLM cluster is a neutral cluster.

47

- Number of hit layers in the KLM cluster must be ≥ 2 in the case of no associated ECL shower, and ≥ 1 when associated ECL shower is found.

Figure 6.1 shows the scheme of KLM hit clustering and determination of its direction. Figure 6.2 shows the scheme of matching of charged track and KLM hit cluster.
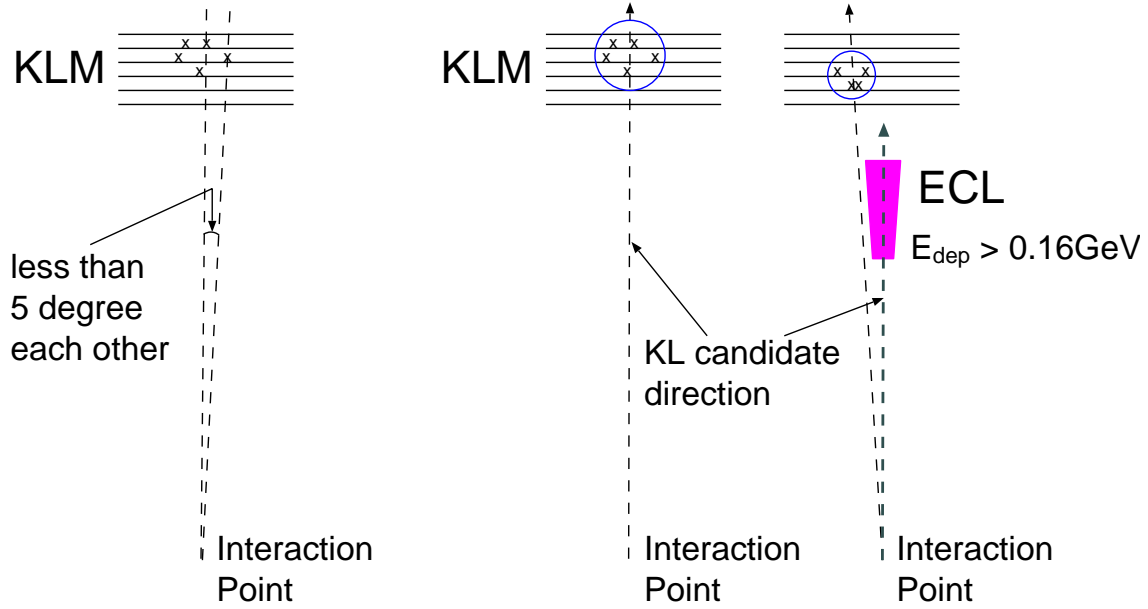
Figure 6.1: Schematic of KLM hit clustering (left) and determination of its direction for the case with and without an associated ECL cluster (right).
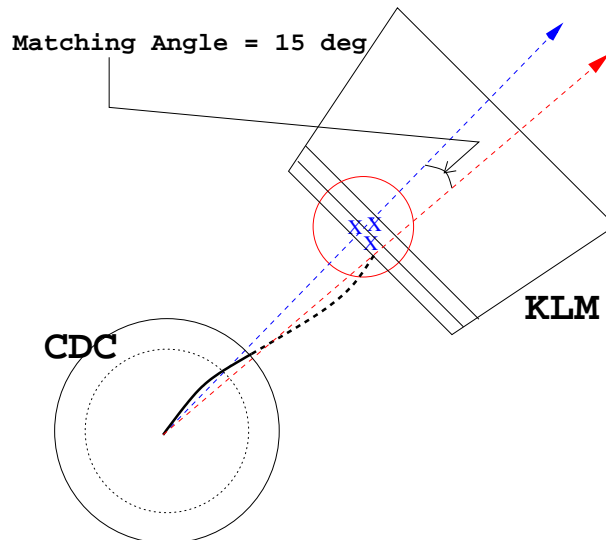
Figure 6.2: Schematic of matching of charged track and KLM cluster.

6.2 Performance

6.2.1 Detection efficiency

Figure 6.3 shows the K_L detection efficiency as a function of momentum in the laboratory frame, estimated by Monte Carlo single K_L events. Single K_L are generated uniformly in the momentum range between 0.3 and 4.5 GeV/c, $\cos\theta$ range between 25 and 150°, ϕ range between 0 and 360°. Figure 6.4 shows the K_L detection efficiency that is estimated using Monte Carlo $J/\psi K_L$ events. A strong momentum-$\cos\theta$ correlation of the K_L in this sample makes the efficiency vs momentum curve different from the single K_L case. Many of high momentum K_L in the $J/\psi K_L$ events go forward and suffer from the KLM acceptance cut-off.

We examined how the K_L detection efficiency in the $J/\psi K_L$ Monte Carlo events depends on the choice of charged track veto angle (normally 15°) and the ECL shower association angle (normally 15°). Figure 6.5 shows the veto-angle dependence of efficiency and average number of K_L candidates per event after removing K_L from $J/\psi K_L$. The latter quantity is a measurement of "fake" K_L rate per event. The efficiency decreases as the veto-angle becomes wider, slowly first and more rapidly above 20°. The fake rate decreases rapidly first as the veto-angle is widened, and slows down at around 15°. Based on these, we believe that a choice of 15° is reasonable.

Figure 6.6 shows the K_L detection efficiency and the fake rate as the ECL shower association angle is varied. The efficiency first increases as the association angle is widened, and then begins to decrease above 20°, reflecting a fact that true K_L is getting removed by being associated with random ECL hits. The "fake" rate also begins to increase above 20°. We believe that 15° is a reasonable choice.

6.2.2 Angular resolution

The angular resolution for K_L is estimated using Monte Carlo simulation. Figure 6.7 shows the differences between detected and generated direction of single K_L for two separate cases, without and with associated ECL shower. The Monte Carlo K_L are generated uniformly in the momentum range of 0.3 and 2.5 GeV/c, the $\cos\theta$ range of 25 and 150°, and the ϕ range of 0 and 360°. Angular resolution which is defined as the FWHM for those distributions is 3° for the case without associated ECL shower, and 1.5° for the case with associated ECL shower, and independent of the K_L momentum. The distribution have long tails. This tendency is more pronounced in the case of no associated ECL shower. This is due to a large fluctuation of hadronic shower pattern in the energy region of this experiment. The K_L direction is more precisely measured if the K_L interacts in the ECL, and the ECL shower position is used in this case.
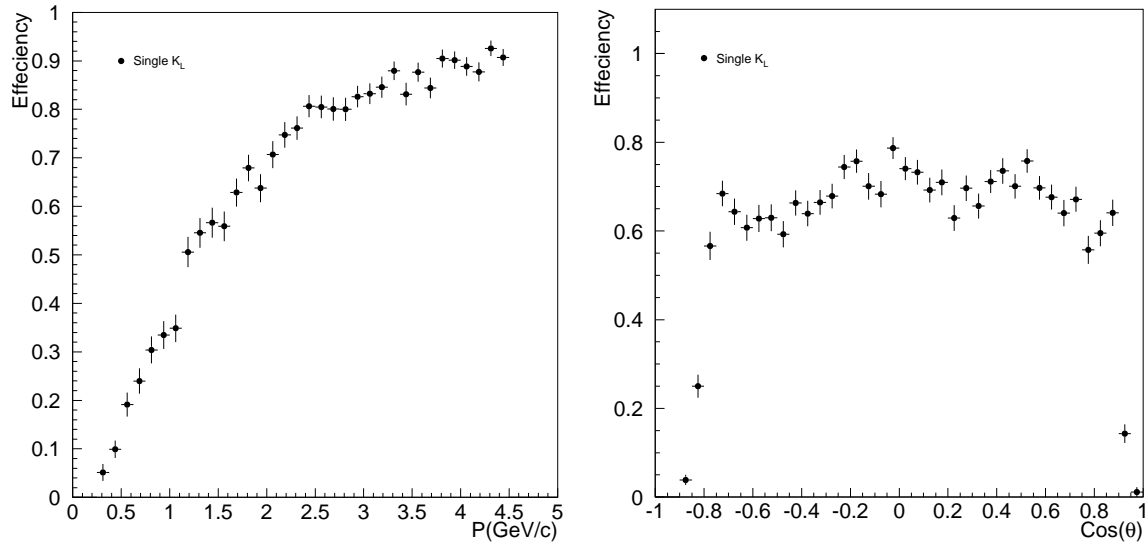
Figure 6.3: Momentum and $\cos\theta$ dependence of K_L detection efficiency determined using single K_L Monte Carlo events.
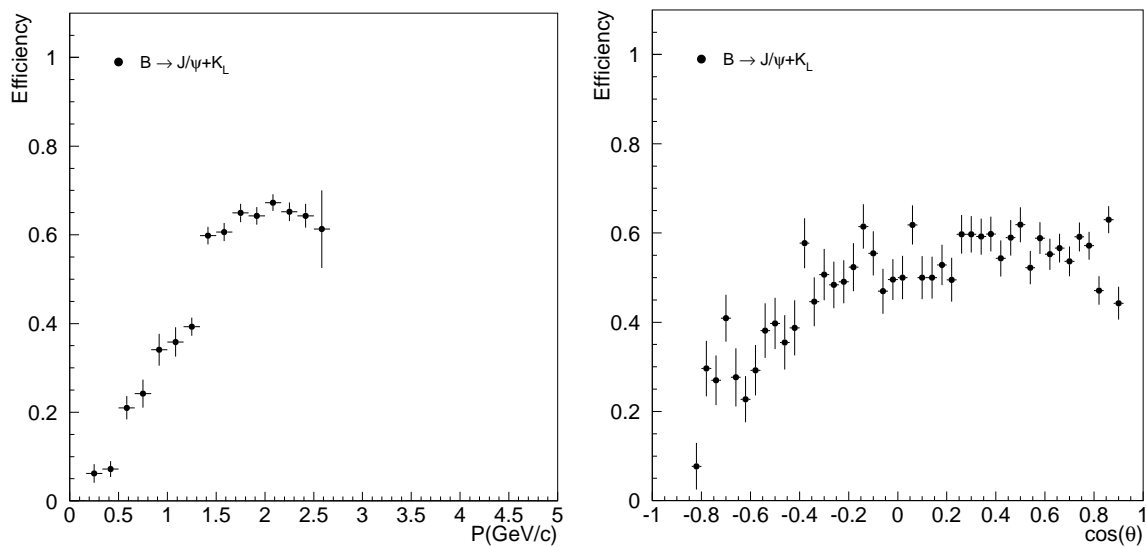
Figure 6.4: Momentum and $\cos\theta$ dependence of K_L detection efficiency determined using $J/\psi K_L$ Monte Carlo events.
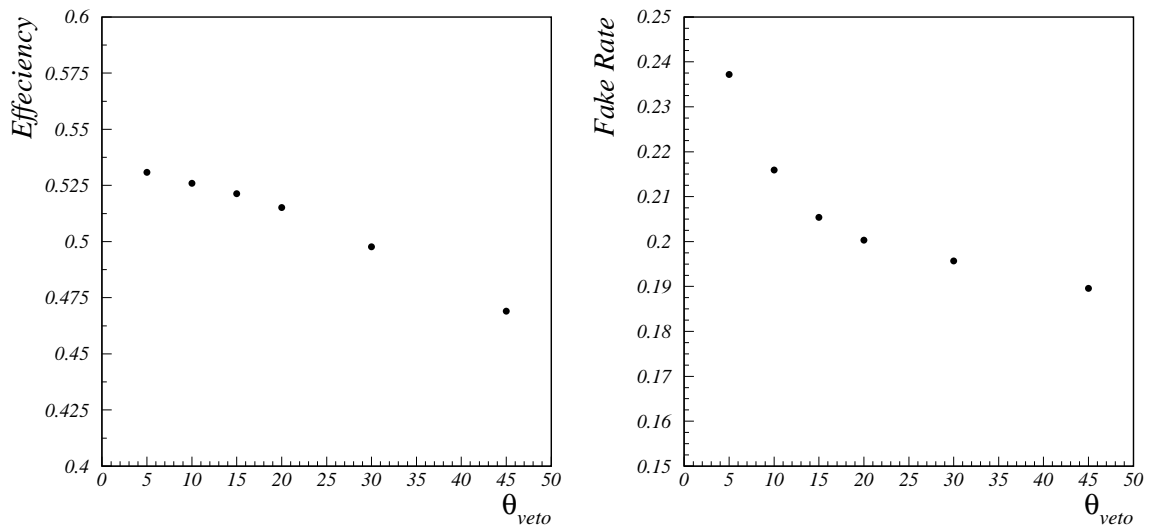
Figure 6.5: Charged track veto angle dependence of K_L detection efficiency (left) and "fake" K_L fraction (right) in the event.
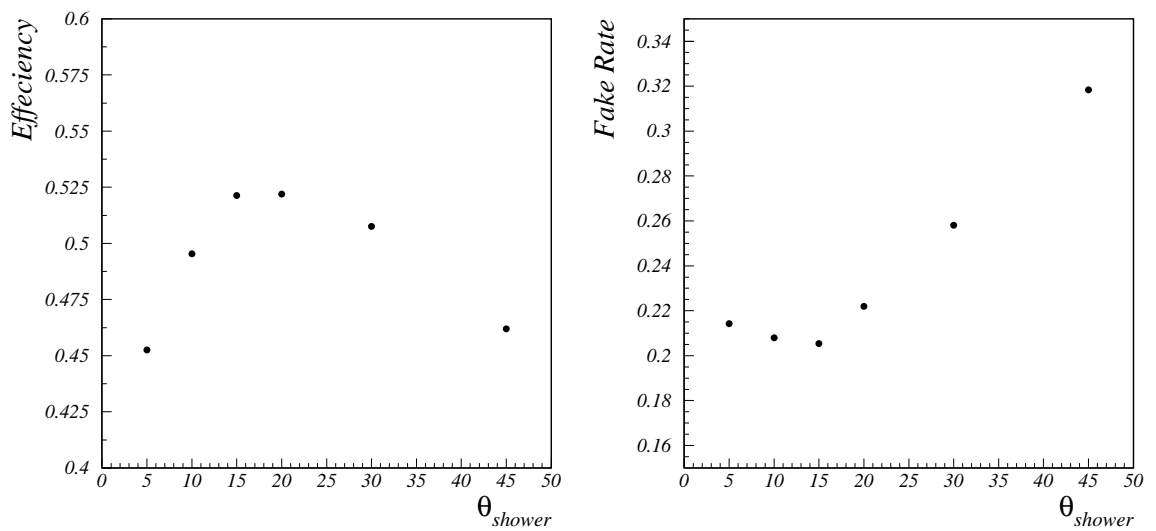
Figure 6.6: ECL association angle dependence of K_L detection efficiency (left) and "fake" rate (right).
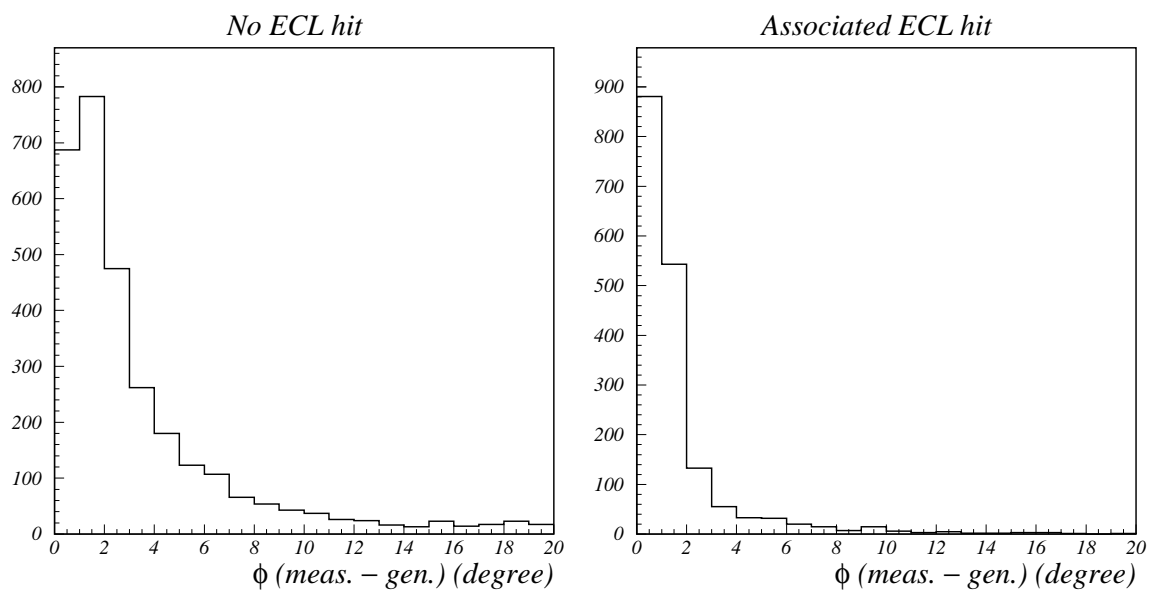
Figure 6.7: Difference between detected and generated directions of K_L. Distributions are made separately for the case with no associated ECL shower (left) and for the case with associated ECL shower (right).

6.3 Verification of K_L detection

6.3.1 ϕ angular difference between K_L and missing p_t.

We demonstrate K_L detection using real data. Figure 6.8 shows the ϕ angular difference between the K_L candidate direction and the missing momentum vector direction in an event. Circle shows the data, and histogram shows the Monte Carlo sample event. The missing momentum vector is calculated using all of other measured particles in the event. The histogram shows a clear peak where the K_L candidate cluster measured in the KLM is consistent with the missing momentum in the event. Large deviation of the missing momentum direction from the K_L candidate direction is mainly due to undetected neutrinos and particles escaping the detector acceptance. Although this is still an indirect evidence, this strongly indicates that we are detecting K_L.
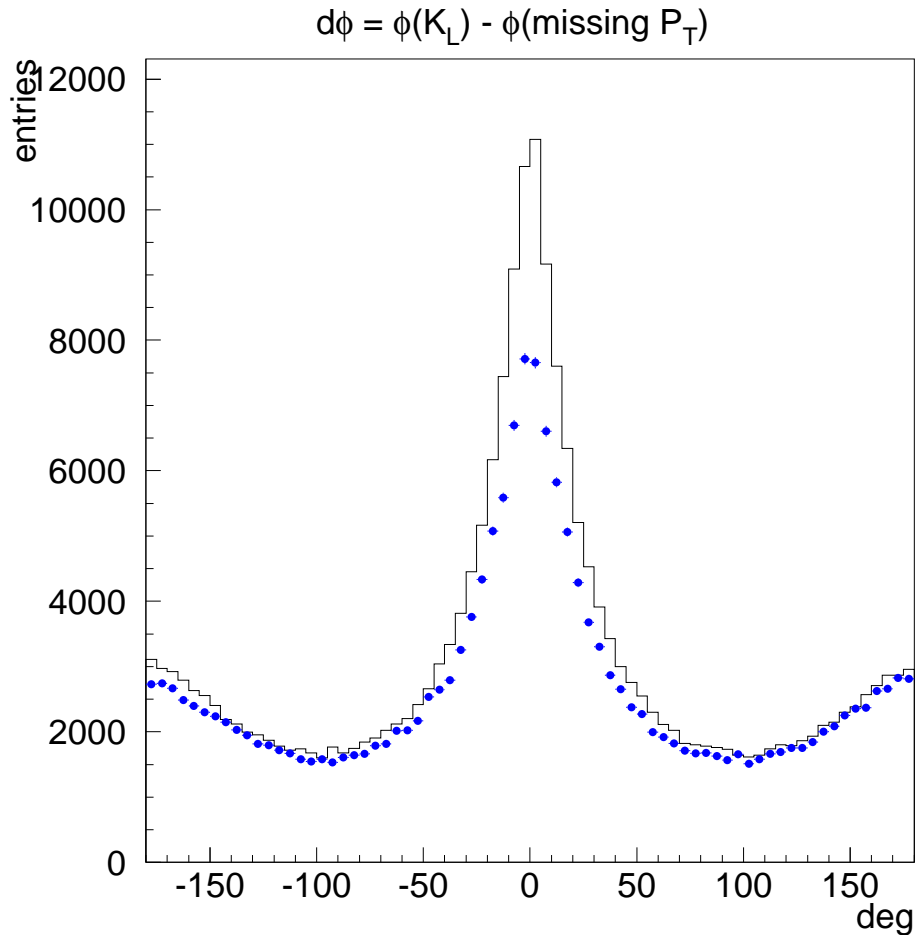
Figure 6.8: ϕ angular difference between the K_L candidate direction and the missing momentum vector direction. Circle shows the data, and histogram shows the Monte Carlo sample event.

6.3.2 $e^+e^- \rightarrow \gamma\phi$ event

We use $e^+e^- \rightarrow \gamma\phi$ decay mode with $\phi \rightarrow K_S K_L$ as a control sample for the verification of K_L detection [31]. The kinematics of the K_L can be completely predicted in this mode if we can detect the radiated high energy gamma and K_S.

Figure 6.9 shows the Feynman diagram of $e^+e^- \rightarrow \gamma\phi$ decay. This is similar to $e^+e^- \rightarrow 2\gamma$ where one gamma is replaced with ϕ.
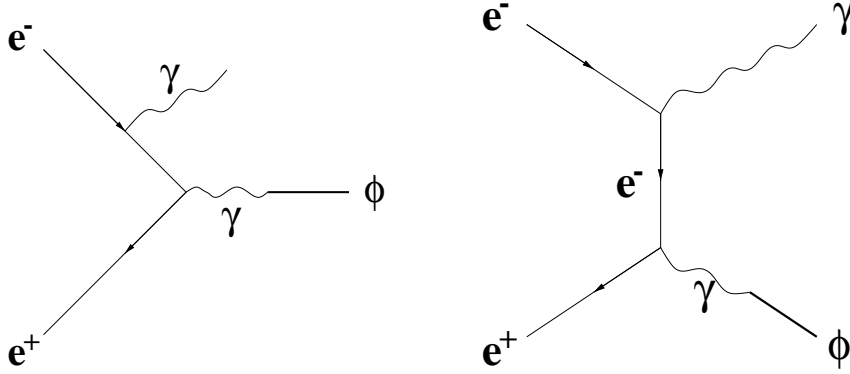
Figure 6.9: Feynman diagram of $e^+e^- \rightarrow \gamma\phi$.

We require following criteria to select $e^+e^- \rightarrow \gamma\phi(K_S K_L)$ candidate events.

- Require a photon that the center of mass energy of the gamma is in the range of $4.5 < E^*_\gamma < 5.5$ GeV/c.

- Require 2 oppositely charged tracks to form a K_S. Both tracks must not be identified as electron by electron identification routine in order to suppress the background from radiative Bhabha events. We also require that the magnitude of momentum of the track in the center of mass must satisfy $0.65 < p^*_{track} < 2.8$, and the θ direction of momentum of the track in the center of mass must satisfy $-0.85 < \cos\theta^* < 0.8$.

- The invariant mass of K_S must satisfy $0.490 < M_{K_S} < 0.506$ GeV/c^2. The decay vertex of K_S must satisfy $r > 2$ mm in $r - \phi$ plane in order to remove fake K_S. We also require the K_S momentum in the center of mass system must be $2.0 < p^*_{K_S} < 3.2$ GeV/c.

- Calculate the expected momentum of K_L from the four vectors of measured γ and K_S. Remove the events where the calculated location of K_L is too close to the extrapolated location of charged tracks from K_S. This cut minimizes the confusion to the K_L detection due to the presence of charged pions in the KLM. For doing so, we define the direction of calculated K_L, $\theta^{cal}_{K_L}$, and the location of extrapolated charged track, θ^{EXT}, by drawing straight lines from the interaction point to the corresponding KLM hits in the first layer. We require $|\theta^{cal}_{K_L} - \theta^{EXT}| < 10°$.

- We look for K_L clusters in the event. If more than one K_L cluster are found, we keep the one closest to $\theta_{K_L}^{cal}$.

- If the detected K_L cluster is inside the 10° cone around the direction of calculated K_L, we declare that a K_L is detected.

From Monte Carlo study, the detection efficiency of $e^+e^- \rightarrow \gamma\phi(K_S K_L)$ event is estimated to be 6.2%.

The triggered efficiency of $e^+e^- \rightarrow \gamma\phi$ event are estimated to be about 60% with the Belle trigger scheme from Monte Carlo study. Most of the untriggered events are discarded by present Belle trigger scheme which suppresses Bhabha events, since most of $e^+e^- \rightarrow \gamma\phi$ events are also triggered with Bhabha event trigger condition which looks simply energy sum of ECL.

The integrated luminosity used for this analysis is 1.2 fb^{-1}. The total number detected as $e^+e^- \rightarrow \gamma\phi(K_S K_L)$ event is 95. Among these events, 25 K_L events are detected along the expected direction.

Figure 6.10 shows the K_L detection efficiency as a function of momentum measured by $e^+e^- \rightarrow \gamma\phi$ with data and Monte Carlo sample. Although statistics is still small, one can see the large discrepancy between the data and Monte Carlo expectation. One of the cause of this discrepancy might be due to the contamination in selected K_S. We need further study for this analysis.

6.4   KLM response in data and Monte Carlo

We studied the probability to make KLM clusters for K_L, pion and kaon, using Monte Carlo samples and data [33].

6.4.1   KLM cluster classification

Table 6.1 shows the average number of KLM clusters per hadronic event in the data and Monte Carlo. The KLM clusters are divided into three categories : those passed the K_L selection criteria, those associated with charged track, and others. Three different Monte Carlo samples, all hadronic events, $B\bar{B}$ enriched sample ($R_2 < 0.2$), and continuum enriched ($0.2 < R_2 < 0.8$), are used in this comparison. Except for those classified as others, which are mostly one-hit clusters and presumably caused by noise hits, number of clusters in the data is lower compared with the Monte Carlo.

Table 6.2 shows a fraction of K_L candidate which are associated with ECL. Here we also observe a discrepancy between the data and Monte Carlo. This might be due to beam-background in the ECL, which is not taken into account in the Monte Carlo in this study.

An average number of K_L per event in the data comes out to be 0.35, whereas Monte Carlo prediction is 0.47. Fraction of detected K_L in the data is 40% by the KLM only, and 60% by a combination of KLM and ECL. Monte Carlo predict these fractions are about 50% and 50%.
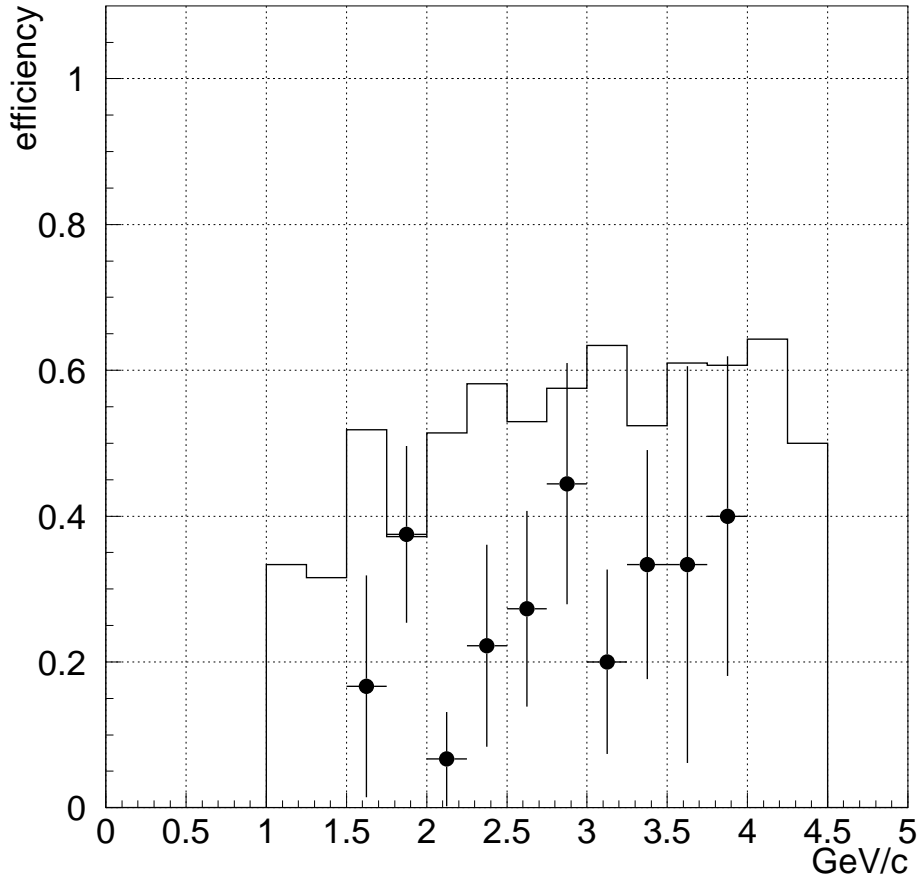
Figure 6.10: K_L detection efficiency as a function of momentum measured by $e^+e^- \rightarrow \gamma\phi$ with data and Monte Carlo sample. Circle shows data, histogram shows Monte Carlo.

	all		$R_2 < 0.2$		$0.2 < R_2 < 0.8$	
	Data	MC	Data	MC	Data	MC
K_L candidate	0.352	0.469	0.305	0.373	0.377	0.516
charged	1.052	1.254	0.835	1.025	1.161	1.371
others	1.577	0.823	1.473	0.705	1.630	0.881
total	2.981	2.545	2.613	2.104	3.168	2.768

Table 6.1: Number of KLM clusters per event and their classification in data and Monte Carlo samples.

	Data	$B\bar{B}$ MC	Continuum MC
reconstructed with KLM only	38%	50%	46%
associated with ECL	62%	50%	54%

Table 6.2: Fractions of K_L clusters which use KLM only and which is associated with ECL.

6.4.2 KLM response to K_L

Figure 6.11 shows the θ distribution of detected K_L in data and Monte Carlo sample. Dip at around 35° and 130° is due to boundary between barrel and endcap. One can see the discrepancy between data and Monte Carlo results. The ratio of data to Monte Carlo is also shown in the right figure. There is about 20-30% of discrepancy between them. The higher values in forward and backward endcap region are due to high beam background in data, which is not taken into account in the Monte Carlo simulation.
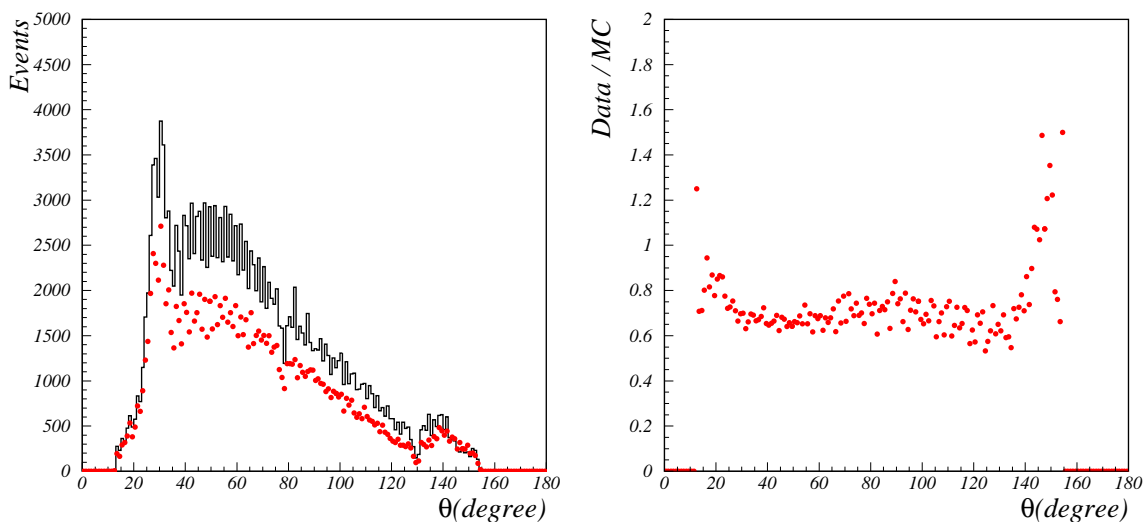
Figure 6.11: θ distribution of detected K_L in data (filled circle) and Monte Carlo sample (histogram) (left), and its ratio (right).

6.4.3   KLM response to $\pi^{\pm}$ and $K^{\pm}$

The pions and kaons are identified by the K/π separation routine. Matching between KLM clusters and pion or kaon tracks are done by the K_L identification method written in section 6.1.

Figure 6.12 shows the θ and ϕ distribution of the fraction to make KLM clusters for pions of momentum between 0.8 and 1.2 GeV/c. Monte Carlo results and real data are shown in the figure. One can see the discrepancy between them, showing that Monte Carlo is always higher than data.

Figure 6.13 shows the fraction of pions making KLM clusters as a function of momentum. Filled circle is for Monte Carlo and open square is for data. The ratio of data to the Monte Carlo are also shown in order to quantify the discrepancy.

The same study was carried out for kaon. Figure 6.14 shows the θ and ϕ distribution of the fraction of making KLM clusters for kaons of momentum between 0.8 and 1.2 GeV/c.

Figure 6.15 shows the fraction of kaons making KLM clusters as a function of momentum. The ratio of data to the Monte Carlo are also shown in order to quantify the discrepancy.

6.4.4   Summary of KLM response to K_L, $\pi^{\pm}$ and $K^{\pm}$

There is about 20-30% discrepancy between data and Monte Carlo in the KLM response to either K_L, pions or kaons. We have noticed that the hadron-shower model which is used in the Monte Carlo might not be representing the real data correctly. The study to modify the hadron-shower model in full detector simulator has been started, so we will get better agreement when the study completes.

(a) θ distribution
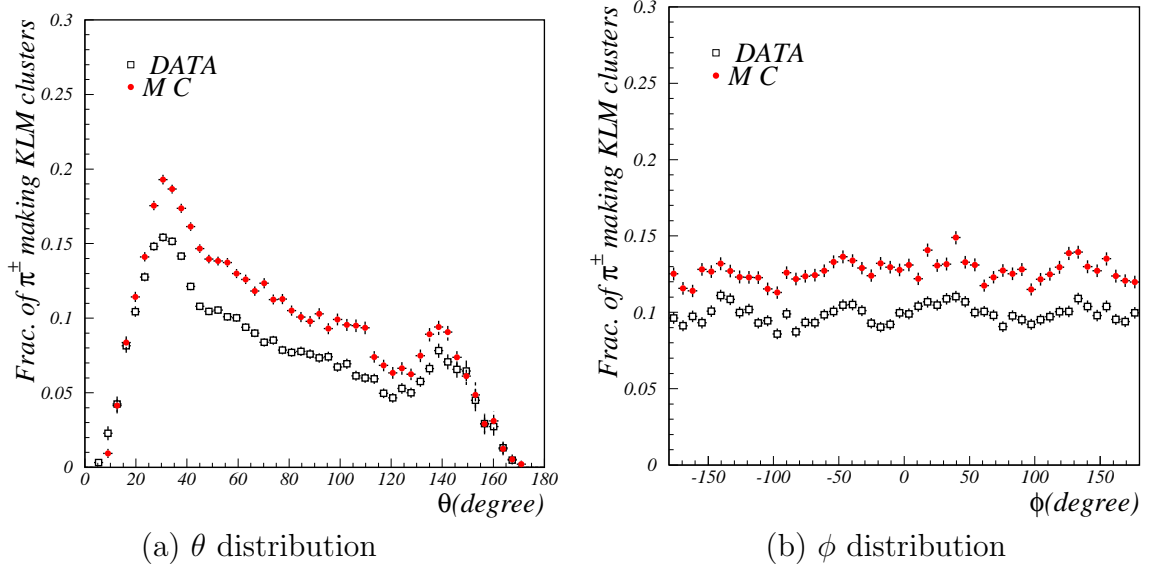
(b) ϕ distribution

Figure 6.12: θ and ϕ distribution of the fraction of making KLM clusters for pions of momentum between 0.8 and 1.2 GeV/c. Monte Carlo results (filled circle) and real data (open box) are shown.
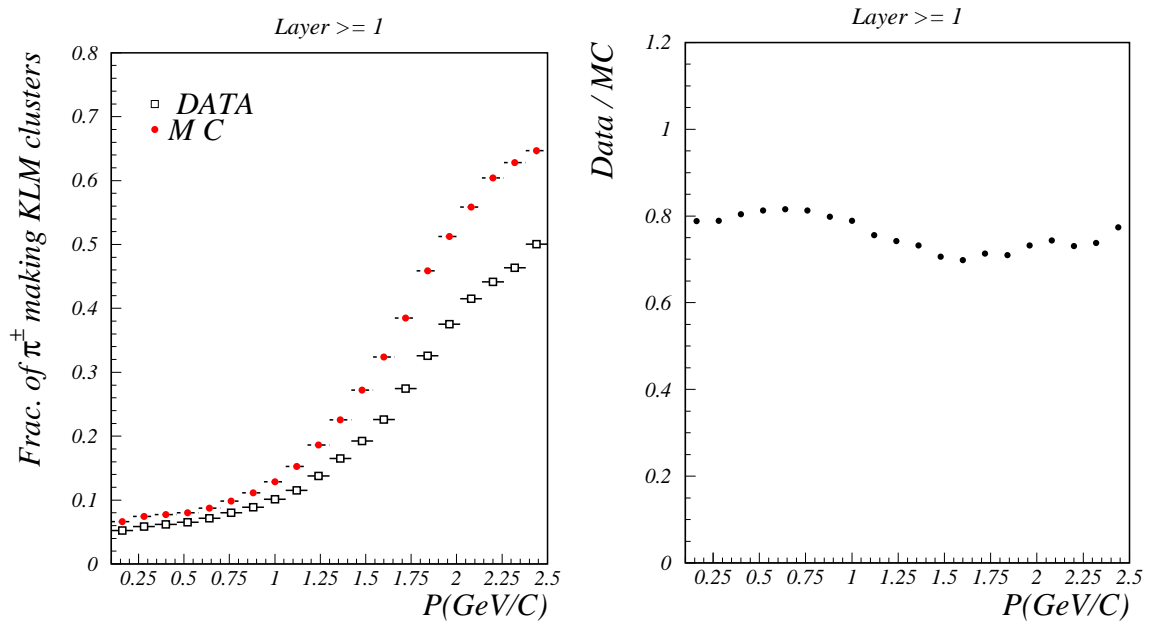
Figure 6.13: The fraction of pions making KLM clusters (left), and the ratio of data to the Monte Carlo (right). In the left plot, filled circle shows Monte Carlo results and open box shows real data.

(a) θ distribution
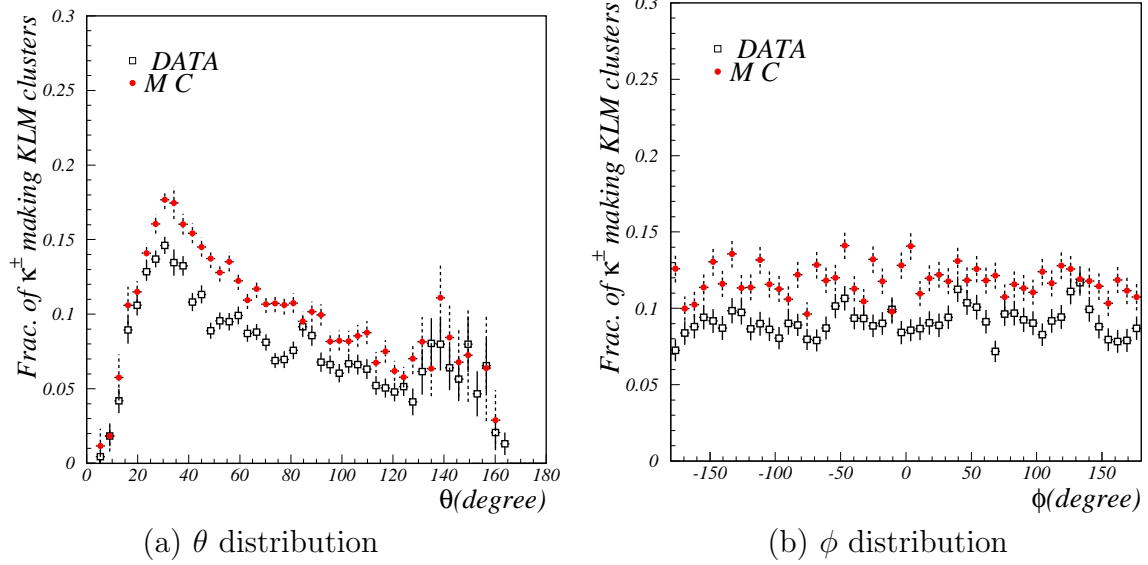
(b) ϕ distribution

Figure 6.14: θ and ϕ distribution of the fraction of making KLM clusters for kaons of momentum between 0.8 and 1.2 GeV/c. Monte Carlo results (filled circle) and real data (open box) are shown.
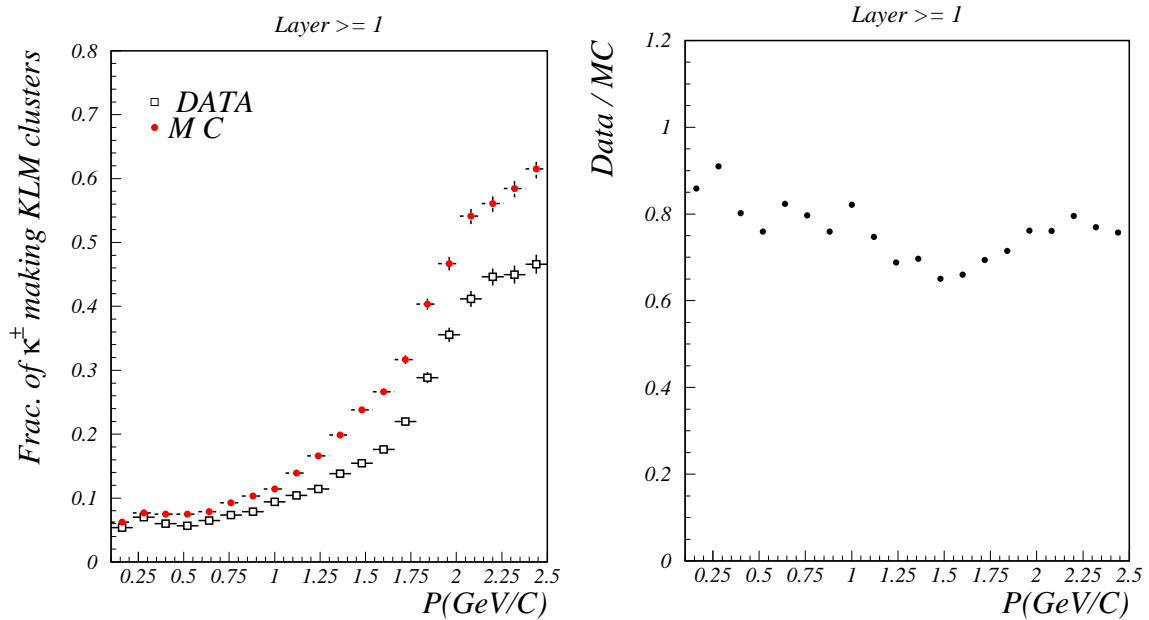
Figure 6.15: The fraction of kaons making KLM clusters (left), and the ratio of data to the Monte Carlo (right). In the left plot, filled circle shows Monte Carlo results and open box shows real data.

60

Chapter 7

Reconstruction of $B^0 \to J/\psi + K_L$ decays

In this chapter we describe the reconstruction procedure of $B^0 \to J/\psi + K_L$ event. Signal yield and background estimation are also described.

7.1 Data set and Monte Carlo events

Data set used in this analysis is 6.2 fb^{-1} that was taken during the run period from June 1999 to July 2000. As Monte Carlo sample, we use 600,000 inclusive J/ψ events. This corresponds to 223 fb^{-1} data of $\Upsilon(4S)$ decays. They are generated as $\Upsilon(4S) \to B\bar{B}$ with the $B^0\bar{B}^0$ mixing being turned off. We allow $\bar{B}^0$ to decay only to $J/\psi X$ and B^0 to decay generically. The J/ψ is allowed to decay into e^+e^- and $\mu^+\mu^-$ each with 50% probability.

For the study of $J/\psi K_L$ signal events and particular background mode such as $J/\psi K^{*0}(K_L \pi^0)$, we use the generator information for those 600,000 inclusive J/ψ events.

7.2 Hadronic event selection

The hadronic events were selected by following criteria.

- At least three "good" tracks were coming from the interaction point, where "good" track was defined by (i) $|r| < 2.0$ cm and $|z| < 4.0$ cm at the closest approach at the beam axis, (ii) momentum projected onto the $xy-$plane > 0.1 GeV/c .

- More than one "good" cluster must be observed in the barrel region of the calorimeter, where "good" cluster was defined in such a way that it was detected in the good acceptance region with an energy deposit greater than 0.1 GeV, where no track were associated with the cluster.

- A sum of all cluster energies, after boosted back to the $\Upsilon(4S)$ rest frame with assumption of massless particle, should be between 10% and 80% of the center-of-mass energy.

- The total visible energy, which was computed as a sum of the "good" tracks assuming pions and the "good" clusters in the $\Upsilon(4S)$ rest frame should exceed 20% of the center-of-mass energy.

- The absolute value of the momentum balance in the z-component calculated in the $\Upsilon(4S)$ rest frame should be less than 50% of center-of-mass energy.

- The event vertex, which was reconstructed from the "good" tracks, must be within 1.5 cm and 3.5 cm from the interaction region in the direction of radial and parallel to the beam axis, respectively.

From Monte Carlo simulations, this selection criteria allows us to retain 92.5% of $B\bar{B}$ events. For J/ψ inclusive and $J/\psi K_L$ events, the efficiency was estimated to be 99.4% and 94.7%, respectively.

In the subsequent analysis, we applied additional event topology cut of $R_2(= H_2/H_0) \leq 0.5$, where H_2 and H_0 are the 2nd and 0th Fox-Wolfram moments [34]. The $J/\psi K_L$ efficiency after this cut was estimated to be 93.4%.

7.3 J/ψ selection

The reconstruction of J/ψ is performed using e^+e^- and $\mu^+\mu^-$ decay modes.

For $J/\psi \to \mu^+\mu^-$ candidates we use two oppositely charged tracks where both tracks are positively identified as muon. For $J/\psi \to e^+e^-$ candidates we use two oppositely charged tracks where both tracks are well identified as electron. In order to save radiative e^+e^- events, we include photons within 50 mrad of the $e^\pm$ direction for the J/ψ reconstruction. Limiting the search cone for the photons to this region effectively remove the part of ECL showers which are associated with the $e^\pm$. We further require that at least one of the lepton has one or more SVD hit in $r\phi$ strip and two SVD hits in z strip.

We perform a J/ψ mass constrained fit to determine the J/ψ vertex and momentum. When photon are included in the fit, the input vertex error of photon is set to 10 cm so that the photon vertex, which is set at interaction point, would not influence.

We required the invariant mass to be in the range $3.05 < M(\ell^+\ell^-) < 3.13$ GeV/c^2 to identify it as J/ψ candidate. This is rather tighter requirement compared with other analyses for exclusive decay modes which contain J/ψ. This is because, due to a limited precision in the K_L measurement, the purity of finally extracted $B^0 \to J/\psi + K_L$ event sample heavily depends on the precision and amount of background in the J/ψ sample.

Figure 7.1 shows the resulting mass distributions for $e^+(\gamma)e^-(\gamma)$ and $\mu^+\mu^-$ separately.
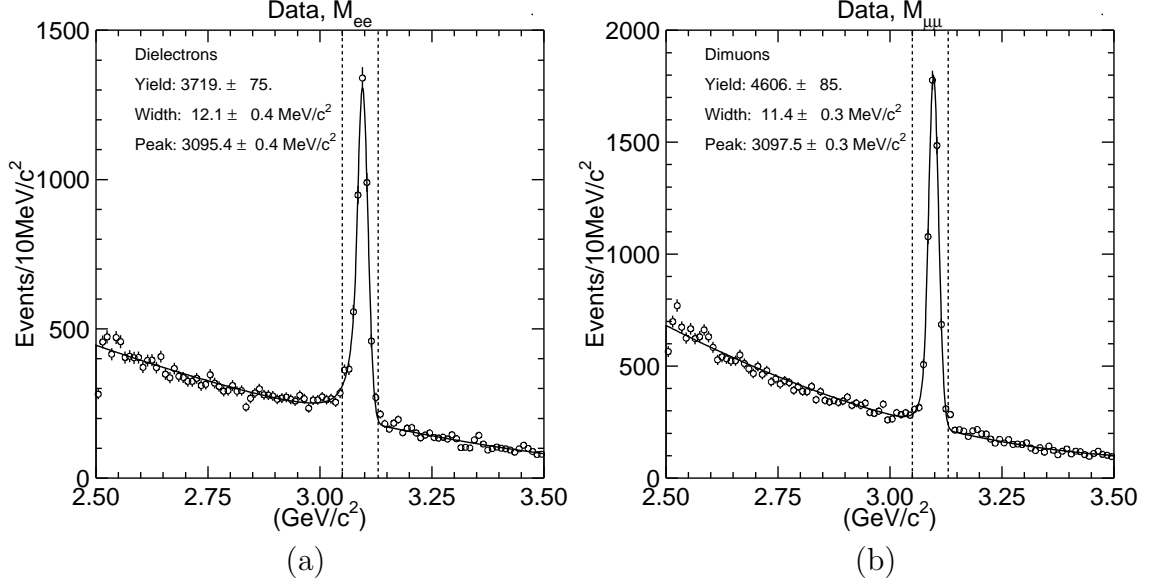
Figure 7.1: Dilepton mass distribution for (a) e^+e^- and (b) $\mu^+\mu^-$ channels.

Figure 7.2 shows the momentum spectrum of J/ψ candidates in the $\Upsilon(4S)$ rest frame. The J/ψ from $B^0 \to J/\psi + K_L$ signal events should lie in the region between 1.42 and 2.0 GeV/c . Those in lower momentum region are mainly the feed down from $B \to \psi'X$ and $B \to \chi_c X$. A broadly distributed background is due to non-J/ψ background.

The detection efficiency of $J/\psi \to e^+e^-(\mu^+\mu^-)$ is estimated to be $50.0 \pm 0.2\%$ ($62.8 \pm 0.2\%$) using Monte Carlo.

7.4 $B^0 \to J/\psi + K_L$ reconstruction

We use all the K_L candidates selected by criteria written in section 6.1. Since we cannot know the momentum of K_L with Belle detector, the reconstrution of $B^0 \to J/\psi + K_L$ beomes a partial reconstruction. Thus we have to obtaion the K_L momentum in the reconstruction.

We impose the following criteria to reconstruct $B^0 \to J/\psi + K_L$ events.

1. For each J/ψ, calculate expected K_L direction in the laboratory frame assuming two body decay of $B^0 \to J/\psi + K_L$ and B^0 holds a half of $\Upsilon(4S)$ energy.

2. Look for K_L inside a cone with 45° opening angle with respect to the expected K_L direction. This cut removes combinatorial background by fake K_L.

3. Make a cone around the K_L with 15° opening angle in the laboratory frame. If any charged track with momentum exceeding a half of calculated K_L momentum is found inside the cone, we discard this K_L. This cut removes background
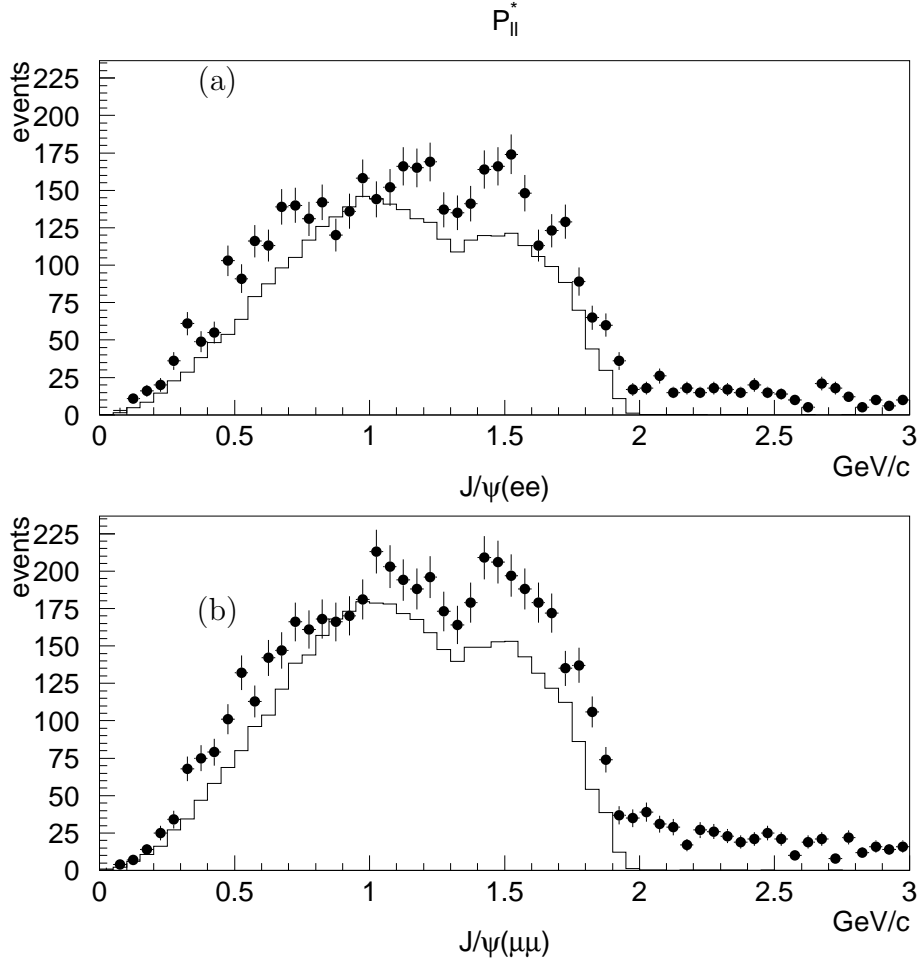
Figure 7.2: Momentum spectrum of J/ψ candidates for (a) e^+e^- and (b) $\mu^+\mu^-$ channels. Solid lines indicate the results from J/ψ inclusive Monte Carlo.

of physics origin such as $B^+ \to J/\psi K^+$ and $B^0 \to J/\psi K_S$, where fake K_L tends to be generated along the direction of high momentum K^+ and K_S.

4. For each combination of J/ψ and K_L, calculate the K_L momentum again assuming two body decay kinematics. Nominal M_{B^0} and $M_{J/\psi}$ are used, but B^0 is not assumed to be at rest this time. The calculation of K_L momentum will be explained in the next paragraph.

5. Calculate the B^0 momentum in the $\Upsilon(4S)$ rest frame, p_B^*. Signal events should center around $p_B^* = 340$ MeV/c, corresponding to the initial motion of B^0 in the $\Upsilon(4S)$ rest frame.

6. $B^0 \to J/\psi + K_L$ candidates must satisfy :

   $1.42 \le p_{J/\psi}^* \le 2.0$ GeV/c, and

   $200 \le p_B^* \le 450$ MeV/c.

64

The K_L momentum is obtained by following calculation. We know the direction of the K_L momentum from the information of the ECL and the KLM by assuming that the K_L was generated at interaction point. The only unknown is the magnitude of K_L momentum, $|\vec{p}_{K_L}|$, when we assume two body decay kinematics. We can obtain it by solving the following equation.

$$
\begin{aligned}
m_B^2 &= (E_{JP} + E_{K_L})^2 - \left(\vec{p}_{J/\psi} + \vec{p}_{K_L}\right)^2 \\
&= \left(E_{JP} + \sqrt{|\vec{p}_{K_L}|^2 + m_{K_L}^2}\right)^2 \\
&\quad - \left(|\vec{p}_{J/\psi}|^2 + |\vec{p}_{K_L}|^2 + 2|\vec{p}_{J/\psi}||\vec{p}_{K_L}|\cos\theta\right)^2
\end{aligned}
\tag{7.1}
$$

where

$$
\begin{aligned}
m_B,\ m_{J/\psi},\ m_{K_L} &\ :\ \text{invariant mass of } B^0,\ J/\psi,\ K_L, \\
E_{J/\psi},\ \vec{p}_{J/\psi} &\ :\ \text{measured energy and momentum of } J/\psi, \\
\vec{p}_{K_L} &\ :\ \text{momentum of } K_L \text{ to be solved}, \\
\theta &\ :\ \text{opening angle between } \vec{p}_{J/\psi} \text{ and } \vec{p}_{K_L}.
\end{aligned}
$$

All the parameters are the value in the laboratory frame. This is the second order equation for $|\vec{p}_{K_L}|$. The solution is expressed as

$$
p_{KL} = \frac{a \cdot b + E_{J/\psi}\sqrt{a^2 - 4m_{K_L}^2(E_{J/\psi}^2 - b^2)}}{2(E_{J/\psi}^2 - b^2)}.
\tag{7.2}
$$

$$
\begin{aligned}
a &\equiv m_B^2 - m_{J/\psi}^2 - m_{K_L}^2, \\
b &\equiv |\vec{p}_{J/\psi}|\cos\theta.
\end{aligned}
$$

The problem of this method is that this is not a fit but only a calculation, so we cannot evaluate the error of $|\vec{p}_{K_L}|$.

Figure 7.3 shows the spectrum of calculated K_L momentum in the $\Upsilon(4S)$ rest frame. The K_L from $B^0 \to J/\psi + K_L$ signal events should lie between 1.55 and 1.85 GeV/c as shown with broken line in the figure. Those from $B \to J/\psi K_L \pi$ background should lie between 1.6 and 1.9 GeV/c. A long tail toward higher momentum region is due to low momentum J/ψ which come from the feed down.

Figure 7.4 shows scatter plots of $p_{J/\psi}^*$ versus p_B^* for data and different sources in Monte Carlo. According to the Monte Carlo, about 88% of the signal events is contained in the region of $200 \le p_B^* \le 450$ MeV/c . The background from $B \to J/\psi K_L \pi$ also peaks near the signal region although the mean is shifted by about 80 MeV/c toward higher p_B^* and the width is much broader. Here the $J/\psi K_L \pi$ background is a sum of both resonant case ($J/\psi K^*$) and non-resonant case, and contributions from $B^\pm \to J/\psi K_L \pi^\pm$ and $B^0 \to J/\psi K_L \pi^0$ are summed. According to the Monte Carlo, about a half of these events remains in the signal p_B^* region. For neither of the two cases, hardly any events populate outside of the $1.42 \le p_{J/\psi}^* \le 2.0$ GeV/c region.
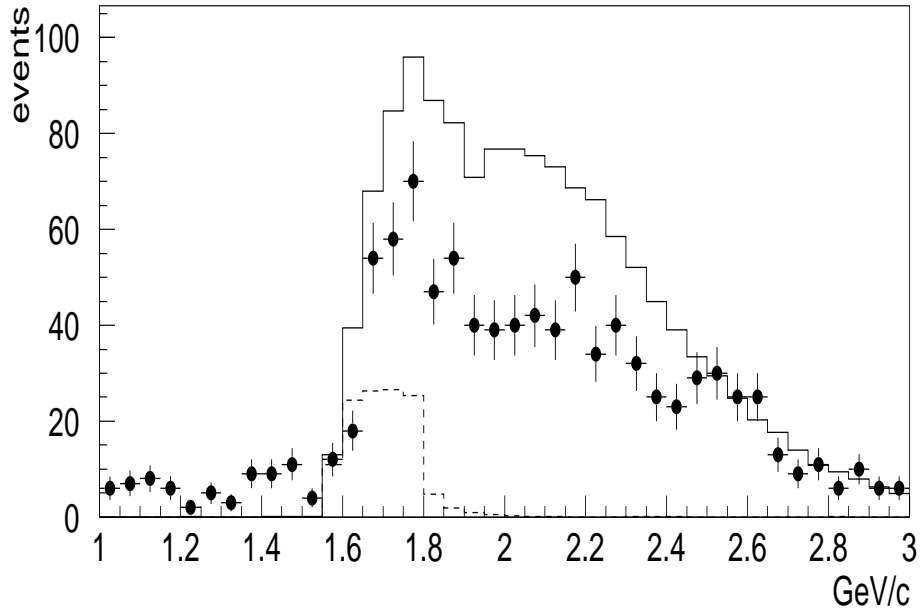
Figure 7.3: Calculated K_L momentum assuming $B^0 \to J/\psi + K_L$ two body decay. Solid line indicates the result from J/ψ inclusive Monte Carlo sample. Broken line is for signal events among them.

Background from sources other than $J/\psi K_L \pi$ are heavily populated in the low $p^*_{J/\psi}$ region. However, those in the signal region mostly stay within the $1.42 \leq p^*_{J/\psi} \leq 2.0$ GeV/c region.

Figure 7.5 shows the p^*_B distribution of the data after the $p^*_{J/\psi}$ cut. Although the $p^*_{J/\psi}$ cut does not remove the background in the signal p^*_B region, we apply this cut in our final distribution because reducing the background in the higher p^*_B region tends to reduce an uncertainty in estimating the amount of background in the signal region. A clear peak in the expected signal region is present.

Figure 7.6 shows the typical example of $B^0 \to J/\psi + K_L$ event display projected on X-Y plane.
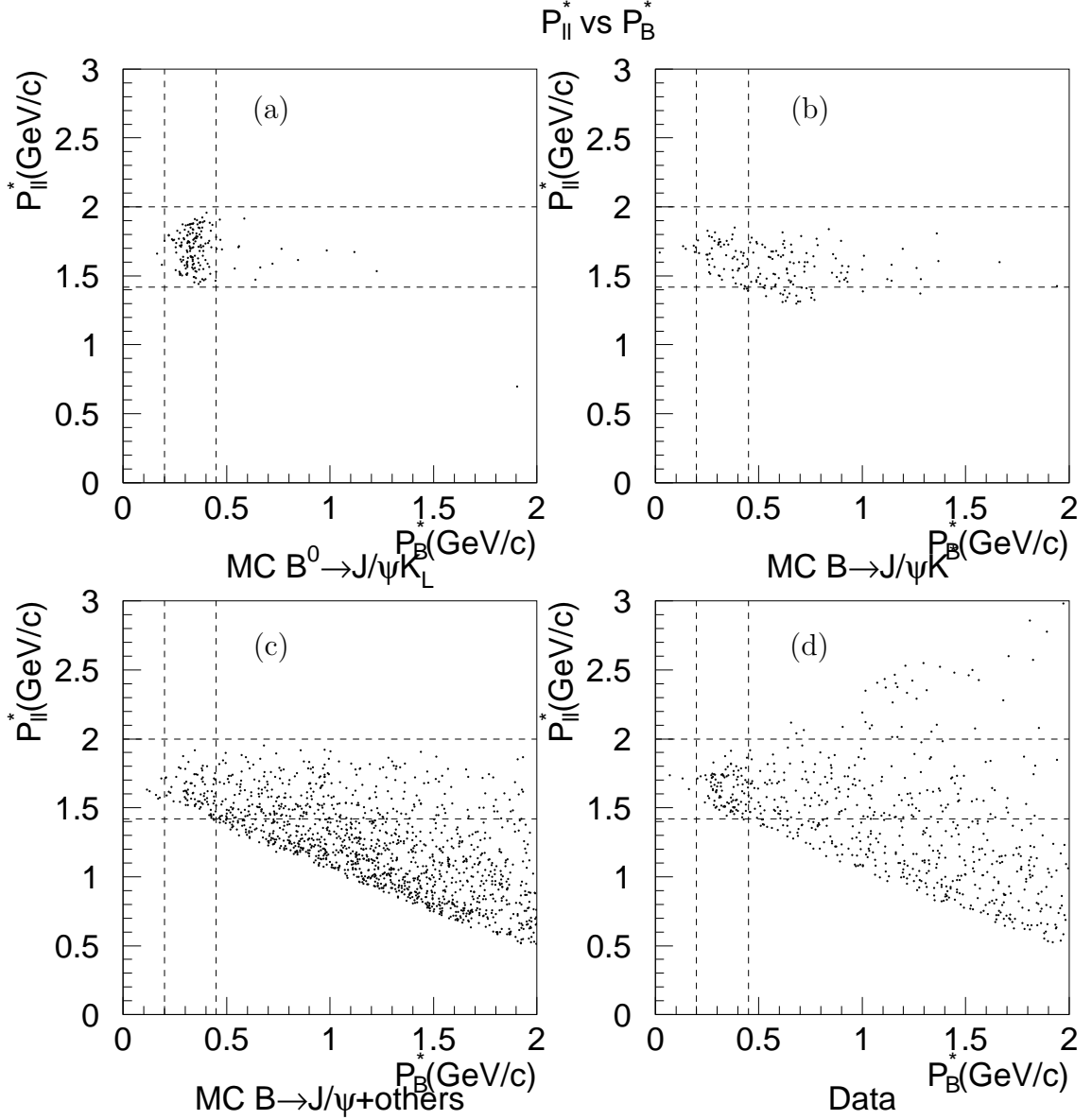
Figure 7.4: Scatter plots of $p^*_{J/\psi}$ versus p^*_B for (a) Monte Carlo signal events, (b) Monte Carlo background events from $B \to J/\psi K_L \pi$, (c) Monte Carlo background events from all other sources combined, and (d) data. The Monte Carlo sample corresponds to $10 fb^{-1}$.
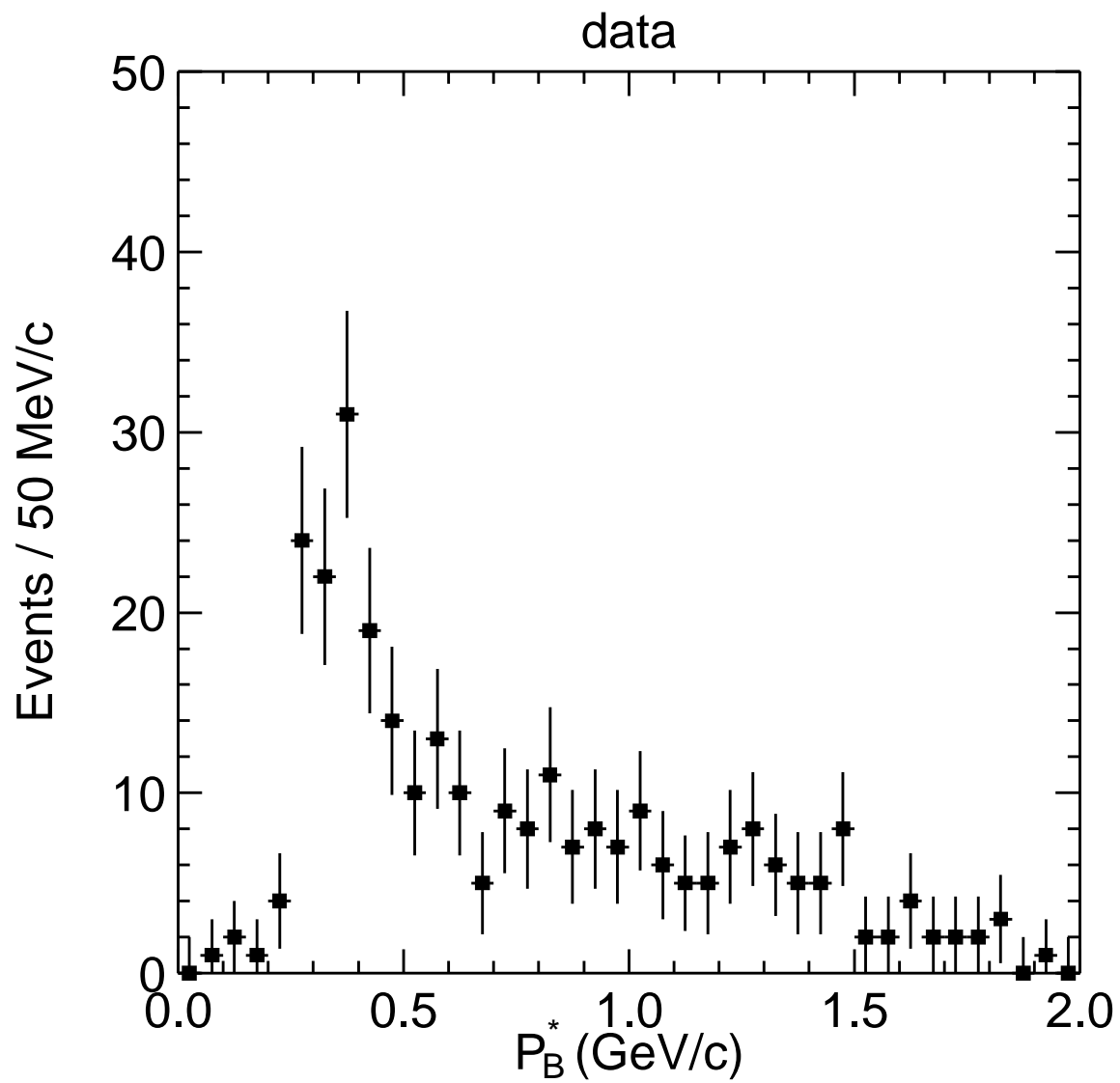
Figure 7.5: p_B^* distribution of the data after $p_{J/\psi}^*$ cut.
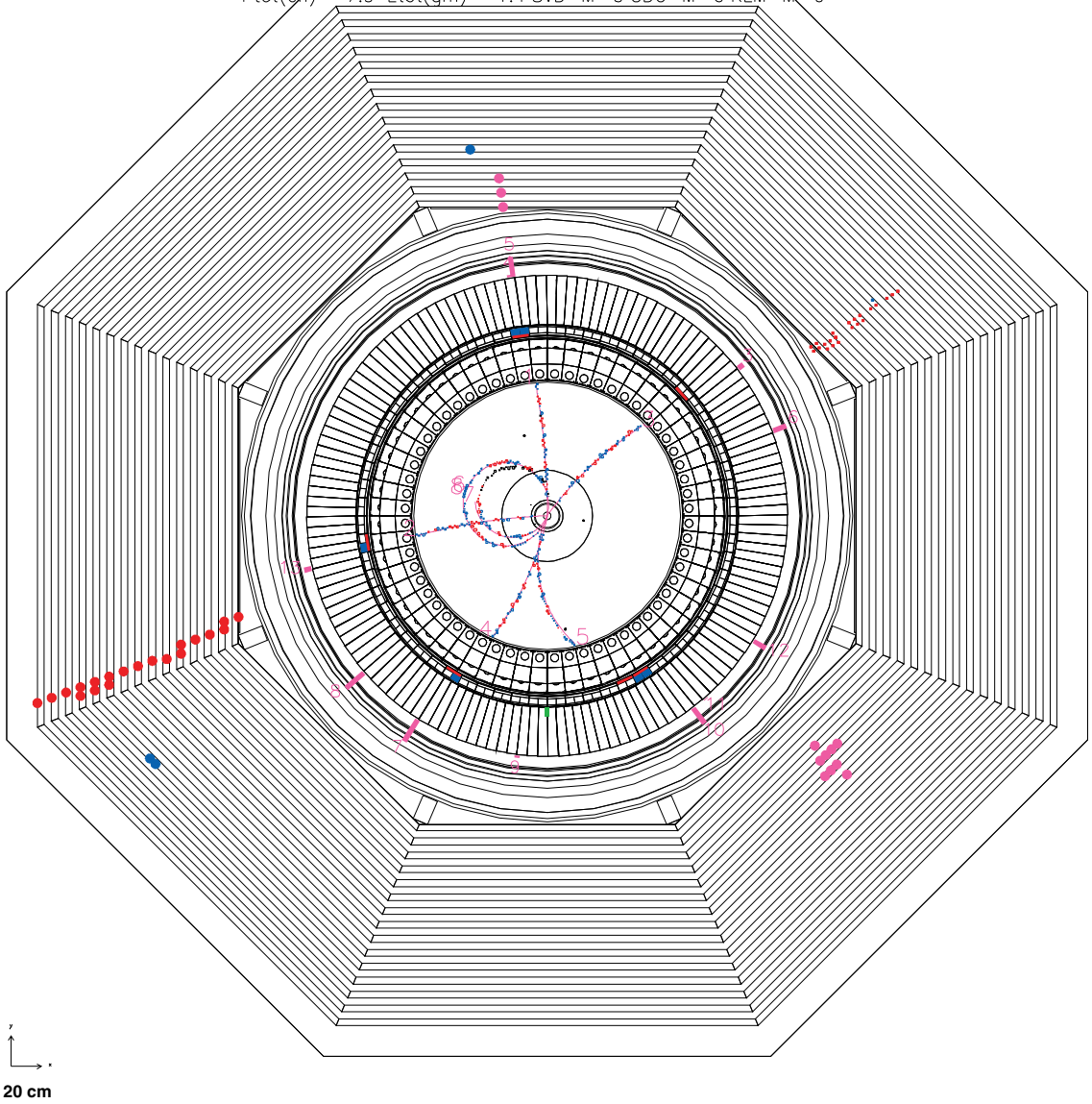
Figure 7.6: A typical example of $J/\psi K_L$ candidate event projected on $X - Y$ plane.

7.5 Signal yield and background estimation

We extract the $J/\psi K_L$ signal yield by fitting the p_B^* distribution to a superposition of the estimated signal and background distributions. For doing this, we rely on an assumption that only those events containing J/ψ become the signal candidates and, therefore, the distributions are reliably estimated using high statistics sample of the J/ψ inclusive Monte Carlo.

Figure 7.7 shows the p_B^* distribution that is obtained by rotating all the K_L candidates in an event by 180° in ϕ before reconstruction. Results from the data and the J/ψ inclusive Monte Carlo are shown. The number of remaining events gives an estimation for the combinatorial background between a J/ψ candidate (including non-J/ψ background) and a fake K_L or between a real J/ψ from one B and a real K_L from other B. The plot shows that the background of this type is negligibly small, and the Monte Carlo can account the measured level in the data although statistical accuracy is still poor.

Both the signal and the $J/\psi K_L \pi$ background shapes are parameterized in terms of reversed Crystal Ball functions which give tails toward higher side instead of normal case where the tails are toward low side. The $J/\psi K_L \pi$ background includes both resonant case $K^* \to K_L \pi$ and non-resonant case $K_L \pi$. The background of all other sources combined is parameterized by a 4th order polynominal. Figure 7.8 show the shapes of p_B^* distributions for the three categories and the result of fitting.

After the shapes of the three distributions are determined separately, we add the two background categories and only its magnitude becomes the free parameter in the fit. For the signal, the magnitude, width and mean of the reversed Crystal Ball function are the free parameters.

Figure 7.9 shows the p_B^* distribution with the result of fitting. The background contributions coming from $B^0 \to J/\psi K_L \pi^0$ is shown separately because it might have its own CP asymmetry. The fraction of its contribution is given by analyzing the Monte Carlo sample.

Table 7.1 summarizes the result of fit. The χ^2 of fit is 21.2 for $ndf = 36$. For comparison, a Monte Carlo result is also given.

	Fit Parameter	Monte Carlo	Data
$J/\psi K_L$	Yield	70.7±3.3	47.5±11.5
	Mean (MeV/c)	335±3	350±15
	Sigma (MeV/c)	54±3	55±10
Background	Total	58.3	47.6
	$J/\psi K^{*0}(K_L \pi^0)$	9.9	8.1
	all others	48.4	39.5
Total yield		129.0	95.1

Table 7.1: Result of fit to the p_B^* distribution. Yields are for the signal p_B^* region.
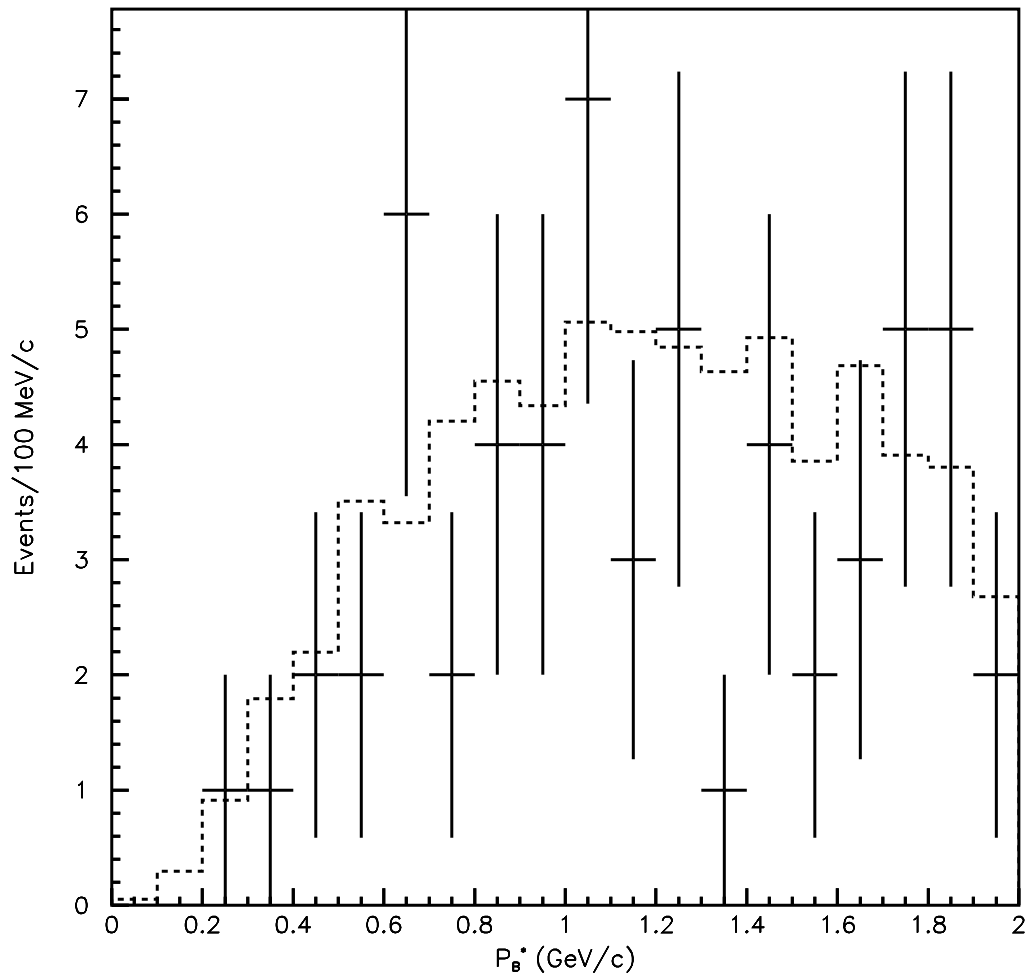
Figure 7.7: p_B^* distribution when all K_L in an event are rotated by 180° in ϕ before reconstruction. Solid and dotted histograms are for the data and the Monte Carlo.

71

Figure 7.8: p_B^* distribution of Monte Carlo and fitted curves for (a) signal events, (b) $B \to J/\psi K_L \pi$ (resonance(K^*) and non-resonance combined), and (c) all other sources combined.
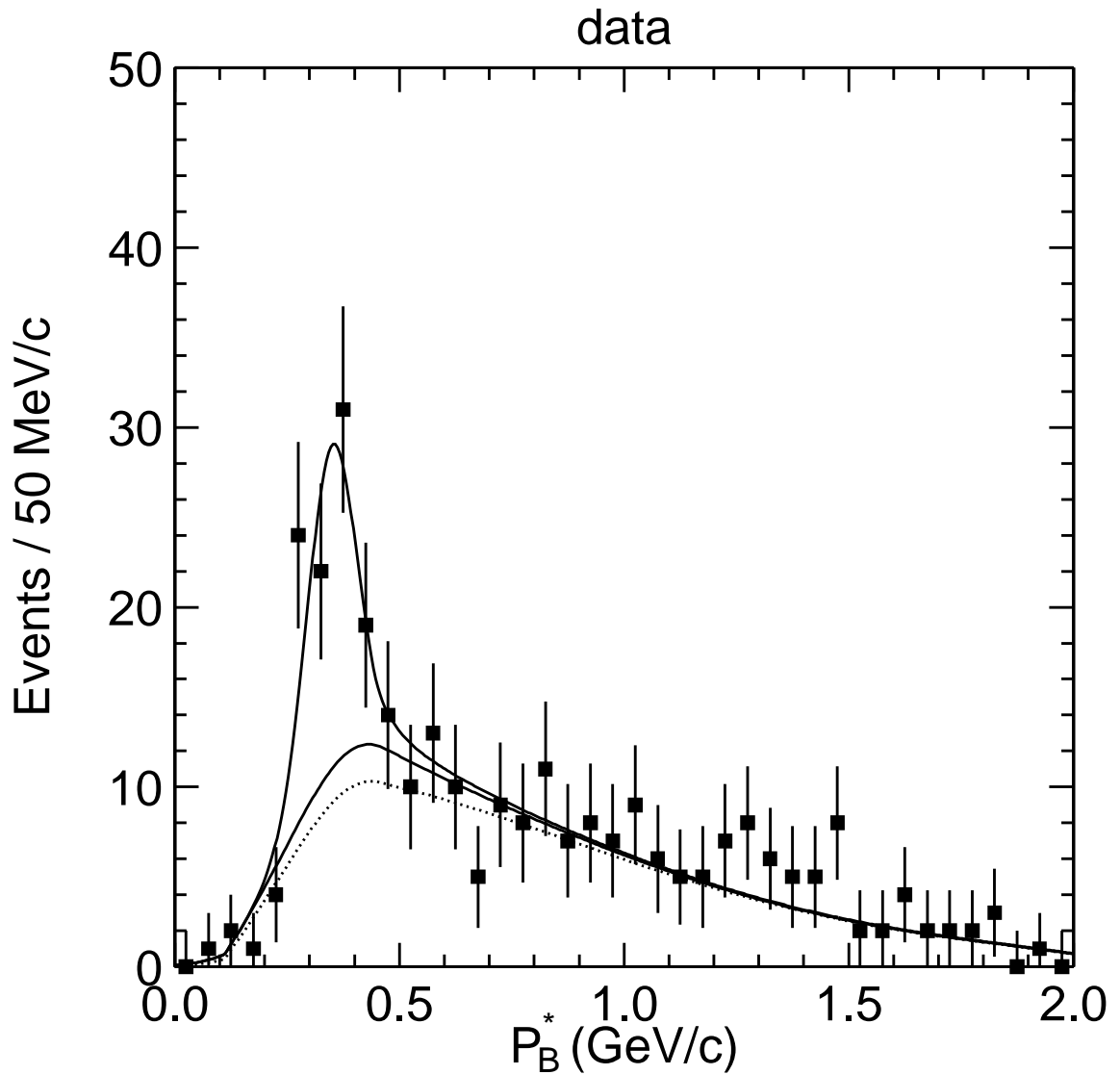
Figure 7.9: p_B^* distribution with the fit result. Upper solid line is a sum of the signal and background. Total background (lower solid line) is divided into those coming from $J/\psi K^{*0}(K_L\pi^0)$ (above the dotted line) and those coming from other sources (below the dotted line).

Chapter 8

Measurement of CP asymmetry

In this chapter we extract the CP asymmetry parameter, $\sin 2\phi_1$, from the event candidates selected in the previous chapter. Flavor tagging, proper decay time difference, vertex reconstruction, resolution function are described.

8.1 Flavor Tagging

Once the $J/\psi K_L$ candidate is found, we must tag the flavor of the other B using the remaining tracks in the event.

Our tagging methods are based on the correlation between the flavor of B mesons and the charge of primary lepton in semileptonic B^0 decay, the sign of total charge of kaons which signatures a cascade decay, or the charge of π from $B \to D^*(\pi D)\ell\nu$ decays. Here we define charged and neutral tracks used in reconstruction of CP decay mode as "CP-side" tracks, and the rest of tracks as "tag-side" tracks. A $B^0(\bar{B}^0)$ flavor for "tag-side" B indicates that "CP-side" was $\bar{B}^0(B^0)$ state at $\Delta t = 0$. We assign the flavor of tag-side B (B_{tag}) in the following criteria.

1. Find a high momentum lepton ($p^*_{lepton} > 1.1$ GeV/c for either electrons or muons) which comes from the semileptonic decay of B_{tag}. We use the relations $B_{tag} = B^0$ for ℓ^+ and $B_{tag} = \bar{B}^0$ for ℓ^-. Electron is examined first. If the flavor is not determined by electron, then muon is examined. If two or more high momentum lepton are found, no flavor is assigned.

2. If the lepton method fails, find charged kaons and count their total charge (Q_K) by simply adding all charges. The relations $B_{tag} = B^0$ for $Q_K > 0$ and $B_{tag} = \bar{B}^0$ for $Q_K < 0$ are used.

3. If high-momentum lepton method and kaon method failed, find medium momentum lepton ($0.6 < p^*_{lepton} < 1.1$ GeV/c). We use the missing momentum (p^*_{miss}) as an approximation of the ν momentum. If $p^*_{lepton} + p^*_{miss} \geq 2.0$ GeV/c, we assume that the lepton comes from $b \to c\nu\ell$ decay and use the relations $B_{tag} = B^0$ for ℓ^+ and $B_{tag} = \bar{B}^0$ for ℓ^-.
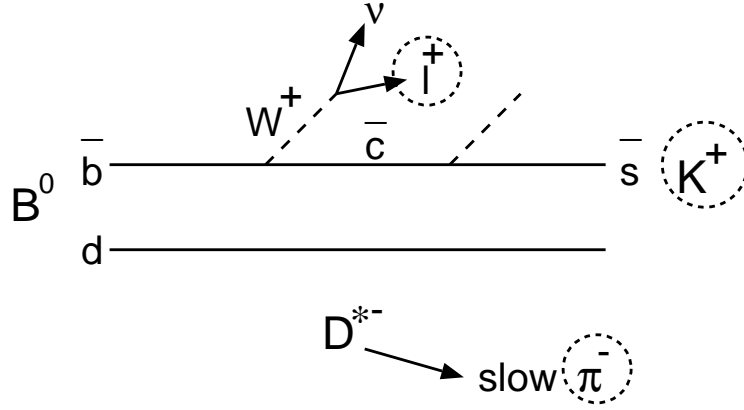
Figure 8.1: Illustration for the flavor tagging method.

4. If above method failed, find low momentum ($p^* < 200$ MeV/c) charged track consistent with a π from the $D^* \to D\pi$ decay. We use the relations $B_{tag} = B^0$ for π^- and $B_{tag} = \bar{B}^0$ for π^+.

Figure 8.1 illustrates the schematics of our flavor tagging method.

The efficiency and wrong tag fraction is obtained using exclusively reconstructed $B \to D^{(*)}\ell\nu$ events which are self tagging decay modes, and the full Monte Carlo simulation. Here, we define

- Tagging efficiency: $\epsilon_{tag} = N_{tag}/N_{rec}$, where N_{tag} and N_{rec} are number of tagged and reconstructed CP events, respectively.

- Wrong-tag fraction: $\omega =$(number of wrongly tagged events)/ (total number of tagged events)

Taking into account the wrong-tag fraction, the time evolution of the opposite flavor (OF) and same flavor (SF) neutral B meson pair is given as

$$\mathcal{P}_{OF} \propto 1 + (1 - 2\omega)\cos(\Delta m_d \Delta t), \tag{8.1}$$
$$\mathcal{P}_{SF} \propto 1 + (1 - 2\omega)\cos(\Delta m_d \Delta t). \tag{8.2}$$

The wrong-tag fraction determines the oscillation amplitude of the OF-SF asymmetry.

$$A_{mix} = \frac{OF - SF}{OF + SF} = (1 - 2\omega)\cos(\Delta m_d \Delta t) \tag{8.3}$$

We fit the time evolution of the OF and SF events simultaneously and obtain the wrong-tag fraction [35].

We use the following decay modes:

- $B^0 \to D^{*-}\ell^+\nu, D^{*-} \to \bar{D}^0\pi^-$

  - $\bar{D}^0 \to K^+\pi^-$

$$- \ \bar{D}^0 \rightarrow K^+ \pi^- \pi^0$$

$$- \ \bar{D}^0 \rightarrow K^+ \pi^+ \pi^- \pi^-$$

- $B^0 \rightarrow D^- \ell^+ \nu, D^- \rightarrow K^+ \pi^- \pi^-$

The vertex position of $D^{(*)} \ell \nu$ is obtained in the following way. First, we fit the D vertex using K and π tracks, where K and π mass is constrained to the world average D mass. For the $K\pi\pi^0$ mode, D mass constraint is turned off. Then, we perform a vertex fitting of ℓ and D tracks to obtain the B vertex. The slow pion track from D^* is not used in the fit, since it does not help to improve B vertex resolution.

We apply the flavor tagging mentioned above to the tag-side, treating the tracks used by the reconstruction of $D^{(*)} \ell \nu$ decay as the CP-side tracks. We also use the same method to obtain a tag-side vertex position as this analysis, which is described in detail later.

We obtain the wrong-tag fraction together with the mixing parameter Δm_d by fitting the Δz distribution of the SF and OF events.

The results are

$$\omega_{lepton} = 0.071 \pm 0.045 \ \ \text{and} \ \ \omega_K = 0.199 \pm 0.070. \tag{8.4}$$

The tagging efficiencies are obtained using the same $D^{(*)} \ell \nu$ samples.

$$\epsilon_{lepton} \ = \ 0.142 \pm 0.021, \tag{8.5}$$
$$\epsilon_K \ = \ 0.279 \pm 0.042. \tag{8.6}$$

We have also checked the wrong-tag fraction using the time-integrated number of OF and SF events with $D^{(*)\mp} \ell^\pm \nu$ sample. Taking into account the B_d^0-$\bar{B}_d^0$ mixing effect, ω is obtained by

$$\omega = \frac{\chi_{obs} - \chi_d}{1 - 2\chi_d}, \quad \chi_d = \frac{\tau_{B^0}^2 \Delta m^2}{2(1 + \tau_{B^0}^2 \Delta m^2)} \tag{8.7}$$

where $\chi_{obs} = N_{SF}/(N_{OF} + N_{SF})$, and we use $\chi_d = 0.172 \pm 0.010$ [13]. Both results are consistent within errors.

The tagging efficiencies and wrong tag fractions of mid-momentum lepton and slow pion are obtained from Monte Carlo analysis. The efficiencies for mid-momentum lepton and slow pion are 3% and 7%, and wrong tag fractions are 29% and 34%, respectively.

The results are summarized in table 8.1, These give total efficiency of 0.52, and the total effective tagging efficiency (ϵ_{eff}), defined as a sum of $\epsilon(1 - 2\omega)$ over all tagging methods, is 0.218.

We find a total of 42 tagged events, of which 8 events were tagged by a high-momentum e, 7 events by a high-momentum μ, 19 events by $K^\pm$, 0 events by medium-momentum e, 2 events by medium-momentum μ, and 6 events by slow π.

76

Method	ϵ	ω	ϵ_{eff}
High p^* lepton	0.142±0.021	0.071±0.045	0.105±0.027
$K^{\pm}$	0.279±0.042	0.199±0.070	0.101± 4.9
Med. p^* lepton	0.029±0.015	0.29±0.15	0.005
Slow π	0.070±0.035	0.34±0.15	0.007
Total	0.52		0.218

Table 8.1: Summary of the tagging efficiencies (ϵ), wrong tag fractions (ω) and effective tagging efficiencies (ϵ_{eff}).

8.2   Proper decay time difference

The proper decay time difference of each candidate event is given by

$$\Delta t = (z_{CP} - z_{tag})/\beta\gamma c \tag{8.8}$$

where z_{CP} and z_{tag} are z vertices for CP-side and tag-side B, respectively, and $\beta\gamma = 0.425$ is the Lorentz boost factor at KEKB.

8.3   Vertex reconstruction

8.3.1 CP-side vertex

We use the J/ψ vertex as the vertex for the B_{CP}. The vertex of J/ψ is reconstructed using two daughter leptons with the constraint that they come from the interaction point profile (IP profile) smeared with finite B flight length in the r-ϕ plane. We use leptons only if there are sufficient numbers of SVD hits associated by the Kalman filtering technique; i.e. with r-ϕ hits in at least one layer and with two or more z hits in total.

The IP profile is calculated offline for every accelerator fill using hadronic events. First, IP is calculated event by event using hadronic data. Then, event-by-event IP distribution is fitted with the 3-dimensional Gaussian. Finally, IP profile is determined from the fit results and the information from KEKB accelerator group. The size of IP profile in x is calculated from the fit, taking into account the primary vertex resolution. The primary vertex resolution is obtained from the primary vertex position distribution in y, since the beam size in y is less than 10 μm and the σ of the y is a good representation of the vertex resolution. The size of IP profile in y is determined from the beam size of HER and LER measured by accelerator group. The typical size of the IP profile is 100 μm in x, 5 μm in y and 3000 μm in z. Uncertainty of ~ 20 μm is added in quadrature to the size of IP profile to account for the uncertainty of the B decay position due to the transverse motion of the B meson. Figure 8.2 illustrates the vertex reconstruction of two B decay vertices.

The efficiency of the vertex reconstruction is estimated to be 96% with $B^{\pm} \to J/\psi K^{\pm}$ and $B^0(\bar{B}^0) \to J/\psi K^{*0}(K^{\pm}\pi^{\mp})$ events. This is consistent with the expectation from SVD acceptance and cluster matching efficiency. The z vertex resolution
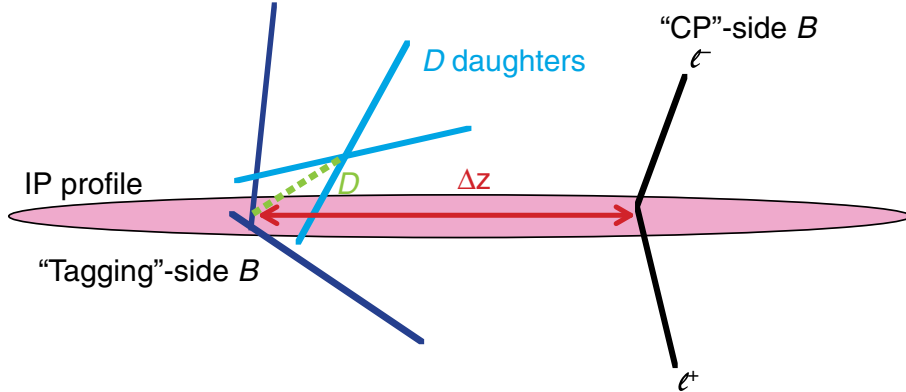
Figure 8.2: Illustration for vertex reconstruction of two B decay vertices.

of CP-side B estimated with the Monte Carlo study is typically 40 μm, which is small enough to meet the requirement of the Δz resolution of ~ 100 μm.

8.3.2 Tag-side vertex

The algorithm for tag-side vertex reconstruction was carefully chosen to minimize the effect of long-lived particles, secondary vertices from charmed hadrons and a small fraction of poorly-reconstructed tracks. Among charged tracks remaining after the B_{CP} reconstruction, we use tracks with SVD hits (the same condition as that for CP side). If the track has a large tracking error in z direction ($\sigma_z > 0.5$ mm), it is not used for the fit to eliminate badly reconstructed tracks. Tracks are removed if they form a K_S candidate satisfying the K_S selection criteria and $|M_{K_S} - M_{\pi^+\pi^-}| < 15$ MeV/c^2. Tracks are also removed if the impact parameter from the IP center greater than 0.5 mm in $r - \phi$ plane (δr), or greater than 1.8 mm from the B_{CP} vertex in z (δz). Figure 8.3 shows the distribution of these track parameters in the data [36].

The remaining tracks and the IP constraint are used to reconstruct the tag-side vertex. If the reduced χ^2 ($\chi^2/n = \chi^2/$number of degrees of freedom) of vertex with IP constraint is worse than 20, we remove the tracks that gives the largest contribution to the χ^2 of the vertex and do the vertex reconstruction again. This trimming procedure is continued until the reduced χ^2 is below 20. The reconstruction efficiency was measured to be 96% with $B^{\pm} \to J/\psi K^{\pm}$ and $B^0(\bar{B}^0) \to J/\psi K^{*0}(K^{\pm}\pi^{\mp})$ events. The expected z vertex resolution of tag-side B with Monte Carlo study is typically ~ 85 μm.

8.4 Resolution function

8.4.1 Resolution function

The resolution function can be obtained either from the Δt residual distribution ($\Delta t(measured) - \Delta t(generated)$ distribution) for the signal Monte Carlo sample or from a lifetime fit of B meson using the Δt distribution of non-CP decay mode [36].

78
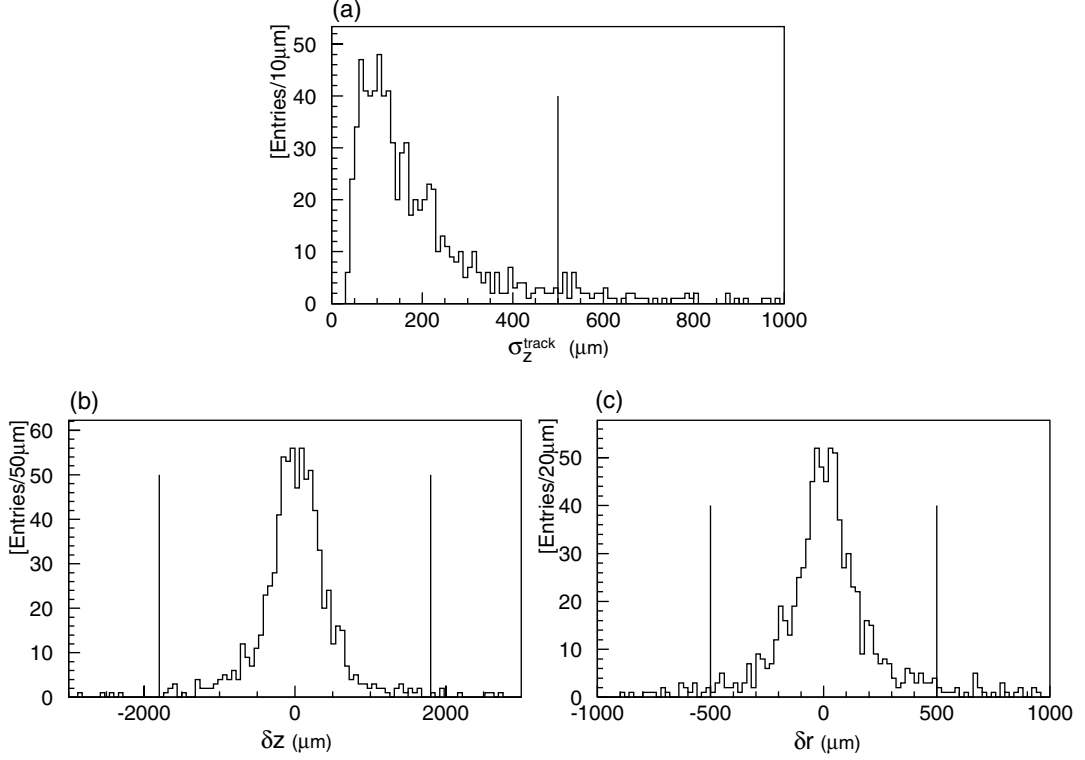
Figure 8.3: (a) σ_z^{track} distribution, (b) δz distribution and (c) δr distribution in the data. Vertical line indicate cut values for each variable.

The resolution of Δt, $R(\Delta t)$, is parametrized as a sum of two Gaussians, where a *main* Gaussian is for the intrinsic SVD resolution and the effect of the secondary charmed mesons in tag-side B decays, and a *tail* Gaussian is for a few poorly reconstructed tracks :

$$ R(\Delta t) = \frac{f_{main}}{\sigma\sqrt{2\pi}} \exp\left(-\frac{(\Delta t - \mu)^2}{2\sigma^2} \right) + \frac{f_{tail}}{\sigma_{tail}\sqrt{2\pi}} \exp\left(-\frac{(\Delta t - \mu_{tail})^2}{2\sigma_{tail}^2} \right). \qquad (8.9) $$

The mean values (μ, μ_{tail}) and width (σ, σ_{tail}) of the two Gaussians are calculated event-by-event from the CP-side and tag-side vertex errors, taking into account the error due to the approximation of $\Delta t \sim \Delta z/\beta\gamma c$. The Gaussian parameters and the fraction f_{tail} $(= 1 - f_{main})$ are determined from the full Monte Carlo simulation studies and a multi-parameter fit to $B \to D^*\ell\nu$ data. Figure 8.4 shows the example of average shape of the $R(\Delta t)$ by summing event-by-event $R(\Delta t)$ functions over 440 $B^- \to D^0\pi^-$ events. In order to parameterize the total shape of the averaged resolution function, we fit it by a triple Gaussian. The following function is obtained by the fit, and we use this function as the resolution function in this analysis.

$$ g(\Delta t - \Delta t') = 0.656 e^{\frac{-(\Delta t - \Delta t' + 0.143)^2}{2 \times 0.754^2}} + 0.298 e^{\frac{-(\Delta t - \Delta t' + 0.260)^2}{2 \times 1.65^2}} + 0.046 e^{\frac{-(\Delta t - \Delta t' + 0.56)^2}{2 \times 0.4.7^2}}. $$
$$ (8.10) $$

79
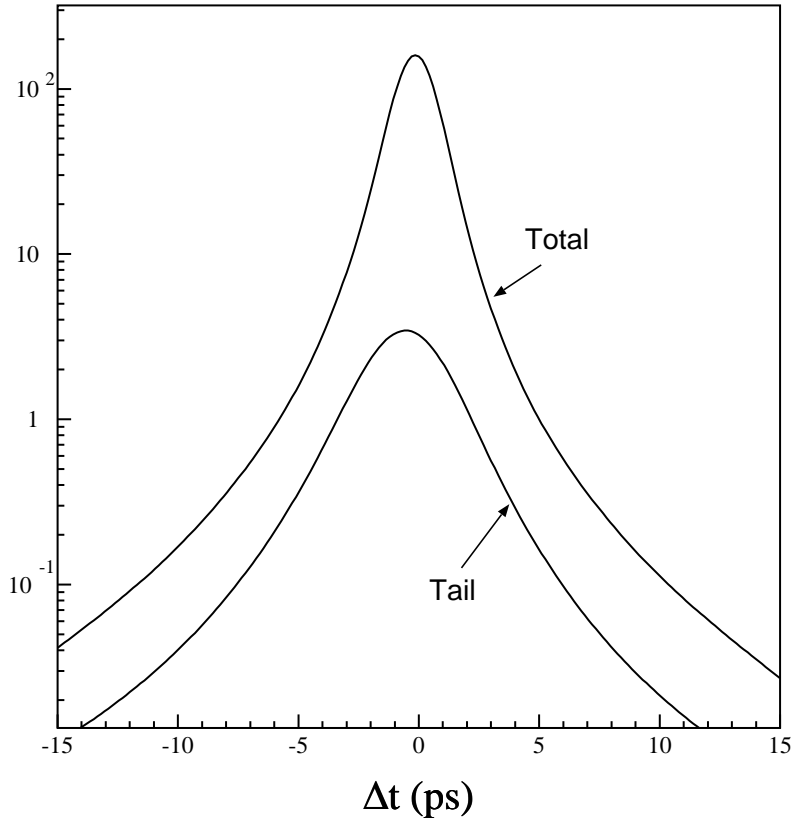
Figure 8.4: The average shape of the event-by-event resolution function obtained by summing over 440 $B^- \to D^0\pi^-$ events.

8.4.2 Resolution function for background events

Table 8.2 summarizes the result of Monte Carlo study for the proper decay length measurements. Difference between the measured and generated z vertices for the CP-side and tag-side are fitted to a single Gaussian. The same analysis is also done to Δz. In reality, these shapes are not necessarily single Gaussians, but resemble superpositions of two or more Gaussians. However we use here single Gaussian in order to see the general behavior in the differences between z_{CP} and z_{tag}, and between different CP-side decay modes.

We notice a shift of the mean for z_{tag} by about $+20$ μm. This is due to a $D^{(*)}$ contribution in the tagging side decay, and causes a shift of Δz by about -20 μm. It should also be noticed that the mean and sigma for the Δz are almost same for different CP-side decay modes. Therefore, we can justify the use of a same resolution function for the signal and background functions.

80

CP-side decay mode	$J/\psi K_L$	$J/\psi K^{*\pm}$	$J/\psi K^{*0}$	$J/\psi X$
z_{CP} mean(μm)	-4 ± 1	14 ± 2	-3 ± 2	5 ± 4
sigma(μm)	46 ± 1	42 ± 2	46 ± 2	48 ± 4
z_{tag} mean(μm)	18 ± 2	20 ± 4	19 ± 4	17 ± 8
sigma(μm)	83 ± 2	83 ± 4	96 ± 5	91 ± 10
Δz mean(μm)	-23 ± 2	-20 ± 5	-31 ± 5	-27 ± 10
sigma(μm)	109 ± 3	102 ± 5	110 ± 5	121 ± 18

Table 8.2: Monte Carlo estimation of measurement accuracy for the CP-side z, tag-side z and Δz.

8.5 CP fitting

For the extraction of the $\sin 2\phi_1$, we perform a fit to minimize the log-likelihood function

$$L = -2 \sum_i \ln \rho_i(\Delta t_i, (p_B^*)_i, \omega_i) \tag{8.11}$$

where i is for each candidate event within $0.2 < p_B^* < 0.45$ GeV/c.

The likelihood function ρ is a convolution of the probability density function F for the signal and background with the resolution function $g(\Delta t - \Delta t')$,

$$
\begin{aligned}
\rho(\Delta t, (p_B^*), \omega) &= c_{sig}(p_B^*) \int g(\Delta t - \Delta t') F_{sig}(\Delta t, \omega) d(\Delta t') \\
&\quad + (1 - c_{sig}(p_B^*)) \int g(\Delta t - \Delta t') F_{bkg}(\Delta t, (p_B^*), \omega) d(\Delta t') \tag{8.12}
\end{aligned}
$$

where c_{sig} is the signal fraction of the candidate events. The signal functions is given by

$$F_{sig}(\Delta t, \omega) = \frac{1}{2\tau_B} e^{-|\Delta t|/\tau_B} \left[1 \pm (1 - 2\omega) \sin 2\phi_1 \sin(\Delta m_d \Delta t) \right], \tag{8.13}$$

where $+$ and $-$ are for $B^0(t=0) \to J/\psi K_L$ and $\bar{B}^0(t=0) \to J/\psi K_L$, respectively. The background function is given as

$$
\begin{aligned}
F_{bkg}(\Delta t, (p_B^*), \omega) &= \frac{1}{2\tau_B} e^{-|\Delta t|/\tau_B} \left[(1 - b_{CP}(p_B^*)) \right. \\
&\quad \left. + b_{CP}(p_B^*) \{ 1 \pm \alpha(1 - 2\omega) \sin 2\phi_1 \sin(\Delta m_d \Delta t) \} \right]. \tag{8.14}
\end{aligned}
$$

Use of $+$ and $-$ are the same as for the signal function case. The value of wrong tagging fraction, ω, must be assigned to each event depending which tagging method is used for the event.

8.5.1 Fraction and CP of the background

The background component is divided into a part that exhibit its own CP asymmetry, given by a fraction b_{CP}, and all others that does not exhibit CP asymmetry. Magnitude and sign of the background asymmetry is parameterized by α.

Since the backgrond is dominated by the events that contain J/ψ and K_L cluster, either generated by real K_L or by other high momentum hadrons such as $K^{\pm}$ and $\pi^{\pm}$ and K_S, we can conlcude that most of the background is due to the B decays. Therefore, we fix that all the background has the B lifetime dependence. The $c_{sig}(p_B^*)$ and b_{CP} are determined from the fit in the p_B^* distribution. Figure 8.5 shows the fraction of the signal, fraction of the background which do not have CP asymmetry, and fraction of the background which have CP asymmetry, in the candidate events as a function of p_B^* .
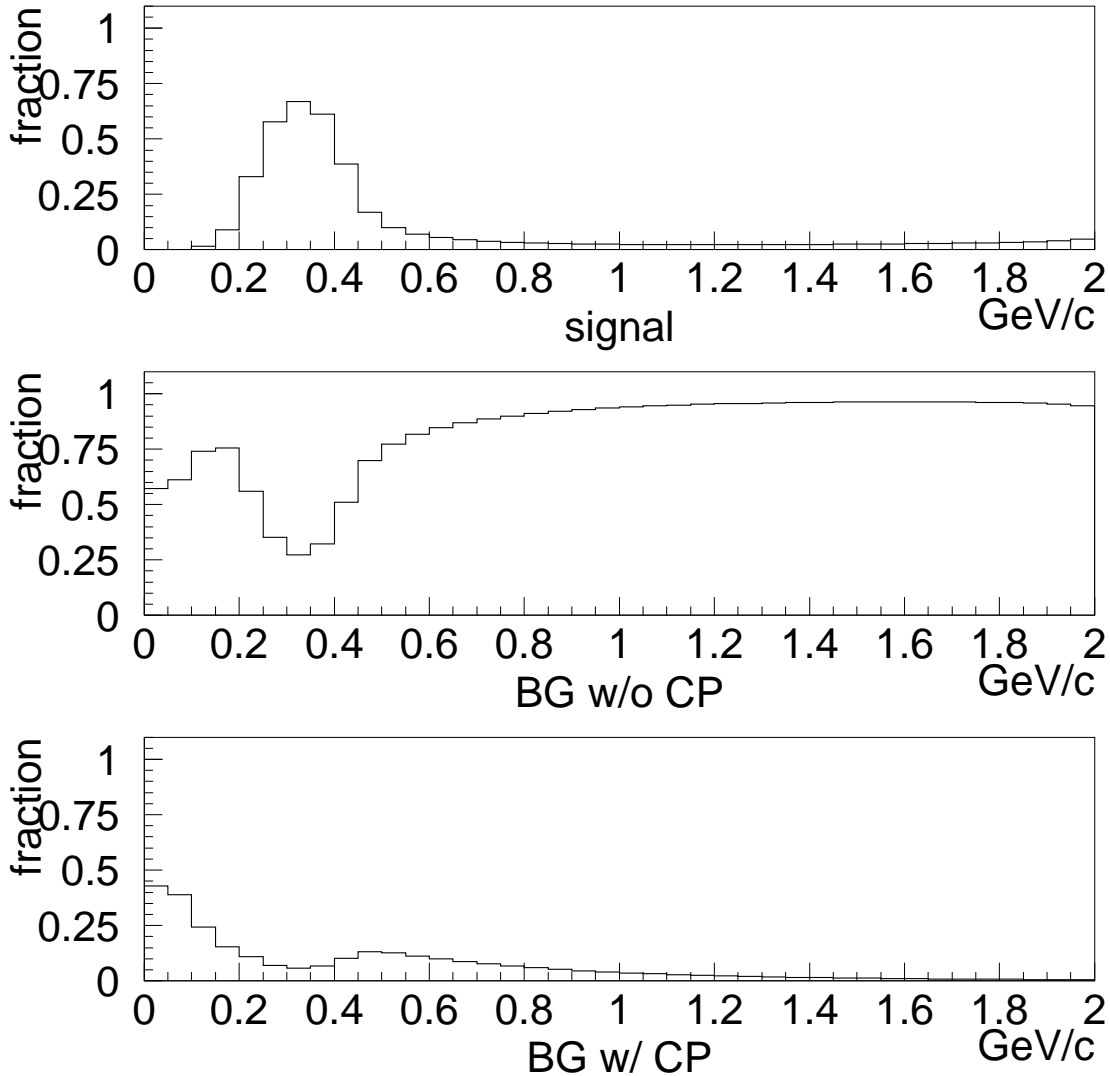

Figure 8.5: The p_B^* dependence of the fraction of signal (c_{sig}), background with CP asymmetry (b_{CP}), and background without CP asymmetry ($1 - c_{sig} - b_{CP}$).

From the 600,000 J/ψ inclusive Monte Carlo events, we find 3,290 events which are generated as $J/\psi K_L$ and pass all the requirements for the $J/\psi K_L$ event selection. We find 2,512 events which are not $J/\psi K_L$ but pass the $J/\psi K_L$ event selection. Listed in table 8.3 are the background sources which are grouped according to CP asymmetry that they exhibit. Major contributions in each group are listed. Among the background which contain CP asymmetry, major contributions come from $\chi_{c1} K_L$, $J/\psi K_S$ and $J/\psi K^*(K_L \pi)$. The CP sign of the first two are opposite from each other and therefore they cancel. On the other hand, the $J/\psi K^{*0}(K_L \pi^0)$ state is in general a mixture of CP even and odd states. The 1997 CLEO measurement concluded that the $L = 1$ component in the $B^0 \rightarrow J/\psi K^{*0}$ amplitude is small, where L is the orbital angular momentum between J/ψ and K^{*0}. If this result holds, the $J/\psi K^{*0}$ state which is observed by $K^{*0} \rightarrow K_L \pi^0$ decay has the opposite CP as $J/\psi K_L$ state, resulting the constant α in table 8.3 being ≈ -1. In this case, about 17% of the background might exhibit the opposite CP asymmetry from the $J/\psi K_L$ signal events.

In this study we decided that we set the parameter of CP asymmetry in the probability density function, α, to be zero for the fit.

CP asymmetry w.r.t. $J/\psi K_L$	decay mode	background	fraction to total background
0	$B^+ \rightarrow J/\psi K^{*+}(K_L \pi^+)$	736	29.3%
	$B^+ \rightarrow J/\psi K^+$	177	7.0%
	$B^+ \rightarrow J/\psi K_L \pi^+$	135	5.4%
	$B^0 \rightarrow J/\psi K_L \pi^0$	114	4.5%
+1	$B^0 \rightarrow \psi' K_L$	20	0.8%
	$B^0 \rightarrow \chi_{c1} K_L$	133	5.3%
-1	$B^0 \rightarrow J/\psi K_S$	157	6.3%
$+\alpha$	$B^0 \rightarrow J/\psi K^{*0}(K_L \pi^0)$	426	17.0%
	$B^0 \rightarrow \chi_{c1} K^{*0}(K_L \pi^0)$	15	0.6%
$-\alpha$	$B^0 \rightarrow J/\psi K^{*0}(K_S \pi^0)$	29	1.2%
	$B^0 \rightarrow \chi_{c1} K^{*0}(K_S \pi^0)$	2	0.1%

Table 8.3: Background in the $B^0 \rightarrow J/\psi + K_L$ candidate events and their CP asymmetry.

8.5.2   Result

We first perform a "blind analysis" in order to check presence of any asymmetry in the Δt that does not come from CP. In this analysis, we assign all events which are successfully flavor-tagged to $\bar{B}^0 \rightarrow J/\psi K_L$. This removes the CP originated asymmetry from the Δt distribution because the $\sin 2\phi_1$ terms in both positive and negative Δt sides cancels. Resulting Δt distribution should exhibit a B lifetime distribution.

Figure 8.6 shows the result of "blind analysis" for the events in the signal p_B^* region. A fit gives $\sin 2\phi_1 = 0.22 \; ^{+1.20}_{-1.12}$ when the B lifetime is fixed as world average value (1.548 ps). If we fix $\sin 2\phi_1$ to be zero, we get $\tau_B = 1.46 \; ^{+0.45}_{-0.38}$ ps. These value are consistent with expectation.
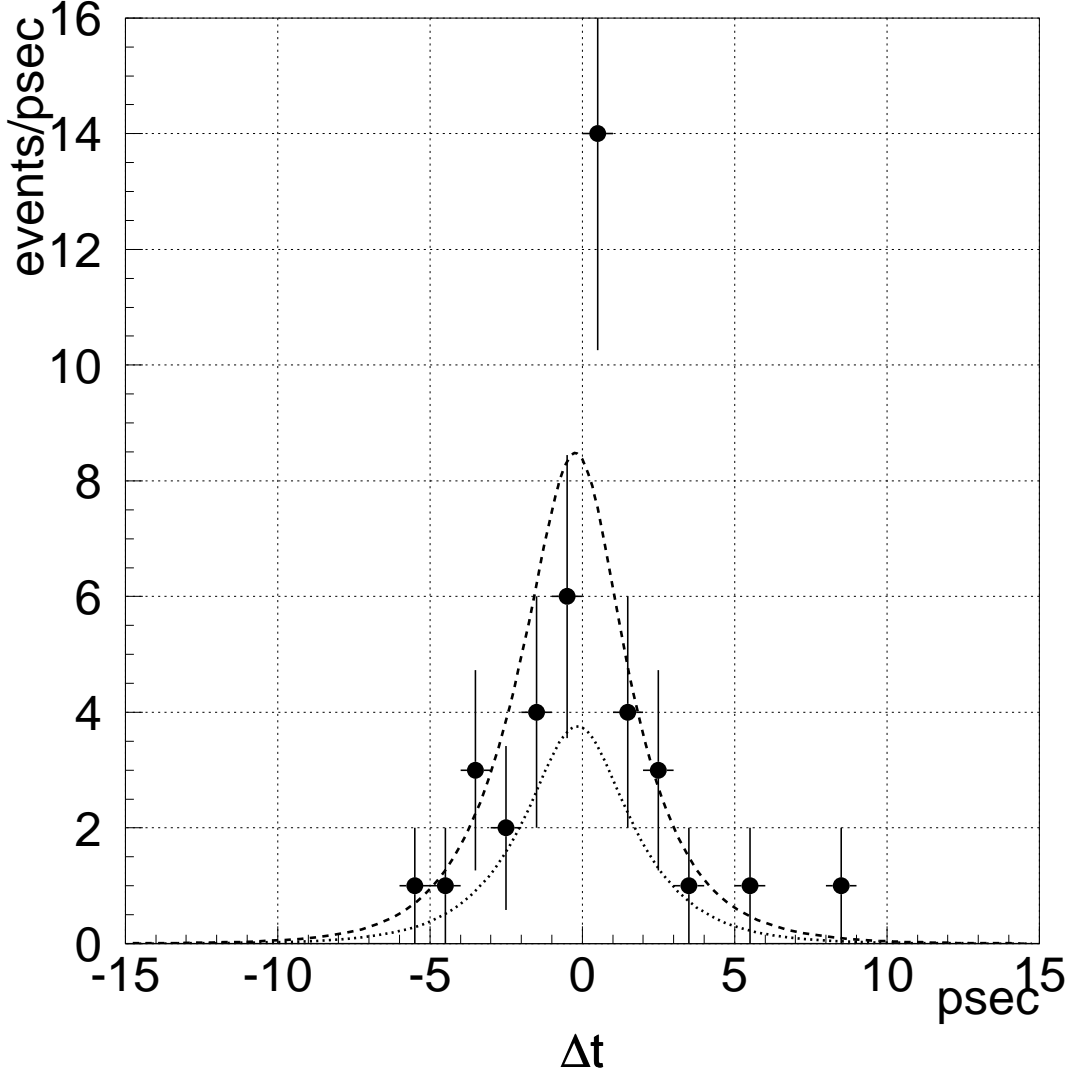
Figure 8.6: The Δt distribution in the "blind analysis" for the events in the signal p_B^* region. Upper broken line shows the overall shape of the fitting function, and lower dotted line shows the shape of background function.

Figure 8.7 shows the Δt distribution for after tagging the flavor of B^0 meson. $\bar{B}^0 \to J/\psi K_L$ events and $B^0 \to J/\psi K_L$ events are shown separately.

Figure 8.8 shows the result of CP analysis. Entry of each event Δt this plot is done in such a way that we flip the sign of Δt if it is tagged as $B^0 \to J/\psi K_L$. This way of representing the data should result in an excess entry of events due to the $\sin 2\phi_1 \sin(\Delta mt)$ term in the negative Δz region if $\sin 2\phi_1$ takes a positive value. This is opposite from the $J/\psi K_S$ case. The fitted curve that is superimposed in the figure is for $\bar{B}^0 \to J/\psi K_L$.

While the fitting is done properly, the CP-dependent Δt shape for the $B^0 \rightarrow J/\psi K_L$ sample with their Δt sign being flipped is not completely identical to that of the $B^0 \rightarrow J/\psi K_L$ sample. This is because a small shift in the Δt distribution due to the D^* contribution occurs toward the negative side for both cases and flipping of the Δt sign causes a flip of this shift also. However, the 20 μm shift corresponds to about 0.16 ps shift, and too small to be noticeable with the present level of statistics.

A fit gives $\sin 2\phi_1 = -1.00 \; {}^{+0.89}_{-0.73}$ when the τ_B is fixed at the world average value.

Figure 8.7: The Δt distribution after tagging the flavor of B^0 meson. $\bar{B}^0 \to J/\psi K_L$ events (top) and $B^0 \to J/\psi K_L$ events (bottom) are shown separately.
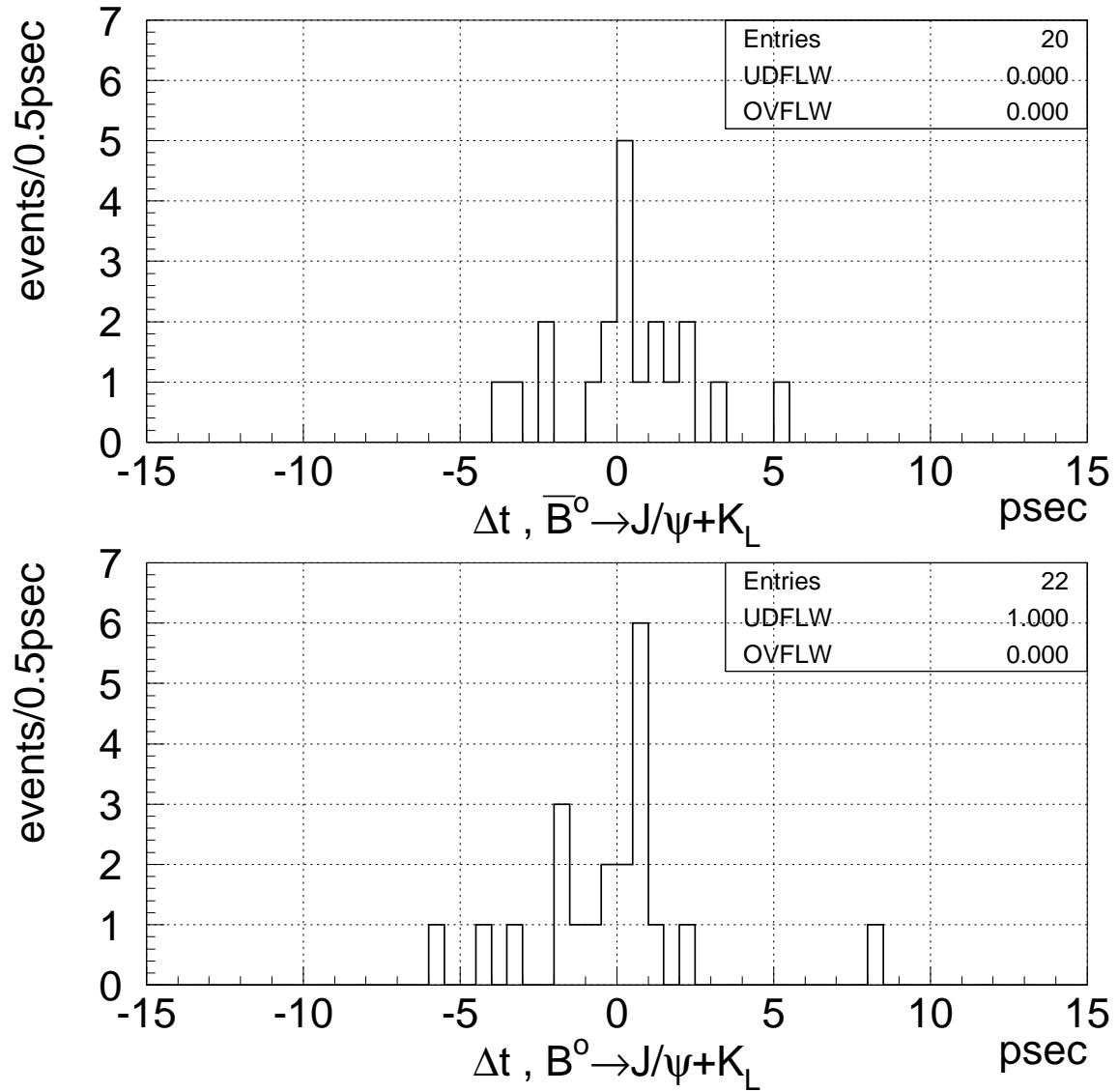
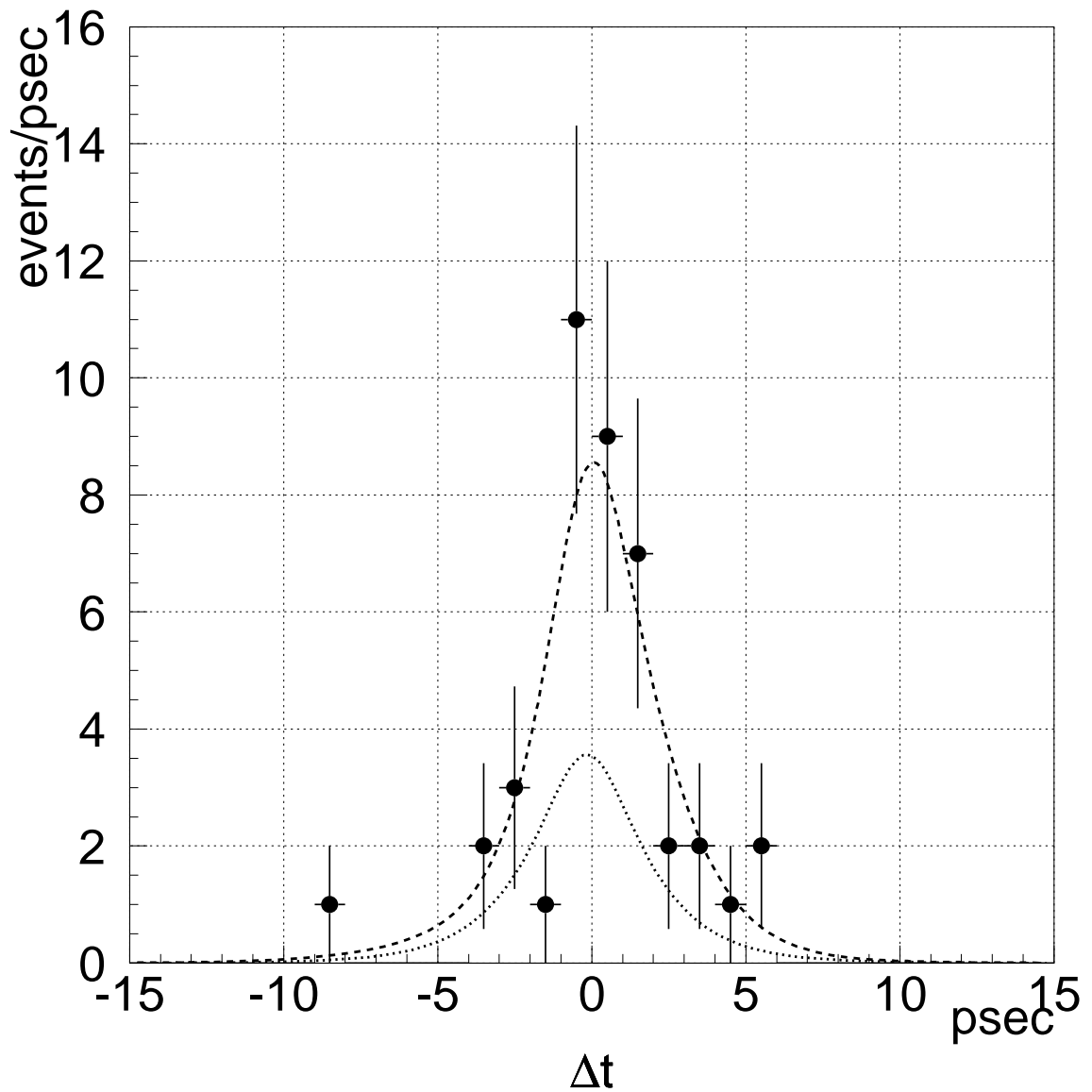Figure 8.8: The Δt distribution and the CP fit result for the events in the signal p_B^* region. Upper broken line shows the overall shape of the fitting function, and lower dotted line shows the shape of background function.

Chapter 9

Conclusion

We have measured the CP asymmetry parameter $\sin 2\phi_1$ in the $B^0 \to J/\psi + K_L$ decay.

For the detection of K_L and muons, the KLM detector subsystem was constructed which was based on glass-electrode resistive plate chambers (RPC). The superlayer structure and independent gas/HV lines for each detector module provides a stable and reliable operation. Although this was the first time that the glass plates were used as the RPC electrode, the performance of the system under the high luminosity runs was proved to be excellent.

We measured the K_L by finding the hadron showers with the combination of the KLM and the electromagnetic calorimeter. Only the K_L direction was measured in this experiment. The magnitude of K_L momentum was determined by the measured J/ψ momentum and K_L angle, and assuming the two body decay. The $B^0 \to J/\psi + K_L$ signal was extracted from the center-of-mass momentum spectrum of the parent B^0.

We used the first data set taken by the Belle detector at KEK B-factory from June 1999 to July 2000. The total integrated luminosity of 6.2 fb^{-1} is accumulated on the energy of $\Upsilon(4S)$ resonance. We observed 102 candidate of $B^0 \to J/\psi + K_L$ events in total, where 48 events are estimated to be the background events from the fitting results for the shape of p_B^* distribution obtained by Monte Carlo simulation study. This is the first direct observation of the $B^0 \to J/\psi + K_L$ decays. We observe about 20% discrepancy of the K_L yield between data and Monte Carlo. Study of hadron shower formation in the detector using charged pions and kaons in the data showed that the Monte Carlo might not be representing the real data correctly.

We could successfully identify the flavor of B mesons by either high momentum lepton, kaon of all momentum range, mid-momentum lepton, and slow pion. We could also measure the distance between two B meson vertices with the silicon vertex detector. A total of 42 events remained out of 102 events after the flavor tagging was done.

Although statistic is limited, from the fitting to the proper time distribution of the 42 events we obtained the value

$$\sin 2\phi_1 = -1.00 \, ^{+0.89}_{-0.73}. \tag{9.1}$$

It should be noted that the discrepancy in the K_L detection efficiency which we observe between Data and Monte Carlo has no effect for the $\sin 2\phi_1$ measurement since it depends only on the Δt distribution in $B^0 \rightarrow J/\psi K_L$ events and $\bar{B}^0 \rightarrow J/\psi K_L$ events.

The current preliminary result of $\sin 2\phi_1$ value of Belle experiment, which is the combined result of fitting to the $J/\psi K_S$, $\psi(2S)K_S$, $\chi_{c1}K_S$, $J/\psi \pi^0$ and $J/\psi K_L$ (98 events in total), is $\sin 2\phi_1 = 0.45 \, {}^{+0.43}_{-0.44}(stat) \, {}^{+0.07}_{-0.09}(syst)$. The $\sin 2\phi_1$ value of $B^0 \rightarrow J/\psi + K_L$ mode alone has the opposite sign from the combined result. It should have the same value as that from other channels based on our formalism. We believe that this is a result of statistical fluctuation due to small event sample. However, this analysis demonstrated that we can extract $\sin 2\phi_1$ value from the $B^0 \rightarrow J/\psi + K_L$ mode. As we accumulate more event sample, an accurate determination of $\sin 2\phi_1$ should follow.

Appendix A

$J/\psi K^*(K_L\pi)$ reduction

In this chapter we describe the study for the reduction of $J/\psi K^*(K_L\pi)$ background events. We tried to reduce the background which comes from $B \to J/\psi K^*(K_L\pi)$ by attempting to reconstruct positively the $K^* \to K_L\pi$ for the events which remain in the signal region.

A.1 $\quad B^- \to J/\psi K^{*-}(K_L\pi^-)$

We add all available π^- in the event with J/ψ and K_L one by one, and compute the p_B^* assuming 3-body decay. We also compute the $m_{K\pi}$ assuming 3-body decay. Figure A.1 shows a result of this study with Monte Carlo sample, which is summarized in Table A.1. Although simple one-dimensional cuts on p_B^* or $m_{K\pi}$ assuming 3-body decay reduces the background significantly, they also lower the efficiency for the signal events. The box cut of p_B^* and $m_{K\pi}$, on the other hand, reduces the background by half while lowering the signal efficiency by only 16%.

We tried further reduction of this background by using the vertex information. The z vertex of π^- tracks should coincide with that of J/ψ if the pion track originates from K^{*-}, whereas the pion in the $J/\psi K_L$ events should have no correlation. We select "good pions" by making a cut on the confidence level of a fit which tries to find a common vertex between J/ψ and pion. Table A.2 summarizes the result of this study. The signal to background ratio is worse when the vertex information is added and the Figure Of Merit (F.O.M) shows hardly an improvement. Our vertex resolution is not good enough for this purpose.

A.2 $\quad \bar{B}^0 \to J/\psi K^{*0}(K_L\pi^0)$

We repeated an analysis described in the previous section to reduce the $J/\psi K^{*0}$ $(K_L\pi^0)$ background. Figure A.2 shows p_B^* vs $m_{K\pi}$ plot for this study. Table A.3 summarizes the result. The result is almost same as that in $B^- \to J/\psi K^{*-}(K_L\pi^-)$ reduction.
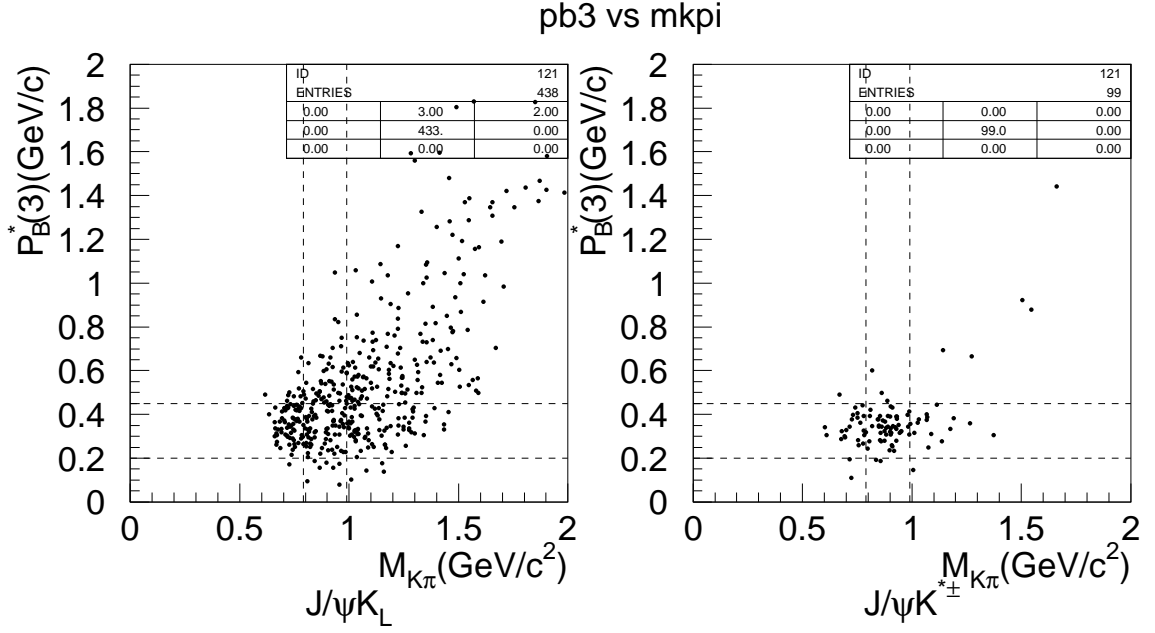
pb3 vs mkpi

Figure A.1: Monte Carlo results of p_B^* (3-body) vs $m_{K\pi}$ for $J/\psi K_L$ (left) and for $J/\psi K^{*-}(K_L\pi^-)$ (right).

decay mode	signal $J/\psi K_L + X$	background $J/\psi K^{*-} + X$
#generated	2000	2000
#J/ψ	1004	965
#$J/\psi K_L$	630	490
#$J/\psi K_L\pi^-$	601	478
$0.20 \leq p_B^* \leq 0.45$	459 (23.1%)	102 (5.1%)
$0.79 \leq m_{K\pi} \leq 0.99$	335 (16.8%)	48 (2.4%)
$0.20 \leq p_B^*(3) \leq 0.45$	251 (12.6%)	17 (0.9%)
$m_{K\pi} - p_B^*(3)$ box	386 (19.3%)	53 (2.4%)

Table A.1: Reduction of signal and background candidates in the $J/\psi K^{*-}(K_L\pi^-)$.

CL cut	signal	background	SB	F.O.M
no cut	2307	446	5.17	44.05
CL$\leq$ 0.1	2359	485	4.86	44.25
CL$\leq$ 0.01	2348	473	4.96	44.25
CL$\leq$ 0.001	2342	469	4.99	44.25

Table A.2: Use of vertex information in the $J/\psi K^{*-}(K_L\pi^-)$ analysis starting from the event sample that passed the p_B^*(3-body)-$m_{K\pi}$ cut.
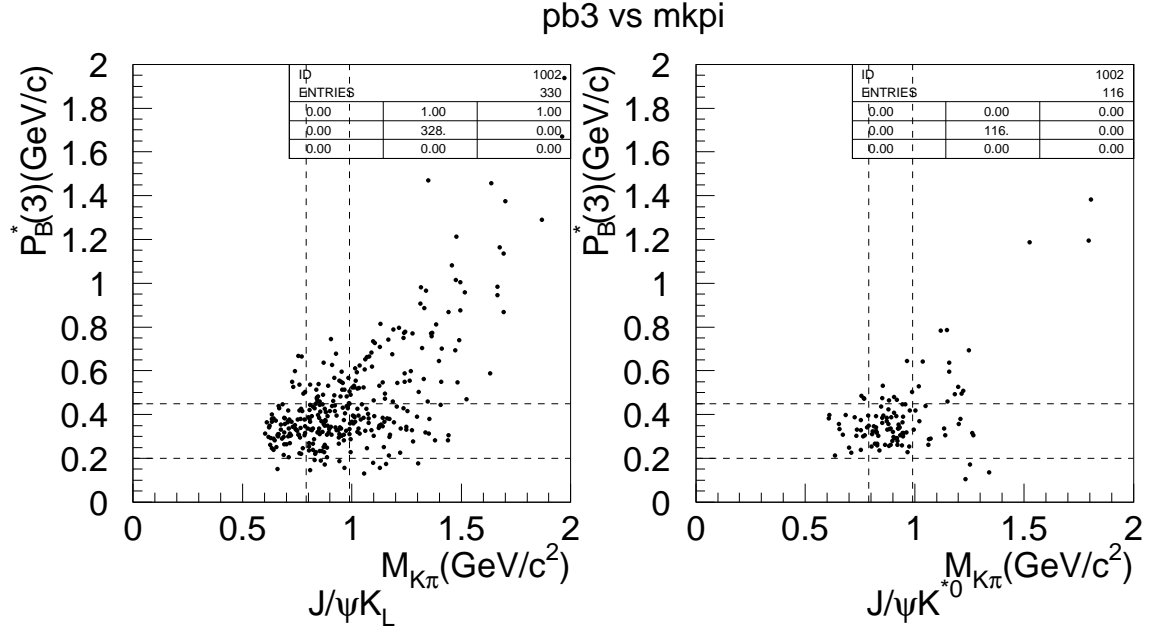
Figure A.2: Monte Carlo results of p_B^* (3-body) vs $m_{K\pi}$ for $J/\psi K_L$ (left) and for $J/\psi K^{*0}(K_L\pi^0)$ (right).

decay mode	signal $J/\psi K_L + X$	background $J/\psi K^{*0} + X$
#generated	2000	2000
#J/ψ	1019	981
#$J/\psi K_L$	699	524
#$J/\psi K_L \pi^0$	469	429
$0.20 \leq p_B^* \leq 0.45$	484 (24.2%)	135 (6.8%)
$0.79 \leq m_{K\pi} \leq 0.99$	218 (10.9%)	50 (2.5%)
$0.20 \leq p_B^*(3) \leq 0.45$	128 (6.4%)	28 (1.4%)
$m_{K\pi} - p_B^*(3)$ box	403 (20.2%)	77 (3.9%)

Table A.3: Reduction of signal and background candidates in the $J/\psi K^{*0}(K_L\pi^0)$.

A.3 Summary

Although the box cut of p_B^* and $m_{K\pi}$ assuming 3-body decay removes a significant fraction of the $J/\psi K^*(K_L\pi)$ background, we did not use it in this analysis. This is because a limited statistics of the data sample does not allow a reliable examination of the performance of this method, and we must rely entirely on the Monte Carlo study.

Bibliography

[1] J. H. Christensen *et al.*, Phys. Rev. Lett. 13 (1964) 138.

[2] M. Kobayashi and T. Maskawa, Prog. Theo. Phys 49 (1973) 652.

[3] J. E. Augustin *et al.*, Phys. Rev. Lett. 33 (1974) 1406.

[4] J. J. Aubert *et al.*, Phys. Rev. Lett. 33 (1974) 1404.

[5] S. W. Herb *et al.*, Phys. Rev. Lett. 39 (1977) 252.

[6] A.Carter and A.I.Sanda, Phys.Rev.Lett. 45(1980)952;Phys.Rev.D23,1567(1981);
I. I. Bigi and A. I. Sanda, Nucl. Phys. 193,851(1981).

[7] E. Fernandez *et al.*(MAC), Phys. Rev. Lett. 51 (1983) 1022;
N. Lockyer *et al.*(MARKII), Phys. Rev. Lett. 51 (1983) 1316.

[8] The BaBar collaboration, Technical Design Report, (1995).

[9] F.Abe *et al.*(CDF collaboration), Phys. Rev. Lett. 81 (1998) 5513.

[10] LHC-B Letter of Intent, CERN/LHCC 95-5, LHCC/18, August 1995.

[11] S.Weinberg : Phys.Rev.Lett. Phys. Rev. Lett. 19 (1967) 1264,
A.Salam : Elementary Particle physics, ed. N.Svartholm (Almquist and Wiksells, Stockholm 1968) 367.

[12] L.Wolfenstein, Phys. Rev. Lett. 51 (1983) 1945.

[13] C.Caso *et al.*, [Particle Data Group], Eur. Phys. J. C3, 1 (1998).

[14] R.Aleksan, to appear in: Proceedings of the International Europhisics Conference on High Energy Physics, Brussels, Belgium, September 1995.

[15] *KEKB B-factory design report*, KEK Report 95-3, 1995.

[16] BELLE SVD group, *Technical design report of BELLE SVD*, 1998.

[17] S.K. Sahu *et al.*, BELLE Note 203 (1997).

[18] A. Abashian *et al.*, Nucl. Instr. and Meth. A449 (2000) 112.

[19] M. Sanpei *et al.*, IEEE Trans. Nucl. Sci. Vol.44, No.3, 752(1997).

[20] R. Itoh and S. Ichizawa, BELLE Note 97 (1995).

[21] S. Nagayama, *PANTHER — User's guide —*, Version 3.0 (1997).

[22] A. Putzer, Comput. Phys. Commun. 57,156(1989).

[23] K.Hanagaki *et al.*, BELLE Note 312 (2000).

[24] L.Piilonen *et al.*, BELLE Note 338 (2000).

[25] KID group, BELLE Note 321 (2000).

[26] CLEO software document homepage :
http://www.lns.cornell.edu/public/CLEO/soft/QQ/index.html (1998).

[27] R. Itoh, *QQ quick reference for BELLE* (1995).

[28] T.Sjöstrand, "PYTHIA 5.7 and JETSET 7.4 Physics and Manual", CERN-TH.7112/93 (1993).

[29] *"GEANT" Detector Description and Simulation Tool*, CERN program Library Long Writeup W5013 (1993).

[30] H. Ozaki, BELLE Note 99 (1996).

[31] S. Azuchi *et al.*, BELLE Note 265 (1999).

[32] S. Azuchi, Master thesis, Tohoku University, February, 2000.

[33] S. Kumar, BELLE Note 351 (2000).

[34] G. Fox and S. Wolfram, Phys. Rev. Lett. 41 (1978) 1581.

[35] J. Suzuki, BELLE Note 313 (2000).

[36] T.Nakadaira *et al.*, BELLE Note 290 (2000).